THE NORDIC CONCRETE FEDERATION 1/2010 PUBLICATION NO. 41

Nordic Concrete Research

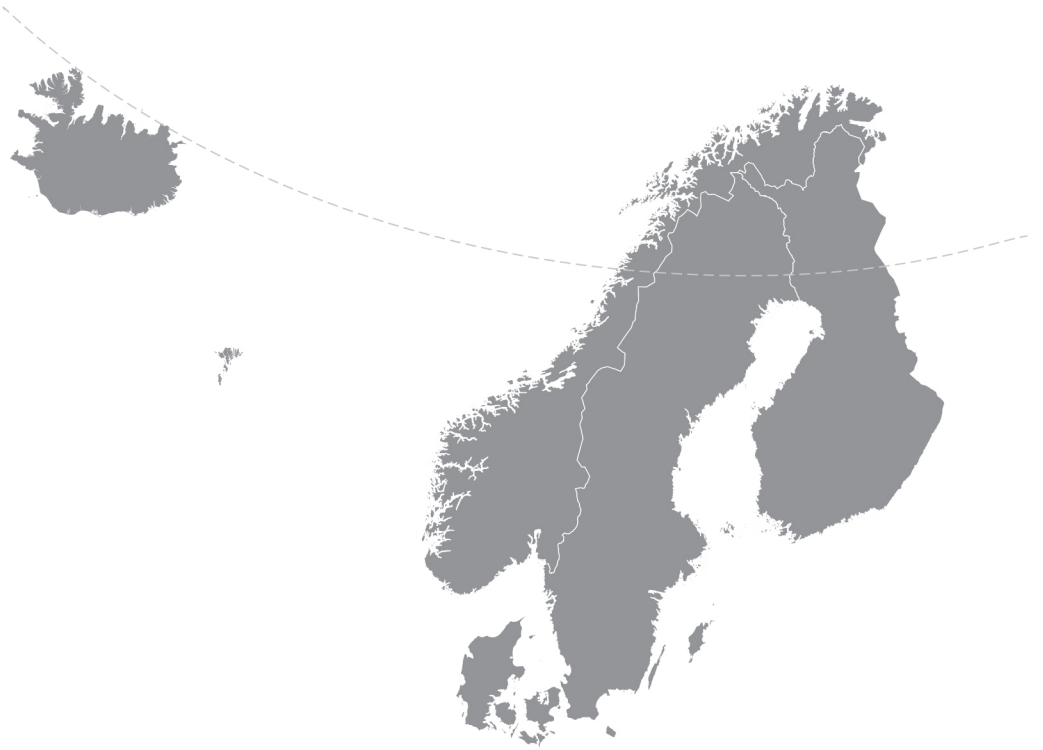

Nordic Concrete Federation

PUBLICATION NO. 41 1/2010

NORDIC CONCRETE RESEARCH

EDITED BY
THE NORDIC CONCRETE FEDERATION

CONCRETE ASSOCIATIONS OF: DENMARK
FINLAND
ICELAND
NORWAY
SWEDEN

PUBLISHER: NORSK BETONGFORENING
POSTBOKS 2312, SOLLI
N - 0201 OSLO
NORWAY

VODSKOV, JUNE 2010

Preface

Nordic Concrete Research is since 1982 the leading scientific journal concerning concrete research in the five Nordic countries, e.g., Denmark, Finland, Iceland, Norway and Sweden. The content of Nordic Concrete Research reflects the major trends in the concrete research.

Nordic Concrete Research is published by the Nordic Concrete Federation that beside the publication activity also organizes the Nordic Concrete Research Symposia that have constituted a continuous series since 1953 in Stockholm. The Symposium circulates between the five countries and takes place every third year. The next will be held in Finland June 5 – 8, 2011. Information can be found on www.nordicconcrete2011.fi

Papers presented in the journal are also published on the homepage. For the first half year only the abstracts are published there, thereafter the full paper.

Since 1982, 354 papers have been published in the journal. Since 1994 the abstracts and from 1998 both the abstracts and the full papers can be found on the Nordic Concrete Federation's homepage: www.nordicconcrete.org

Vodskov, June 2010

Dirch H. Bager
Editor, Nordic Concrete Research

PUBLICATION NO. 41 1/2010

CONTENTS

1. Morten Hernes & Morten Christensen
Application of CRC JointCast in Joint Details of Precast Elements 1

2. Siaw Foon Lee & Stefan Jacobsen
Sample preparation, image acquisition and image analysis on interfacial transition zone of steel fiber-reinforced mortar 15

3. Siaw Foon Lee, Xiao Hui Wang & Stefan Jacobsen
Mix design and the effect of silica fume and steel fiber on rheological and mechanical properties of mortars 33

4. Anders Johansson-Selander, Mårten Janz, Johan Silfwerbrand & Jan Trägård
Penetration Profiles of Water Repellent Agents in Concrete as a Function of Time – Determined with FTIR-Spectrometer 51

5. Anders Sjöberg, Patrice Blondeau & Peter Johansson
Measurement methods for stored VOC in concrete floors 61

6. Sofia Utsi & Jan-Erik Jonasson
Influence of different amount of fly ash for early age concrete containing Swedish cement - Part I: Tendency model for heat and strength development for variable fly ash content 77

7. Sofia Utsi & Jan-Erik Jonasson
Influence of different amount of fly ash for early age concrete containing Swedish cement - Part II: Calculation of form stripping times and the risk for early freezing for different amounts of fly ash 93

Application of CRC JointCast in Joint Details of Precast Elements

Morten Hernes
Stud.Cand.Scient. Architectural Engineering
Fredensgade 16, 19, DK-8000 Aarhus
E-mail: mortenhernes@hotmail.com

Morten Christensen
B. Sc. Architectural Engineering
Snogebæksvej 27, 8, DK-8210 Aarhus
E-mail: mortenchristensen2@gmail.com

ABSTRACT

Compact Reinforced Composite (CRC) is a relatively new material that combines a high strength, densely packed cement matrix with high fibre content. The current project investigates the shear capacity concerning application of CRC in the vertical joints between precast concrete elements. For the purpose CRC JointCast, a special type of CRC, are utilized. The paper presents and discusses the results of 30 full-scale tests with 10 different joint details. The tests showed that easy-to-construct joints with significantly higher load bearing capacities were achieved by the application of CRC in the joints, especially with rough surface construction joints.

Key words: CRC, PCC-elements, joint details, shear force, tests

1. INTRODUCTION

CRC JointCast is a type of CRC designed specifically for use in small quantities and typically in critical parts of the structure. [1] The fibres are made of steel and the content is 6% by volume. CRC JointCast is characterised by a compressive strength in the region of 120-160 MPa, and a tensile strength in the order of 10 MPa.

Over the last decade the application of CRC has been increasing in an array of various areas from balconies and staircases, to bigger machine parts and repair works. CRC and its properties have been investigated extensively but its application as CRC JointCast in joints of precast structures has nevertheless been studied only a little. This project intended to investigate the load bearing capacities of CRC JointCast in the vertical joints between precast elements subject to a shear force.

The project was carried out at the Aarhus School of Engineering (ASE) as part of the authors' bachelor project with support from Hi-Con, the world's largest producer of CRC elements. Testing was carried out in the laboratories at ASE. The project was launched in June 2009 and finalised in January 2010.

2. JOINT DETAILS TESTED UNTIL FAILURE

2.1 Test programme

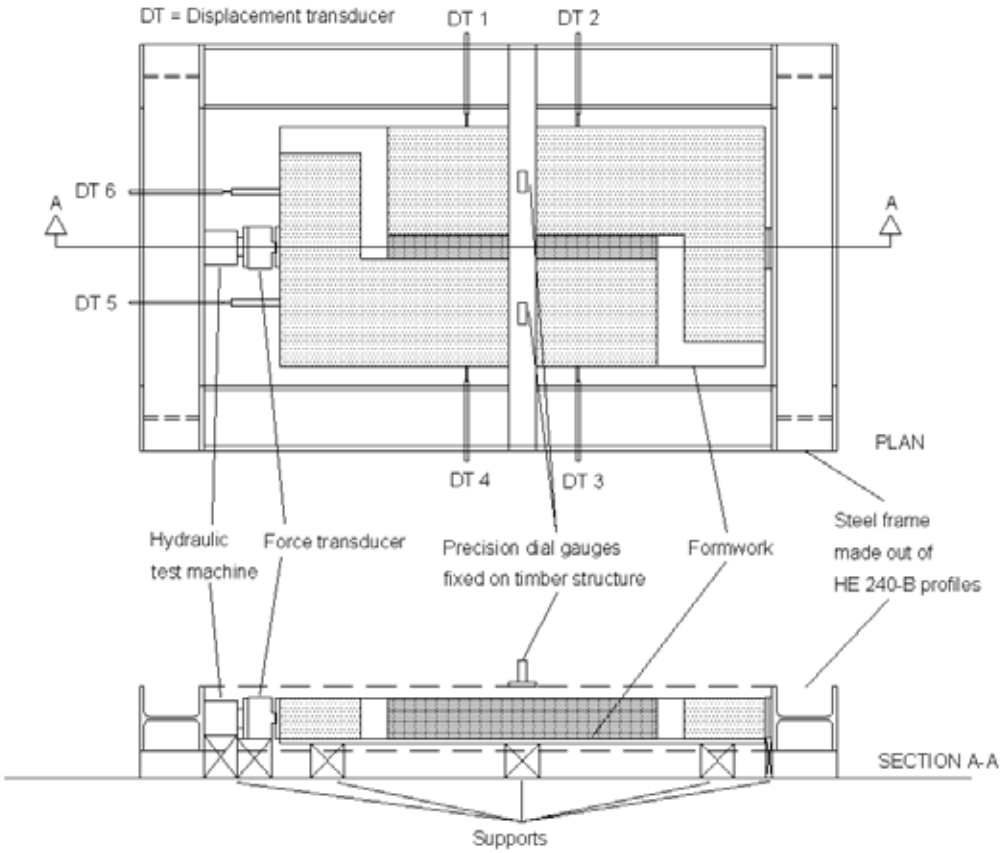

Figure 1 – Testing setup in the laboratory at ASE

The programme was aimed at investigating the shear capacity of vertical joints in precast elements, and a total of 30 test specimens were tested in a testing setup as seen in Figure 1. The elements had the distinctive L-shape so as to have the force in the centerline of the joint between the elements. Each of the elements was 1400 mm in length, while the length of the joint was 1000 mm.

The test programme comprised 10 varying joint details. Different parameters in the design of the joint details were changed to probe their effect on the shear capacity. The parameters were the concrete mixture, different design of the reinforcement, and rough or indented surfaces. To establish a better basis for further analysis and research only one factor at a time was altered between the details. In addition each test was repeated twice. The 10 different joint details are shown in Figure 2. The unreinforced details were only tested for comparison as unreinforced details will never fulfil the codes, as the elements are unreinforced in the contact area.

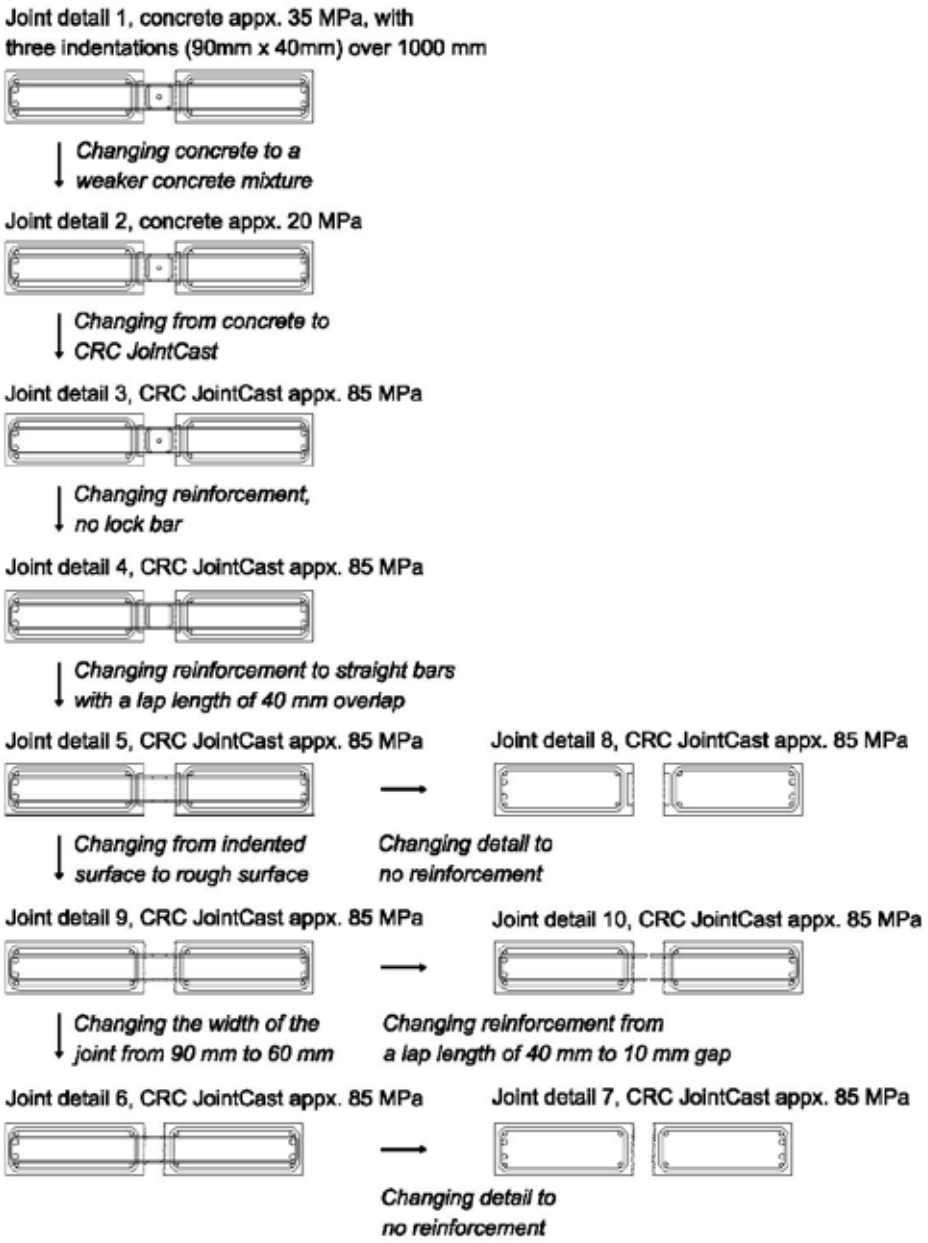

Figure 2 – Test programme, 10 joint details

A typical joint detail (Joint detail 1) was the base for the test programme, but due to the special properties of CRC, the indented surface had to be altered from the typical joint detail to a new type so that a failure in the joint could be achieved. As a result the indented surface had three indentations, each 90 mm by 40 mm, which equals to less than 10% of the total joint area. Typical joint details in the building industry have a total joint area in the region of 50%. [2]

The details with rough surface were not as such an investigation to the capacity of CRC JointCast, but as to how a rough surface could inflict on the load bearing capacities of the details. The details with rough surface were estimated so that the precast element surface would fail at about half the capacity of the hydraulic test machine. The rough surface was applied upon the whole area of the construction joint. This was done by application of retarder on the formwork prior to casting. The two types of construction joints are shown in Figure 3.

The testing was done horizontally in a steel frame specially constructed for the project. A 500 kN hydraulic test machine and a force transducer were placed in continuation of each other in the centreline of the joint. Steel plates were placed between the transducer and the test specimen and between the test specimen and the steel frame. These plates ensured that the force from the hydraulic test machine was acting on the same area at both ends of the test specimen. During the loading 6 horizontal displacements were monitored by LVDT transducers and before, during and after the testing 2 manually monitored precision dial gauges were employed in the vertical direction.

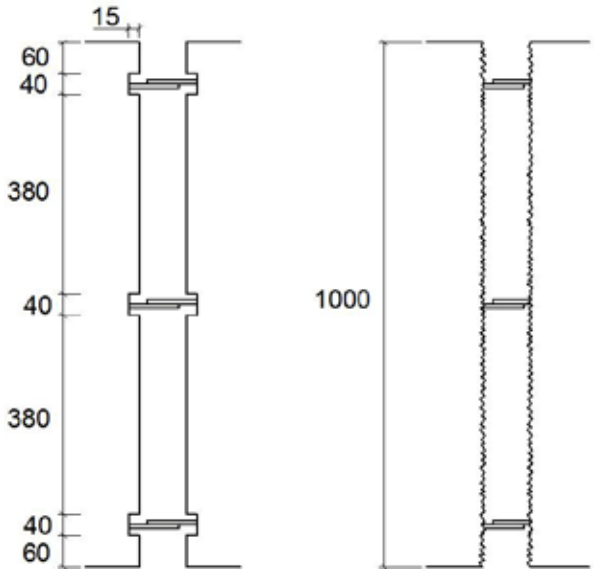

Figure 3 – Construction joints, indented and rough surface

During testing, the load was increased continuously until failure occurred, or until the maximum capacity of the hydraulic machine was reached. In these instances the joint details had achieved distinctly higher loads than the predicted load to achieve failure.

The reinforcement was bent according to normal bending rules and procedures, and was tied together at ASE. Each joint detail required a specific arrangement of the reinforcement, and was tied accordingly. Concrete grading in the elements was C40/50 and the batch was delivered in a truck from the concrete supplier Unicon, and unloaded using a conveyor belt. The concretes for joint details 1 & 2, and CRC JointCast for the other details were mixed and cast at ASE with precision, and in accordance with normal practice.

CRC JointCast was mixed using a binder, consisting of cement, microsilica and super plasticizer, steel fibres and water. The steel fibres were smooth, straight and had a length of 12,5 mm, and a diameter of 0,4 mm.

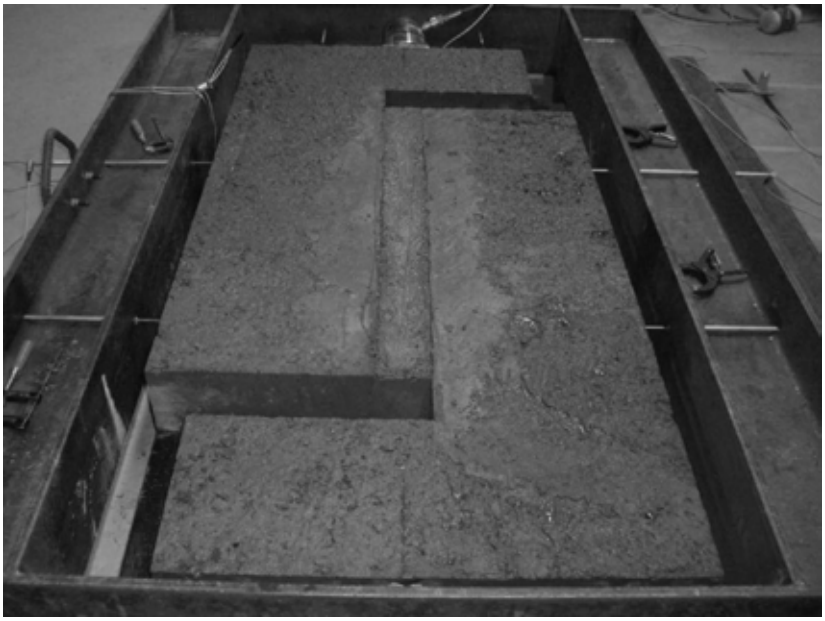

Figure 4 – Test specimen before testing in the laboratory at ASE

2.2 Properties

To determine the properties used for calculations, cylinder tests were made for the four types of concrete; concrete for the elements, concrete (35 MPa) for joint detail 1, concrete (20 MPa) for joint detail 2 and CRC JointCast for the remaining details. The results for CRC JointCast were based on 100x200 mm cylinder tests, the other tests were based on 150x300 mm cylinders.

As the tests of the joint details were performed during 6 days, the properties for the materials were determined for each of these 6 days. This was done by adopting the concept of linear curing, and thus drawing a line between the measured averages of the cylinder tests undertaken before and after the tests. The properties of the materials are shown in Table 1, and the results are given only for the days the tests with the specific concrete were performed.

The test values for the compressive strength, f_c, of CRC JointCast were expected to be around 140MPa, but the test results showed a compressive strength between 80 and 90 MPa. This could be attributed to the location of storage of the test specimens. Both the elements and the cylinders were stored outdoors under plastic linings, and cold weather (some days under 10 degrees Celsius) affected the curing time. Determination of properties for the cylinders was based on tests taken both before, and after the testing of the joint details. Consequently the cylinders had a curing time of 14 days and 26 days, respectively.

Similarly with the concrete, the mechanical properties of CRC JointCast will develop on account of the chemical reactions between cement and water. The speed on which cement hydrates, and subsequently develops higher strength, will be faster at higher temperatures. The deviation from the expected values was larger with CRC JointCast than with the other types of concrete. [3]

The tensile strength, f_t, of the concrete cylinders was determined as the splitting tensile strength. Each cylinder was cut in half, and placed in the testing machine in the longitudinal direction. The splitting tensile strength was determined. In table 1 the tensile strength is presented as 90% of the splitting tensile strength. [4]

Table 1 – Properties used for calculations

Date	Concrete elements		Concrete for joint detail 1		Concrete for joint detail 2		CRC JointCast	
	f_c MPa	f_t MPa	f_c MPa	f_t MPa	f_c MPa	f_t MPa	f_c MPa	f_t MPa
08.11.09	42,5	3,04	33,6	2,60	19,7	1,52	-	-
09.11.09	42,9	3,07	-	-	-	-	80,5	11,2
10.11.09	43,3	3,10	-	-	-	-	83,4	11,4
11.11.09	43,7	3,13	-	-	-	-	86,2	11,7
12.11.09	44,1	3,16	-	-	-	-	89,0	12,0
13.11.09	44,5	3,19	-	-	-	-	91,8	12,4

2.3 Results for shear loads

The main results from the test programme are shown in Table 2 and Table 3. Table 2 presents the results for the joint details with indented surface, while Table 3 presents the results for the joint details with rough surface. The estimated capacities shown in Table 2 and Table 3 were calculated using the properties measured from the cylinder tests presented in Table 1.

The formula used for calculating the estimated shear force resistance, V_{Rki}, of the joint details is shown below. This formula is taken from the European Standard [4], and is the conventional calculation method for shear capacity at the interface between concrete cast at different times. The cross-sectional area is included in the formula to give an estimate of the anticipated forces.

Due to the limited surface area of the indentations in the joint material, the height of the indentations in the concrete element exceeds the stipulated 10*d, where d is the depth of the indentation. The project objective however, is to study the effect of the indentations in the joint material. These are within the specified 10*d, and the conventional formula was employed.

V_{Rki} is given by:

$$V_{Rki} = c \cdot f_{ctk} \cdot A_i + f_{yk} \cdot \mu \cdot A_s \leq 0{,}5 \cdot \nu \, f_{ck} \cdot A_i \quad (1)$$

where:

f_{ck} : characteristic compressive strength
f_{ctk} : characteristic tensile strength, lower bound
f_{yk} : yield strength of reinforcement (550 MPa)
A_i : cross-sectional area of the joint surface
A_s : cross-sectional area of reinforcement
ν : strength reduction factor for concrete cracked in shear
c & μ : factors which depend on the roughness of the interface; for indented surface c = 0,50 and μ = 0,9; for rough surface c = 0,40 and μ = 0,7

The main results in Table 2 are shown for each of the different joint details with indented surface. There was some variation in the achieved maximum test loads, but the shear resistance was higher than expected for all joint details. In addition to the estimated resistances and the maximum test load, two ratios are shown. Ratio 1 is the maximum test load divided by the highest value of the estimated shear force resistance and the estimated joint resistance, respectively. Ratio 2 is the maximum test load divided by the estimated resistance of the concrete element. During the testing of joint detail 8, failure occurred in the precast element rather than in the joint detail. This is indicated with marker #.

Table 2 – Results of joint details with indented surface subject to a shear force. # shows that failure occurred in the precast element rather than the joint

Joint detail no.	Test date	Est. shear force resistance kN	Est. joint resistance kN	Est. resistance of concrete element kN	Test No.	Maximum test load kN	Ratio 1	Ratio 2
1	08.11.09	163	97	269	1.1	142	1.46	0.53
					1.2	151	1.56	0.56
					1.3	140	1.44	0.52
2	08.11.09	157	64	269	2.1	138	2.15	0.51
					2.2	146	2.28	0.54
					2.3	154	2.41	0.57
3	09.11.09	209	196	270	3.1	331	1.69	1.22
					3.2	399	2.03	1.48
					3.3	351	1.79	1.30
4	09.11.09	209	196	270	4.1	344	1.76	1.27
					4.2	343	1.75	1.27
					4.3	306	1.56	1.13
5	10.11.09	210	203	271	5.1	339	1.67	1.25
					5.2	301	1.48	1.11
					5.3	311	1.53	1.15
8	12.11.09	65	216	125	8.1#	85#	1.31#	0.68#
					8.2	133	2.05	1.06
					8.3#	119#	1.83#	0.95#

In Table 3 the main results are shown for each of the different joint details with rough surface. In most cases the test specimens were not tested until failure. In these cases the testing was stopped since the test load came close to the capacity of the hydraulic test machine. An asterix * indicates that the specimen was not tested up to failure.

In all cases, the maximum test load was greater than the estimated resistance of the concrete element. Along with the estimated resistances and the maximum test load, two ratios are shown. Ratio 3 is the maximum test load divided by the estimated shear force resistance, while ratio 4 is the maximum test load divided by the estimated resistance of the concrete element.

*Table 3 – Results of joint details with rough surface subject to a shear force. * shows that the joint detail was not tested to failure*

Joint detail no.	Test date	Est. shear force resistance. kN	Est. resistance of concrete element kN	Test No.	Maximum test load kN	Ratio 3	Ratio 4
6	11.11.09	818	303	6.1*	455*	0.55*	1.50*
				6.2*	462*	0.56*	1.52*
				6.3*	452*	0.55*	1.49*
7	11.11.09	702	188	7.1	434	0.62	2.31
				7.2	465	0.66	2.47
				7.3*	475*	0.68*	2.53*
9	13.11.09	848	307	9.1*	464*	0.55*	1.51*
				9.2*	458*	0.54*	1.49*
				9.3*	457*	0.54*	1.49*
10	13.11.09	848	307	10.1*	460*	0.54*	1.50*
				10.2*	468*	0.55*	1.52*
				10.3*	464*	0.55*	1.51*

2.4 Results for displacements

During the tests, six displacement transducers measured the horizontal movement, two in the longitudinal direction, and four in the transverse direction, with two on either side. Table 4 presents the results for the lengthwise movement. The two displacement transducers measuring the longitudinal displacement were placed on either side of the hydraulic test machine. Measurements were taken continuously while the loading was applied. The values in the table below are the average between the two transducers at the yield load, thus displaying the displacement through the centreline of the test specimen. An asterix * indicates that the joint detail was not tested until failure. In these cases the values for displacement represents the maximum test load.

The displacements in the transverse direction were also measured continuously during the testing. There were only small displacements during the tests. The difference between the measurements on either side of the test specimen illustrates how the crack width developed during the testing. For joint detail 1 and 2 crack widths in the range of 1 millimetre were measured. For the joint

details with CRC JointCast, crack widths were in the range of 2-3 millimetres before failure occurred. The vertical displacements were monitored manually during testing, and the tendency of all test specimens was that they were lifted approximately 1 mm during loading.

*Table 4 – Results of displacement in the top of the elements at maximum test load. * shows that the joint detail was not tested to failure*

Joint detail no.	Test no.	Maximum test load kN	Displacement mm
	1.1	142	6,5
1	1.2	151	9,2
	1.3	140	6,3
	2.1	138	4,3
2	2.2	146	6,0
	2.3	154	6,3
	3.1	331	9,0
3	3.2	399	11,1
	3.3	351	8,0
	4.1	344	9,4
4	4.2	343	11,9
	4.3	306	8,2
	5.1	339	11,5
5	5.2	301	11,8
	5.3	311	10,0
	6.1*	455*	11,6
6	6.2*	462*	10,3
	6.3*	452*	13,2
	7.1	434	10,0
7	7.2	465	11,2
	7.3*	475*	11,0
	8.1	85	10,1
8	8.2	133	4,4
	8.3	119	9,3
	9.1*	464*	12,1
9	9.2*	458*	12,5
	9.3*	457*	11,6
	10.1*	460*	11,4
10	10.2*	468*	12,8
	10.3*	464*	11,7

2.5 Discussion

All test loads shown in Tables 2 and 3 present higher values than the resistances estimated employing the actual properties from the cylinder tests. The details with indented surface, joint detail 3, 4 and 5, show higher than double load bearing resistance of the two details with normal concrete. This is obviously attributable to the application of CRC JointCast as joint material. Between these three joint details there were only minor differences. This was expected as only the details of the joint reinforcement were varied but not the interface properties of the joint.

Modifying the reinforcement by removing the lock bar is likely to reduce the restraint efficiency, thus weakening the total load bearing capacity of the joint.

Figures 5, 6 and 7 display the difference between the tests with joint details 2, 3 and 5, respectively. The figures illustrate one problem with designing joints with CRC JointCast; the ductility at yield load. Joint detail 2 (Figure 5) demonstrates a very ductile behaviour after failure, indicated by the slowly descending slope in the post-peak behaviour. During testing of this joint detail, appearance of cracks was observed by sounds, and visible cracks in the joint interface appeared. The load-displacement curve indicates that the reinforcement in the joint contributes to the ductile behaviour of the joint detail.

Joint details 3 and 5 (Figures 6 and 7) had a very high load bearing capacity, twice that of joint detail 2. As a consequence, the test specimens exhibited a sudden failure with insufficient structural ductility since there was not adequate reinforcement to carry the yield load. This is reflected by the steep fall in the load-displacement curve after peak load. Test no. 3.1 and 3.3 demonstrates a slightly more ductile post-peak behaviour. This indicates that the reinforcement in the joint to some extent contributes to the ductile behaviour after peak load. Test no. 3.2 however, achieves a higher peak load but has a very steep fall in the load-displacement curve and demonstrates no ductile post-peak behaviour.

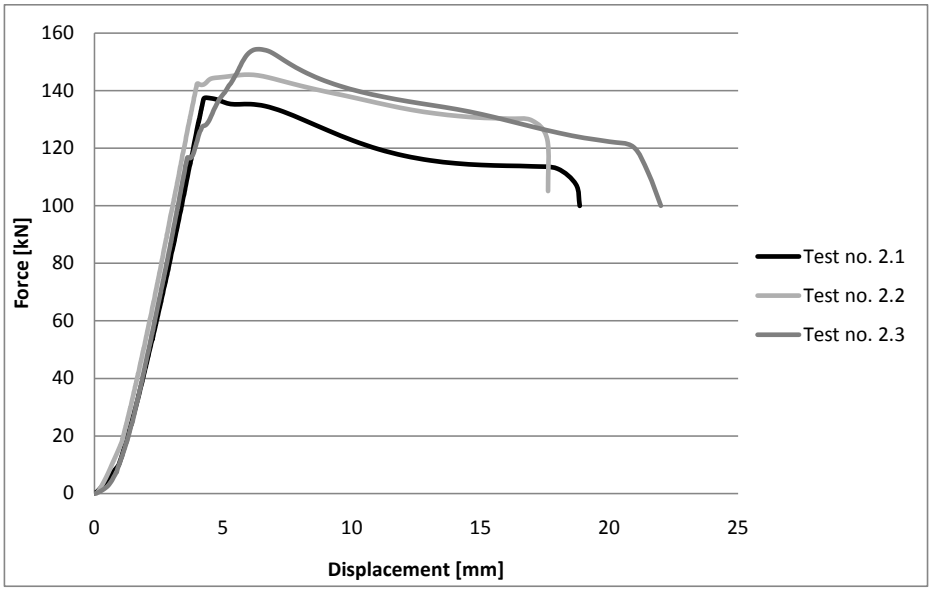

Figure 5 – Load-displacement curve for joint detail 2, concrete compressive strength 19,7 MPa, u-bar with lock bar, three indentations 90 x 40 mm

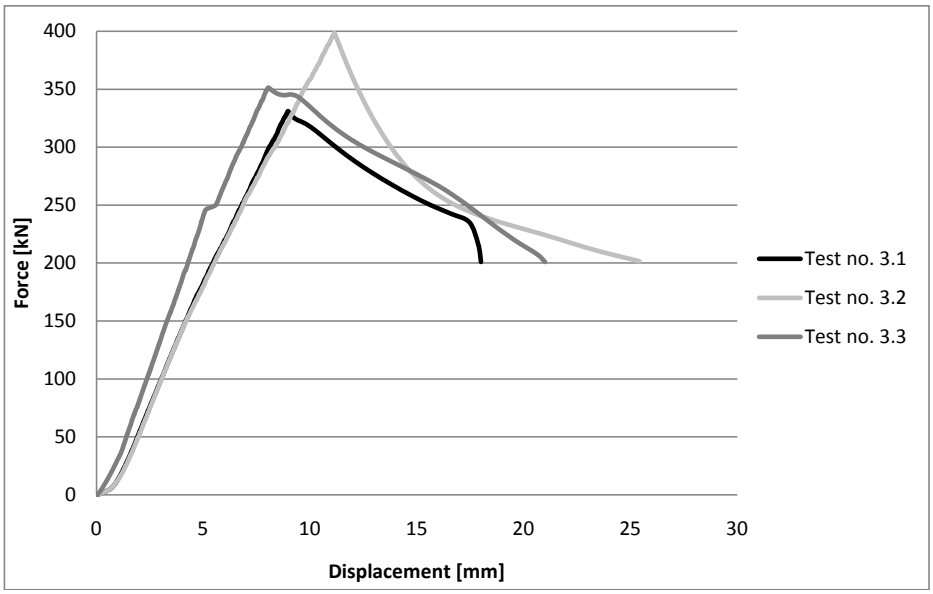

Figure 6 – Load-displacement curve for joint detail 3, CRC JointCast, u-bar with lock bar, three indentations 90 x 40 mm

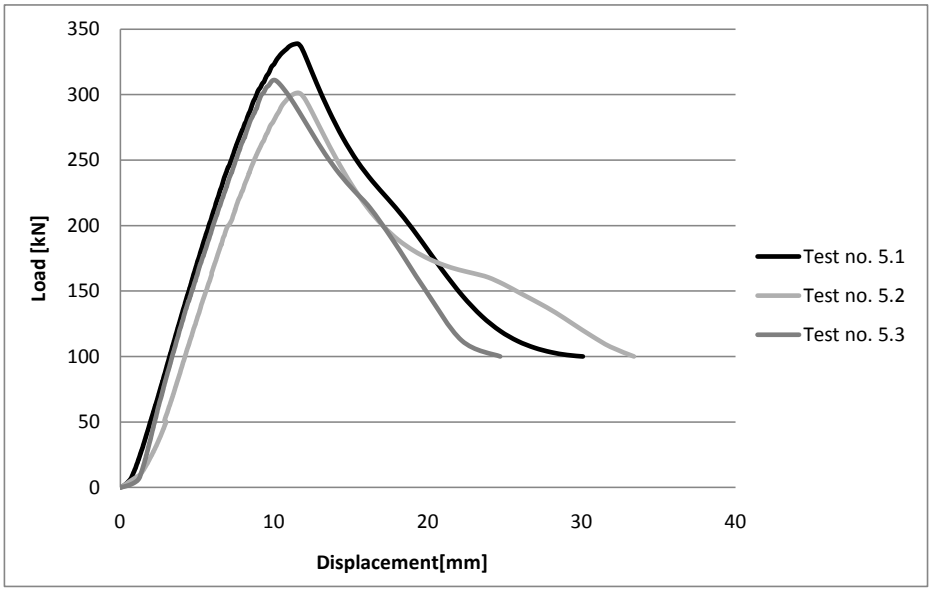

Figure 7 – Load-displacement curve for joint detail 5, CRC JointCast, straight reinforcement with 40 mm overlap, three indentations 90 x 40 mm

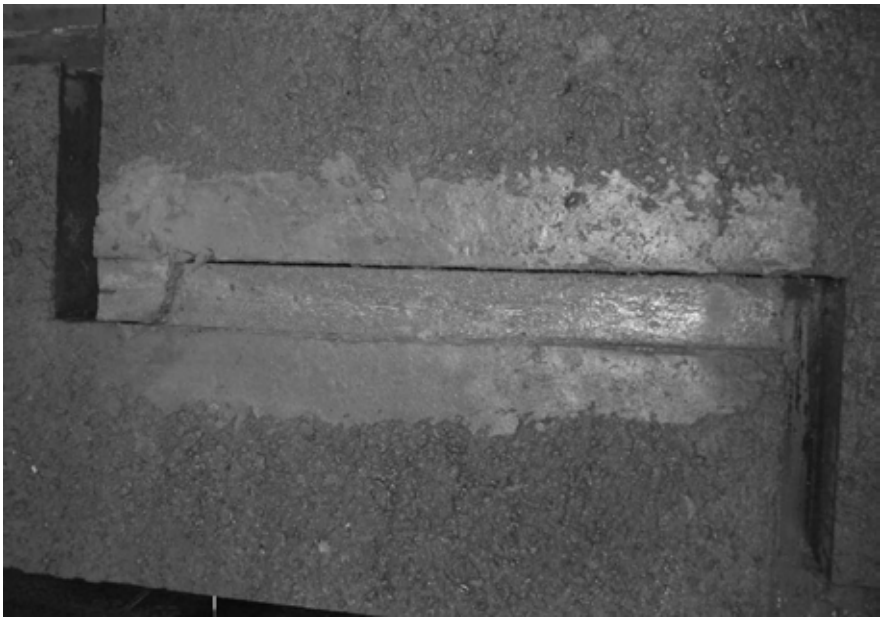

Figure 8 – Typical failure in test specimens, joint detail 5, test no. 5.3, CRC JointCast, straight reinforcement with 40 mm overlap, three indentations 90 x 40 mm

Figure 9 – Shear failure at indentation in joint detail 5, test no. 5.1, CRC JointCast, straight reinforcement with 40 mm overlap, three indentations 90 x 40 mm

Figure 10 – Failure in concrete element in joint detail 8, test no. 8.1, CRC JointCast, no reinforcement, three indentations 90 x 40 mm

Figure 8 shows a typical failure pattern for the joint details 1 to 5. The crack appeared on one side, and at the first indentation it crossed the joint and continued along the interface at the other side. There were no indications as to why this pattern occurred. A possible cause could be the additional torsional moment arising from the joint of relatively large width of 90 mm. Observations during testing with joint details 6 and 9 showed that the wider joint resulted in more cracks in the joint, even though none of them were tested until failure.

At peak load the failure at the indentations occurred as shear rupture. Figure 9 shows a typical shear failure at one of the indentations. In the shear failure through the CRC JointCast and the 8 mm reinforcement bars the fibres in the joint matrix were pulled out, rather than cut over. As noted previously, only minor displacements were observed in the transverse direction. The reinforcement presented signs of some bending stress after failure, and it is probable that the reinforcement acted as dowels in the joint material. After the cracks have appeared, the bars are activated and the yielding of the bars thereby determines the resistance of the joint.

One of the series of tests, joint detail 8, was dedicated for investigating the joint details with no reinforcement. Here, the capacity of the joint depended only on the three indentations. The tests showed high load bearing capacities with respect to applying CRC JointCast in the details. However, here the failure occurred in the concrete elements, because the indentations of CRC JointCast were so strong that spalling in the element concrete appeared. Figure 10 shows this type of failure. The lack of reinforcement resulted in almost no transverse restraint. At the same time the indentations were quite narrow, and the concrete did not have capacity enough to resist the stress.

The joint details with rough interfaces all showed remarkable high load bearing capacities. Failure could be produced in only two of the twelve tests. There is no explicit reason for this result. It is proposed that in comparison to the indented interface, the rough interface should be provided along the whole joint length. Furthermore the binder used in CRC JointCast is made out of a small particle matrix, and will therefore adhere better to the rough surface than smooth. This also applies to the details with reinforcement. Employment of such joint details may however introduce problems associated with the limited ductility, and a further investigation into this area is necessary.

3. CONCLUSION

In tests of the project various joint details were loaded in shear paying attention to the varying design of the detailing. The factors included are the type of construction surface, reinforcement design and the concrete mix.

The laboratory tests showed that significantly higher load bearing capacities were achieved by applying CRC JointCast in the joints. The application of CRC JointCast in construction joints allows the utilization of the resistance of the joints capacity optimally. Hence, the structure can be designed on account of the carrying capacity of the precast elements.

Further testing and analyses must be undertaken before implementing the rules, as there are concerns on the lack of ductility. This can be solved by adding more reinforcement to the section. Nevertheless, the results enable the development of new joint details in the construction industry, utilising the high load bearing capacity, and/or easier constructions.

Results from the experiments indicate that joints with rough surface provide very high load bearing capacity. Further investigations to identify all advantages are required, and the present results encourage to further testing.

REFERENCES

1. Aarup, Bendt, “Examples of CRC JointCast applications”, BA/CRC Technology, 2001, Denmark
2. http://www.spaencom.dk/ref.aspx?id=6631
3. Aarup, Bendt, “Maturity of CRC”, Aalborg Portland, 1996, Denmark
4. DS/EN 1992-1-1, Eurocode 2: Design of concrete structures – Part 1-1: General rules and rules for buildings, 3rd edition, 2008

Sample preparation, image acquisition and image analysis on interfacial transition zone of steel fiber-reinforced mortar

Siaw Foon Lee
Postdoc
Department of Structural Engineering
Norwegian University of Science and Technology (NTNU)
NO-7491 Trondheim
Norway
E-mail: siaw.lee@ntnu.no

Stefan Jacobsen
Professor
Department of Structural Engineering
Norwegian University of Science and Technology (NTNU)
NO-7491 Trondheim
Norway
E-mail: stefan.jacobsen@ntnu.no

ABSTRACT

A good sample preparation for steel fiber-reinforced mortar is very important mainly for the quantification of porosity and microstructure in the interfacial transition zone (ITZ) using backscattered electrons imaging analysis (BSE-IA). Due to the ductile behaviour of steel fiber, artifact such as smearing or imperfect cut at the edge of steel fiber could happen, and this could affect the microstructure examination in the ITZ between steel fiber and matrix. Through trial, an improved grinding and polishing procedure with short duration for obtaining steel fiber-reinforced mortar specimen (water/cement (w/c) ratio of 0.3 and 0.5) with minimum artifact is found. Scanning electron microscopy (SEM) settings for backscattered electrons image acquisition and an image analysis technique for porosity and microstructure quantification are proposed. Countermeasures that minimize artifacts during sample preparation are also discussed. It is found that the neighbouring aggregates, depending on their geometries and arrangements, can disturb the trend of the porosity in the ITZ. Profiles of porosity and unhydrated cement in the ITZ of steel fiber are presented.

Key words: Microstructure, Interfacial Transition Zone, Backscattered Electrons Imaging, Secondary electron microscopy, steel fibre-reinforced mortar

1. INTRODUCTION

Quantification of porosity and microstructure features in cementitious materials using the backscattered electron (BSE) imaging technique has widely been adopted [1, 2, 3]. For BSE-IA, a good sample preparation that gives a flat-polished surface with minimum artifact is essential as topographical variations or severe artifacts can appear as features that overlap with the important features on the greyscale histogram in the BSE image analysis. Therefore, misinterpretation of features in image analysis could possibly happen.

For porosity study using BSE-IA, epoxy impregnation is an important step because pores that are filled with epoxy will appear black in the BSE image, and this allows the segmentation of porosity from the hydration products to be done easily. In addition, epoxy impregnation reduced possible cement hydrate from washing out during polishing. Examining specimen in the conventional scanning electron microscopy (SEM) with vacuum condition tends to introduce microcracking on the specimen. The cracking of hardened cement paste caused by drying and vacuum impregnation during preparation is another concern [4, 5, 6]. Solutions for that are impregnating epoxy by ethanol replacement procedures to avoid vacuum impregnation as proposed by Struble et al. [7] or examining specimen under environmental scanning electron microscopy (ESEM) [8]. The formation of ITZ caused by the wall effect is reported as a weak region in mortar/concrete due to a significant high porosity found in that region [9, 10]. Therefore, it is essential to have a good sample preparation to preserve the original features in the ITZ without losing any information.

Mortar is a multiphase material with different hardness and elastic modulus of each phase [11, 12]. Incorporation of steel fiber into mortar means that an additional phase is added into it and steel fiber has high ductility and different hardness compared to cement paste [13, 14]. Thus, this makes the grinding and polishing for steel fiber-reinforced mortar specimen become relatively more tedious. Methods such as electrical discharge machining (EDM) and grinding technique for steel reinforcing bar [15] are not suitable for steel fiber-reinforced mortar specimen due to the random arrangement of steel fibers during mixing and also the sizes of steel fibers are on the milli-scale. Furthermore, most of the literature on sample preparation is for cementitious materials without the incorporation of steel fibers and the detailed procedure is not clearly mentioned [7, 16].

In this paper, a detailed and improved grinding and polishing procedure with short duration for steel fiber reinforced mortar specimens, SEM settings for image acquisition and an image analysis technique are presented. The porosity and microstructure in the ITZ between steel fiber and matrix for w/c 0.3 and 0.5 mortars was quantified.

2. EXPERIMENTAL PROCEDURE

2.1 Materials

Two steel fiber-reinforced mortars with w/c 0.3 and 0.5, with 0.3 vol % straight high carbon steel fibers from ref. [14] were used. They were cast into 40x40x160 mm moulds, covered with plastic bag straight after casting, demoulded after 24 hours and cured in water at 20 ℃ for 28 days. The materials used in the mix proportion were Norcem Anlegg cement (an Ordinary Portland cement in Norway), water, limestone filler, a polycarboxylate polymers

superplasticizer (Glenium 151), sand 0-2 mm, sand 0-4 mm and steel fiber with the ratio 1.00:0.30:0.09:0.02:0.45:2.58:0.04 for w/c 0.3; 1.00:0.50:0.11:0.01:0.60:3.40:0.06 for w/c 0.5, measured in kg/m^3, assuming 2 vol% air void and fraction of matrix (all materials with particles' sizes < 0.125 mm) = 41% by volume. The length and diameter of the steel fiber was 13 mm and 0.16 mm respectively.

2.2 Initial preparation and grinding

After 28 days, small cubes were cut from the mortars and cleaned from any contamination and dried at 20 ℃ and 50% RH before epoxy mounting to enhance the adhesion between the resin and the cubes. Depending on research interest, small cubes can be cut from either the center, top, bottom or the side of concrete using a low-speed diamond saw with water as lubricant. For grinding and polishing, a specimen holder of 160 mm diameter with six mounts of 25 mm diameter was used. The dimension of the cube was determined in such a way that the cube surface area was around 50% of the mount area [17]. In our study, the cube dimension was around 16x16x16 mm, which formed a surface area of around 52% of the mount area. A Struers TegraPol-31 grinding and polishing machine with adjustable rotational speed and polishing pressure was used.

The surface of the cube was examined and any protruding steel fiber from the surface was cut. For easy handling and perfect edge retention during grinding and polishing, the cube was cold-mounted into epoxy resin. The examined surface of the cube was put face down in a 25 mm diameter mounting cup. Araldite Standard Epoxy resin with bas and hardener in ratio 1:1 were blended well and then poured into the mounting cup. The cube with epoxy in the mounting cup was clamped at the edge of a table to prevent a massive amount of epoxy from flowing underneath the cube. The epoxy was cured at 20 ℃ for at least 24 hours before the specimen was removed from the mounting cup.

A preliminary grinding and polishing force and duration can be worked out from the Metalog User's Guide [17] by looking into the hardness and ductility of the specimen and the number of specimens ground or polished at a time. Since steel fiber reinforced mortar is a composite material and the specimen made in the study consisted of about 60% aggregates, therefore, the hardness of aggregate was used as a reference for the preliminary selection of grinding and polishing force and duration. It is necessary to perform a trial on the preliminary selection of force and duration on a specimen prepared for the first time.

To ensure a plane surface on the SEM holder, the base of the specimen was dry ground by hand for a few minutes on a Struers Silicon Carbide MD-Piano 600 that gave a 30 μm final surface flatness. The examined surface was ground using Struers Silicon Carbide MD-Piano 220 (68 μm), MD-Piano 600 (30 μm), MD-Piano 1200 (14 μm) and MD-Largo (9 μm) at 150 rpm, see Table 1 for lubricant/abrasive, force and duration used. Fig. 1 shows the surface image of a new epoxy-mounted specimen in a reflected light microscope at x10 x10 magnification. The image revealed a layer of epoxy on the polished surface that was very difficult to be noticed by naked eyes. Therefore, it is advisable to grind the surface on MD-Piano 200 for a few times to get rid of the epoxy layer and to achieve the entire surface flatness of 68 μm before proceeding to next step. The specimen was cleaned ultrasonically in water for about 2 minutes to remove grit and debris, and then it was examined in a reflected light microscope to spot any artifact due to the previous grinding.

Sample preparation for cementitious materials without steel fiber was normally ground down to 14 μm diamond grit before epoxy impregnation [16]. For steel fiber-reinforced mortar, specimens were ground with diamond grit down to 9 μm, and if necessary, with grit smaller than 9 μm. Fig. 2 shows that for the specimen with final grinding at 9 μm, steel fibers have fine circumferences for epoxy impregnation, however, with grit larger than 9 μm, an imperfect cut was seen on the edges of the steel fibers, and this will affect the study of porosity and microstructure in the ITZ very close to steel fibers. We therefore recommended grit $\leq$ 9 μm for final grinding.

Table 1 – Grinding discs, polishing cloths, lubricant/abrasive, force and duration in our study.

1) MD-Grinding Disc	**Lubricant/Abrasive**	**Force (N)**	**Duration (min)**
MD-Piano 220 (68 μm diamond)	Water	20	2
MD-Piano 600 (30 μm diamond)	Water	20	2
MD-Piano 1200 (14 μm diamond)	Water	20	2
MD-Largo	Ethanol/9 μm diamond grit suspensions	15	2
2) MD-Polishing Cloths			
MD-Plan	Blue Ethanol /6 μm diamond grit spray	10	2
MD-Dur	Ethanol /3 μm diamond grit suspensions	10	2
MD-Dac	Ethanol /1 μm diamond grit suspensions	10	2
MD-Nap	Blue Ethanol / ¼µm diamond grit spray	10	1

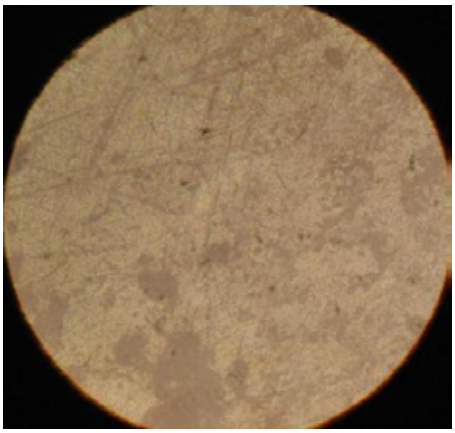

Figure 1 – The surface texture of a specimen after epoxy mounting in the reflected light microscope at x10 x10 magnification.

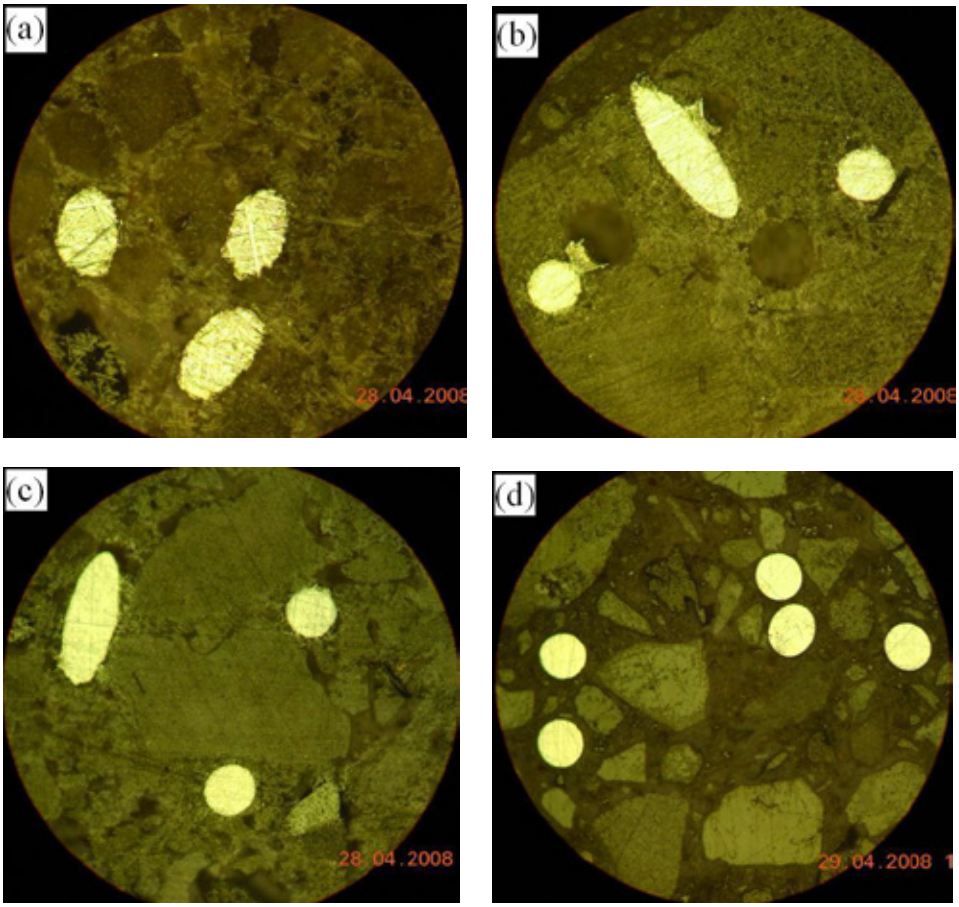

Figure 2 – The surface texture of steel fiber reinforced mortar specimen taken under the reflected light microscope at x10 x10 magnification after the grinding of (a) MD-Piano 220 (68 µm), (b) MD-Piano 600 (30 µm), (c) MD-Piano 1200 (14 µm), and (d) MD-Largo (9 µm).

2.3 Epoxy vacuum impregnation

Before epoxy vacuum impregnation, the specimens were dried in a ventilated oven at 30 ℃ for 2 days. Drying and vacuum impregnation have a significant risk for introducing cracking of hardened cement paste, but was chosen as cracking is not part of this study. The thickness of the specimen before and after epoxy impregnation was measured using a high-precision caliper to control the amount of the excessive epoxy that should be removed from the specimen surface before polishing.

The low-viscosity Epo-tek epoxy 301 and Epo-tek hardener in ratio 4:1 were mixed well in a small bottle. The entrapped air in the mixed epoxy was sucked out by putting the bottle in a vacuum chamber prior to impregnation. The specimen with its face-up surface and the bottle with epoxy were put in the vacuum chamber pumped down to 40 mbar. The bottle was clamped and could be rotated freely using a handle outside the vacuum chamber. The epoxy was poured slowly onto the top of the specimen to fully cover the whole surface. The epoxy was set for about 10 minutes in the vacuum chamber before air was let gradually in to push it down into the

specimen. To achieve full bond strength, the epoxy was then cured in a temperature chamber at atmospheric pressure at 40 ℃ for at least 24 hours.

The excessive epoxy was removed using a diamond surface grinding wheel until about 20 μm thick of epoxy remains on the top of the specimen. The specimen was then hand ground with MD-piano 600 and 1200, at low rotation speed 150 rpm with water as lubricant, until its thickness became about the same as the thickness measured before epoxy impregnation. The specimen was cleaned ultrasonically in ethanol for around 2 minutes after each grinding to remove the grit and debris.

Extra care not to grind beyond the epoxy intrusion depth on low w/c specimen needs to be taken, as a low w/c or high performance concrete, has a low permeability, and thus the epoxy intrusion depth is shallow. For specimens ground below the epoxy intrusion depth, the cavities unsaturated with epoxy when examined in the reflected light microscope will appear darker gray, see Fig. 2 in ref. [16]. Kjellsen et al. [16] showed that for specimens dried at 40 ℃ and next at pumped-down pressure of 30 mbar, the epoxy intrusion depth for w/b 0.4 without silica fume (sf) was ~120 μm, with sf was ~100 μm, while for w/b 0.25 without sf was ~70 μm, with sf was ~40 μm.

2.3 Final polishing

MD-Largo (9 μm), MD-Plan (6 μm), MD-Dur (3 μm), MD-Dac (1 μm) and MD-Nap (1/4 μm) were used for final polishing at the low rotation speed of 150rpm, see Table 1 for lubricant/abrasive, force and duration used. The same consideration of polishing the surface more than twice, if necessary, was applied to the specimen after epoxy vacuum impregnation, see Fig. 3, in order to remove the epoxy on the entire surface before proceeding to the next step. After each polishing, the specimen was cleaned ultrasonically in ethanol for around 2 minutes to remove the grit and debris, and the polished surface was examined in a reflected light microscope for any artifact incurred or polished below the epoxy intrusion depth.

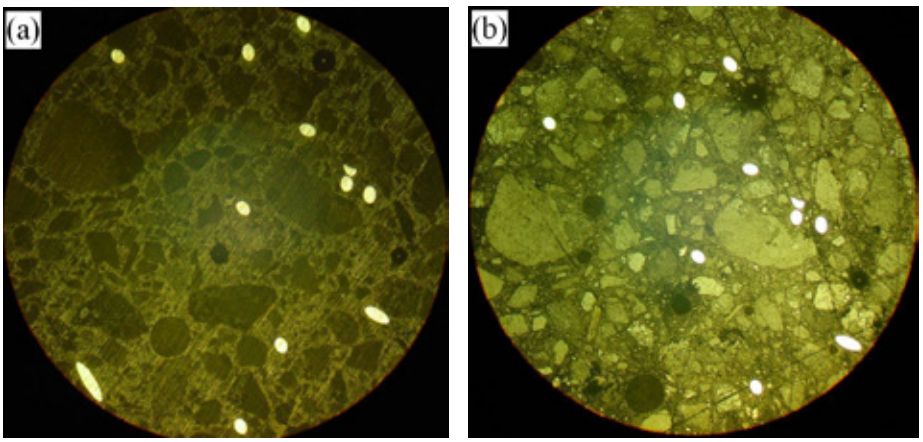

Figure 3 – Images taken at x10 x2.5 magnification in a reflected light microscope. (a) Aggregates appear homogenous in colour after epoxy impregnation and hand grinding. This indicates that a thin layer of epoxy still on the polished surface. (b) Aggregates appear inhomogeneous in colour after 9μm polishing indicates that the thin layer of epoxy has been completely removed.

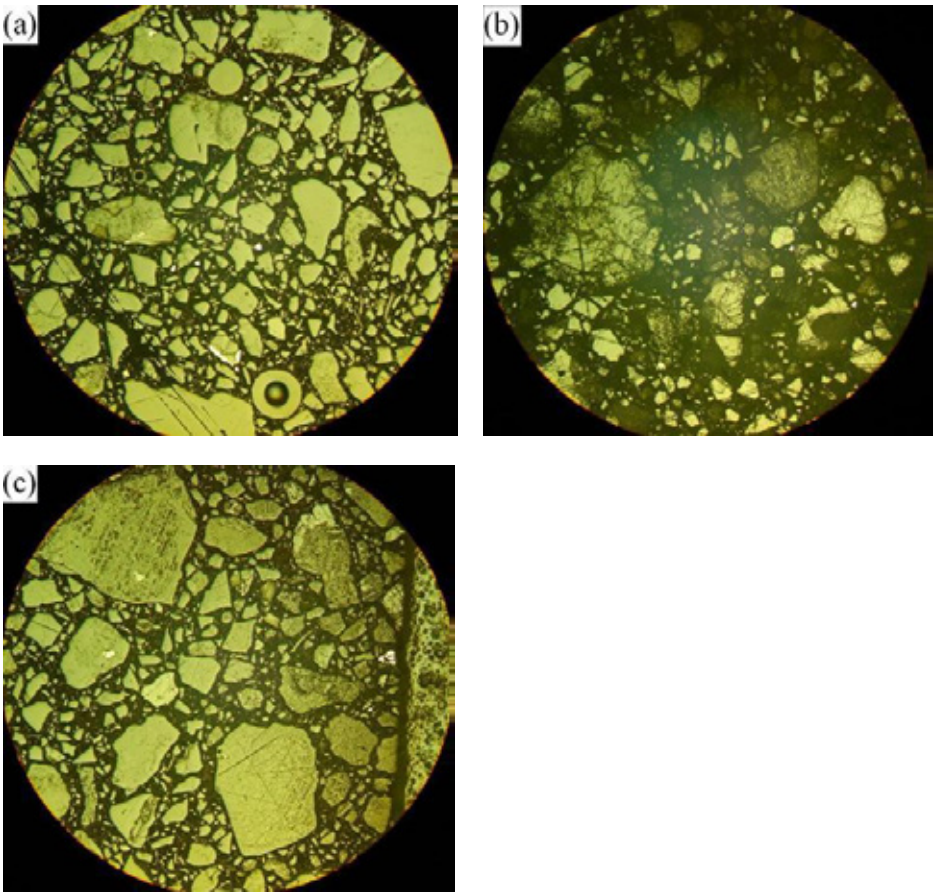

Figure 4 – Images taken at x10 x2.5 magnification in a reflected light microscope. (a) Scratches after 1 µm diamond grit polishing. (b) Scratches and contamination after 9 µm diamond grit polishing (c) Edge rounding on the left side of image.

A bright homogeneous field of view, see Fig. 1 in ref. [16], will be seen if no artifact presents on the polished surface. Countermeasures in section 5.1 or in the Metalog User's Guide [17] should be taken immediately before proceeding to the next polishing if artifacts were spot. From experience, the operator's persistence and patience is highly important to obtain a polished surface with minimum artifact.

3 SECONDARY ELECTRON MICROSCOPY AND FEATURE SEGMENTATION

For image acquisition using SEM, the polished surfaces of the specimens were sputter coated with a layer of carbon using the Cressington 208Carbon High Vacuum Turbo Carbon Coater. The body of the specimen not coated with carbon was wrapped with a strip of aluminium foil so that a complete conducting path of electrons was ensured when scanned by the electron beam, avoiding distorted images.

After coating, specimens should be kept in an air-tight container to prevent any dust resting on the polished surface. Fig. 5 shows that an identified particle resting on the steel fiber surface in secondary election (SE) image, however, appears as a topographic difference in backscattered electron (BSE) image.

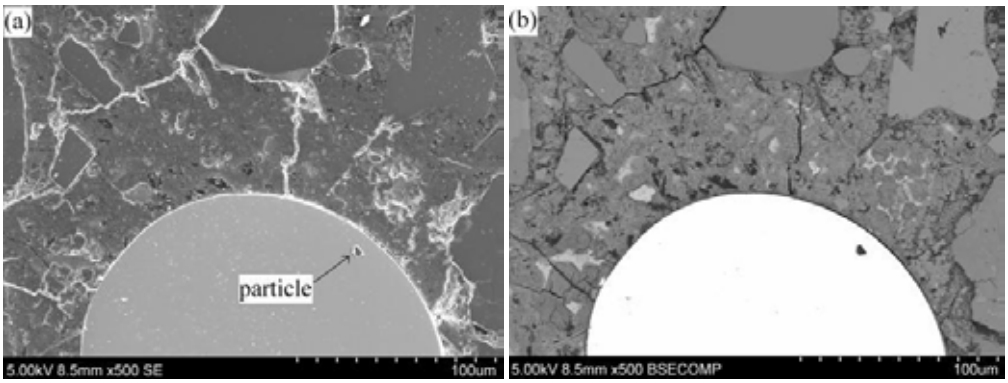

Figure 5 – An identified particle on the steel fiber in the SE image (a) but appears as a topographic difference in BSE image (b).

A Hitachi S-3400N LV-SEM equipped with Oxford INCA software was used. The microscope was operated at an accelerating voltage of 5 kV with working distance about 8 mm. The focusing and astigmatism corrections of images were carried out in the SE detector first. When a sharp image was obtained, it was changed to the BSE detector for image acquisition. The BSE COMP mode with black for 0 and white for 255 on the greyscale was chosen as it allows the exploitation of image compositions according to their atomic number contrasts. The BSE images were taken at a magnification of 500x in low vacuum. Each image was digitized at 2560x1920 pixels with a resolution of 0.1 μm/pixel.

The Oxford INCA Feature was used to assist the setting of the limit of the brightness and contrast required for taking BSE images. First, the contrast was turned to zero and the brightness was adjusted until its intensity lined up on 0 in greyscale shown on the Oxford INCA Feature. After that, the contrast was varied slowly until the histograms spread throughout the greyscale, but not beyond the upper limit of the greyscale.

It was essential to know the constituents of the specimen studied so that segmentation of features could be performed on OXFORD INCA Feature to see how well the histogram was spread throughout the greyscale, see Fig. 6. The right peak on the histogram referred to the steel fiber. In our study, since the phase of the steel fiber was not important in the ITZ image analysis, it was made to disappear at the upper limit of the greyscale without losing any necessary phases of the features wanted by slightly increasing the contrast.

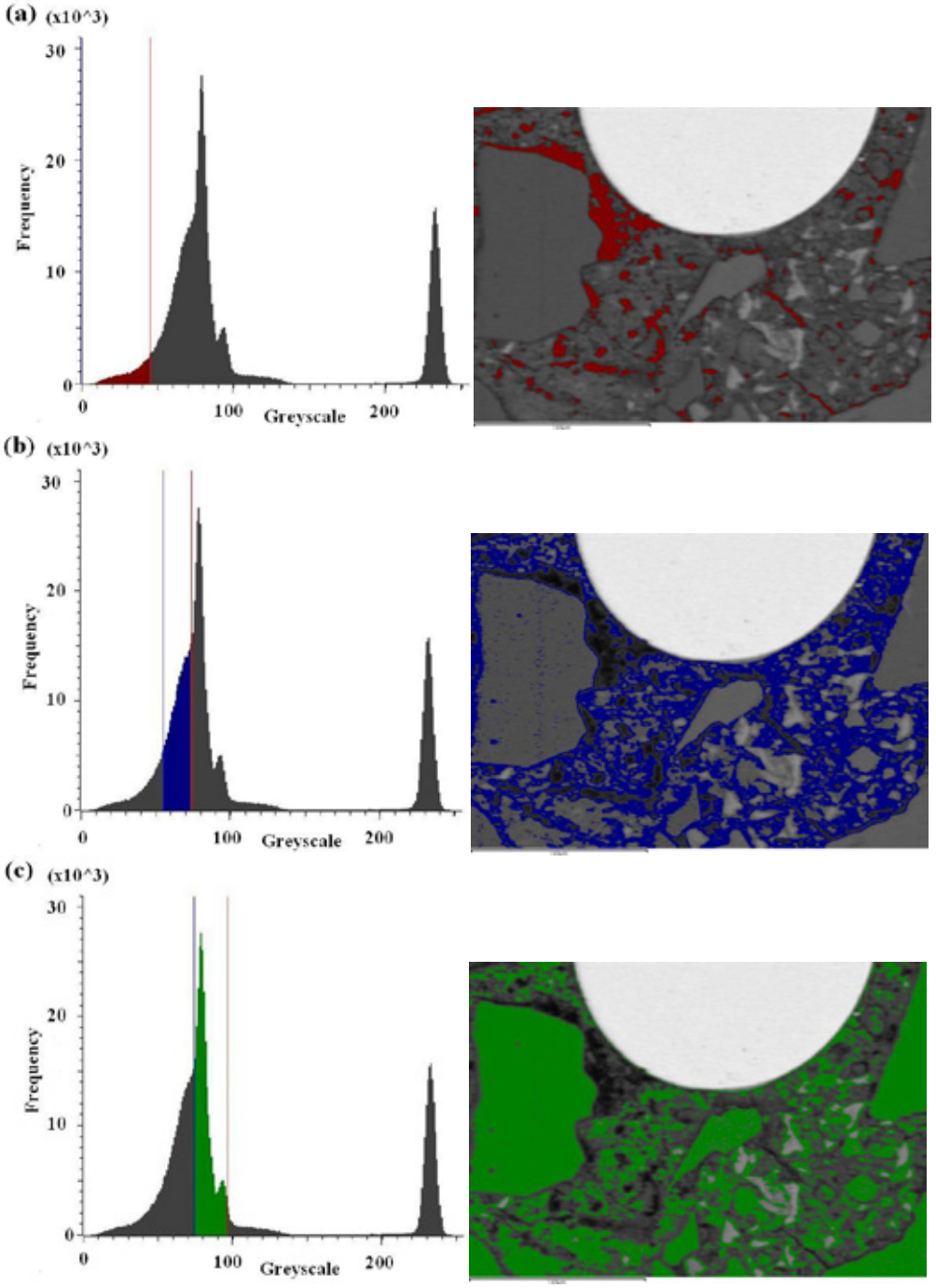
(a) (x10^3)
30
20
10
0
Frequency
0
100
200
Greyscale
(b) (x10^3)
30
20
10
0
Frequency
0
100
200
Greyscale
(c) (x10^3)
30
20
10
0
Frequency
0
100
200
Greyscale

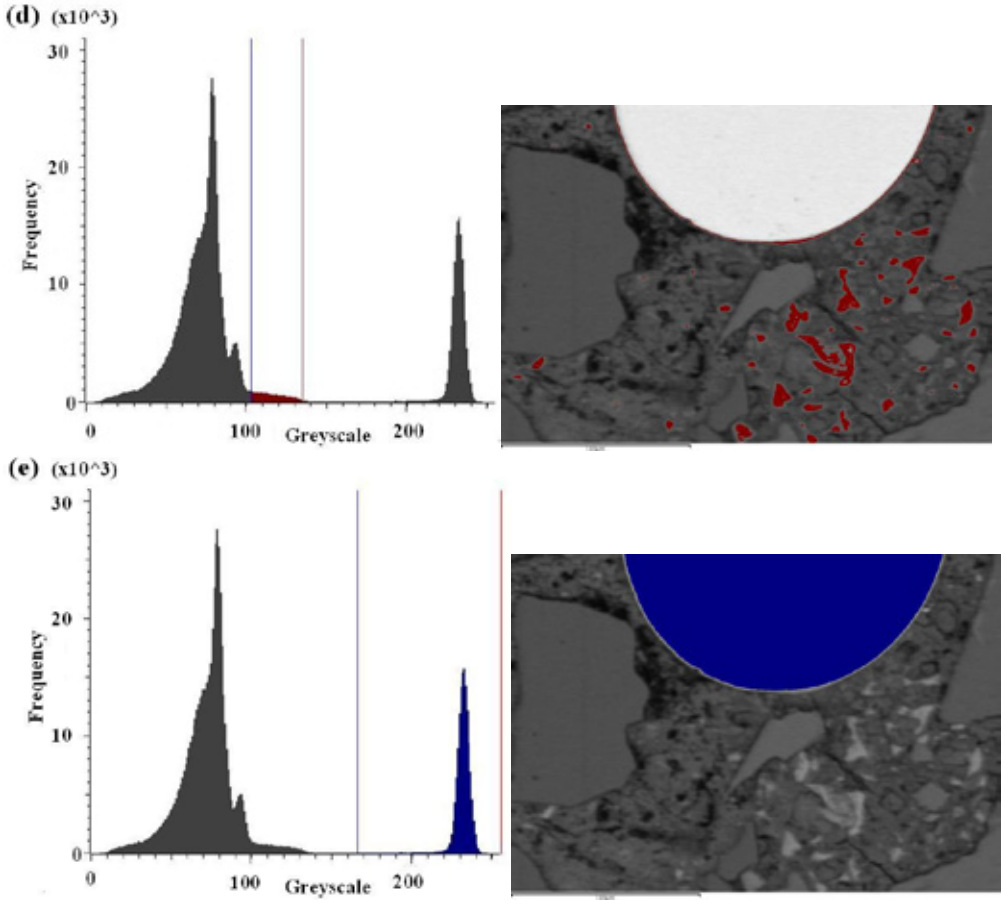

Figure 6 – Segmentation of features is done by setting individual grey threshold on the histogram on OXFORD INCA Features. (a) porosity, (b) hydration products, (c) aggregates + calcium silicate hydrate, (d) unhydrated cement grains, and (e) steel fiber.

For performing segmentation of features in the image analysis, firstly, 10-μm wide strips were cut successively from the image starting at the edge of the steel fiber using the magnetic lasso tool in Adobe Photoshop software, see Fig. 7. All strip images were saved at 2560x1920 pixels, 8 bit greyscale mode and in jpg format. The number of strips cut successively from the edge of steel fiber depends on the individual interest. The maximum thickness of ITZ in concrete has been claimed to range from 15 μm up to 50 μm[18, 19], depending on the age and the amount of binder used in the mix proportion.

The ITZ strips were then analyzed using analySIS®. Segmentation of features was performed on the images by defining a range of grey value for each feature. The individual feature was then measured in area fraction. The grey-value ranges of features obtained from the first-strip analysis were applied to the rest of the strips cut from the same image. In this stage, only segmentation of features was performed. No effort was made to enhance the contrast of the image taken.

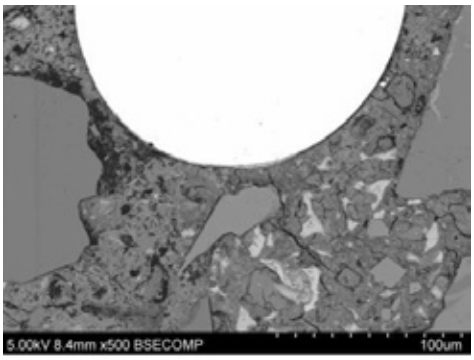

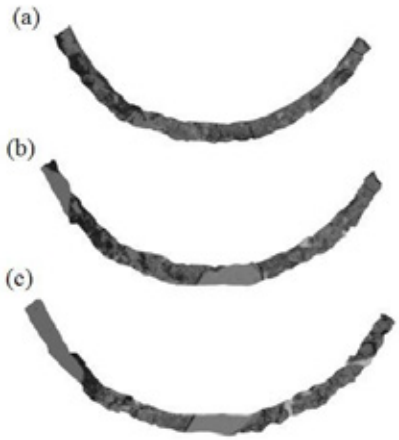

Figure 7 – 10-µm wide strips were cut successively from the edge of steel fiber in Adobe Photoshop software.

4 DISCUSSION

4.1 Sample preparation

In our study, small cubes were selected from the central portion of 40x40x160 mm prism. A grinding trial on a new steel fiber reinforced mortar specimen was performed using a series of SiC papers and MD-grinding discs. It was found that for SiC paper the polished surface was convex, while for MD-grinding discs the polished surface was flat when examined under a strait edge.

For porosity quantification on cementitious materials, epoxy impregnation is necessary as epoxy with its low atomic number, Z=6 (contains mainly carbon), appears as black in backscattered electrons image, and thus separating pores from other phases. In addition, pores filled with epoxy minimizes incidents damaging the surface such as washing out of cement hydrates during wet polishing, cement grains plucking out from the surrounding of the pores and steel fiber pull-out during sample preparation.

From experience, we discovered that although epoxy impregnation helped to stabilize the microstructure and porous structure, certain countermeasures as below should be taken during sample preparation to prevent artifacts such as scratches, edge retention, relief and contamination. 1) Grinding or polishing specimens for more than 3 minutes should be avoided as debris and grit may accumulate on the discs or cloths and scratch the polished surface. Furthermore, keeping polishing time short reduced relief and thermal damage on the polished surface 2) Proper concentration of lubricant and diamond grit should be ensured during polishing. Scratches were commonly seen when too little lubricant was present in the concentration, see Fig. 3(b) and Fig. 4(a) and (b). It is advisable to shake the bottle well before polishing. 3) Ethanol is used as lubricant for polishing and also for cleaning specimens after each stage to avoid dissolving calcium hydroxide (CH). However, epoxy is soluble in ethanol [20]. Ultrasonically treatment of specimens too long in ethanol or too much polishing on the same specimen in a day tends to soften the mounting epoxy. 4) Grinding discs and polishing cloths should be washed properly after use. Otherwise, contamination can be seen on the polished surface, see Fig. 4(b). Although contamination can be removed easily at the next polishing step, extra work is needed to ensure that it does not influence the following surface flatness.

Final polishing of the specimens was done with ¼ μm diamond grit so that topographic difference less than 1 μm could be achieved. With all these countermeasures or improvements, the risk of removing microstructure close to the interface of steel fiber was reduced during polishing. Microcracking seen along some part of the steel fiber's circumference, see Fig. 8, is most probably due to the drying causing differential volume change between paste and fiber, as reported by other researchers [8].

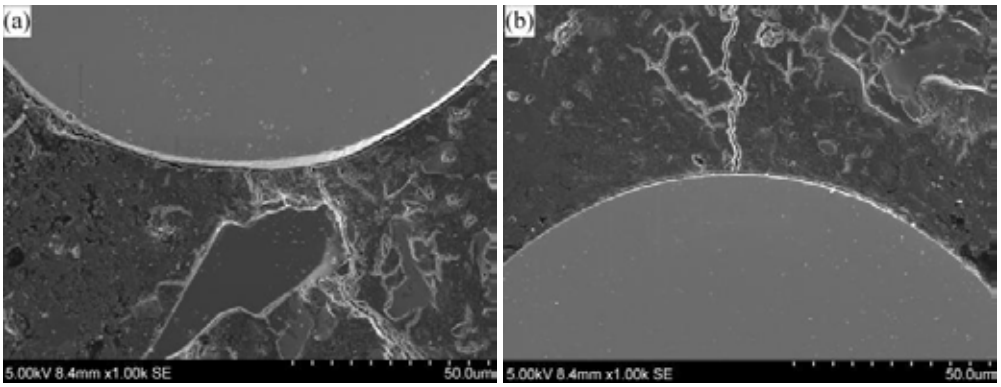

Figure 8 – A microcrack along some part of the steel fiber was observed at the lower half (a) and at the upper half (b) of steel fiber.

4.2 Image acquisition

Wong et al. [21] analyzed an image by removing aggregates from the image, revealing that for w/c 0.7 the histogram consisted of four distinct peaks that were pores, hydration products (HP), calcium hydroxide (CH) and unhydrated cement grains (UH), while for w/c 0.35 the histogram consisted of one large peak that was possibly made up of HP and CH, and one small peak from UH, however, no peak on porosity. In general, pores with epoxy appear as the darkest constituent, HP the slightly darker constituent, UH the lightest constituent on the histogram. The HP such as calcium-silicate-hydrate (C-S-H), calcium hydroxide (CH), ettringite and

monosulphate tend to merge under a single broad peak since their contrasts are too close to distinguished.

Aggregates rich in silica have similar grey threshold as C-S-H [2]. Aggregates rich in calcium have similar grey threshold as most of the HP [3]. Depending on their atomic numbers, spots that appear as the lightest constituent may overlap with the grey levels of unhydrated cement grains; whereas spots that appear as the slightly darkest constituent may overlap with the HP. Therefore, the presence of aggregates in image acquisition/image analysis will increase either the frequency of apparent C-S-H or apparent C-H on the histogram, depending on which mineral aggregates are rich in, see Fig. 9(a) for w/c 0.3 and Fig. 9(b) for w/c 0.5. In addition, for specimens with w/c 0.5 the porosity appears broad with frequency higher than that of w/c 0.3. UH is hardly seen on the histogram for w/c 0.5 when compared to w/c 0.3.

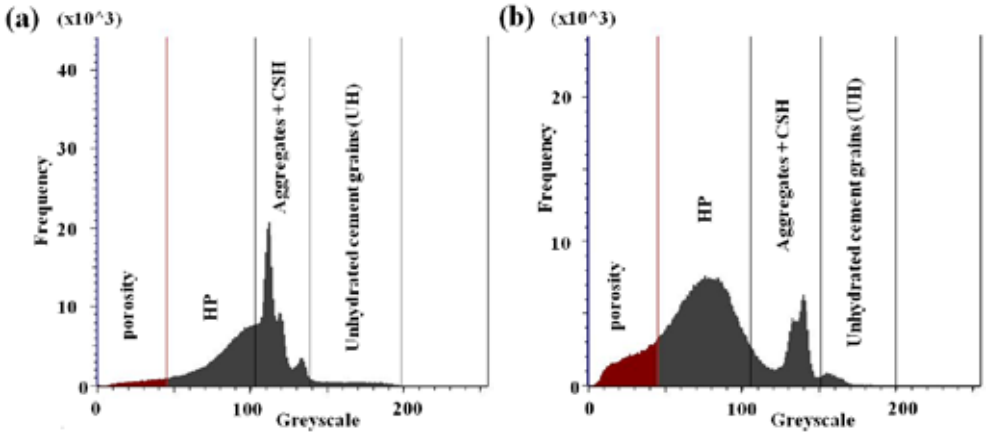

Figure 9 – Histograms for (a) w/c 0.3 and (b) w/c 0.5, with aggregates present in the image.

A high resolution BSE image is a prerequisite for segmentation of features in image analysis. To obtain a good resolution BSE image, SEM settings such as accelerating voltage, probe current, aperture, working distance, brightness and contrast, focus and astigmatism control, BSE gain and scan speed are in fact related to each other. At low acceleration voltage ($\leq$ 5 kV), the beam interacts with the region very close to the surface of the specimen. Therefore, the image detected carries information mainly on surface details. At high acceleration voltage (15-30 kV), the beam penetrates and interacts with microstructure deep into the surface of specimen. In this case, the emerging electrons carry mostly information about the interior of the specimen [22]. Since the boundaries between the constituents of cementitious materials are diffuse, the increase of accelerating voltage makes the image more blurred.

The adjustment of the brightness and contrast in SEM determines corresponding peaks on the histogram. Head et al. [21] ensured that the histogram did not spread beyond both ends of the greyscale by adjusting the brightness and contrast such that no pixel count was recorded on greyscale 0-10 and 245-255 during image acquisition. In our study, the reason to turn the contrast to zero when setting the brightness was to ensure that the required brightness intensity was set. At too high or too low brightness with unproper contrast setting, some features merged together and appeared as a broad peak on the histogram or information lost at both ends of greyscale commonly occurred. Fig. 6 and Fig. 10 show BSE images taken at the same field of a specimen, but with different brightness and contrast setting. Fig. 10 illustrated the loss of

information and feature merging when brightness and contrast were not properly set during image acquisition.

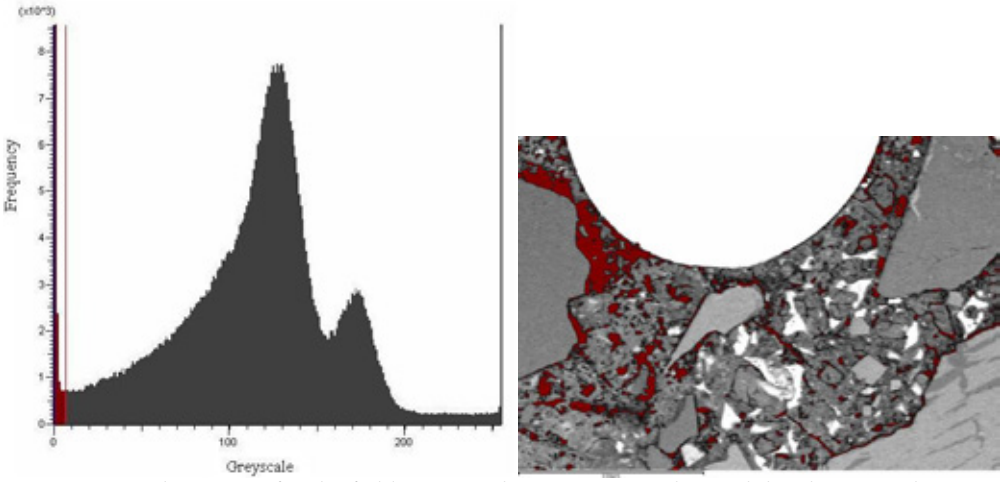

Figure 10 – A histogram for the field same as that in Figure 6, but with brightness and contrast not adjusted properly. Features merged under a broad peak and information lost at both ends of the greyscale of the histogram.

Mouret et al. [23] studied the influence of the magnification on the evaluation of the area fraction of the unhydrated cement grains and concluded that magnification between 200x to 1000x did not give any significant difference in their mean values. Scrivener et al. [24] found that a magnification of 400x for a cement paste analysis of ten fields gave a standard deviation of ~0.6%. Therefore, a magnification of 500x was used in our study and it allows also half of the diameter of steel fiber being taken for ITZ study.

4.3 Image analysis

The size of an image pixel and how accurately the features are segmented on the greyscale generally determine the image quantitative data of the features in a specimen. The brightness of a pixel is an average of all phases present in the pixel. If the brightness of two or more phases is close to each other, averaging the phases' brightness tends to broaden the peaks on the histogram. If the brightness of phases in a pixel is far from each other, the averaging gives wrong grey value of the pixel. Therefore the smaller the pixel size, the more accurate the histogram is obtained. With 0.1 μm/pixel used in our study, some fraction of fine capillary pores ranging from 0.2 μm to 2.6 nm proposed by Igarashi et al. [25] and gel pores on the nanometer mainly found in the hydrated products as Powers-Brownyard proposed [26] are impossible to be detected as individual pore in the image analysis.

For segmentation of pores on the histogram, the lower threshold level can easily be set to zero. However, it has always been a problem to set the upper threshold level because the boundary between C-S-H and large or capillary porosity is diffuse. In addition, there was no distinct peak on the porosity threshold for low w/c as already discussed. Therefore, segmentation of pores on histogram could be done mainly by individual judgment. Scrivener et al. [24] found that the threshold value at the intersection between the tangent of the lower portion of the hydration

products (HP) and the initial tangent on the histogram gave a result that matched the manual threshold value for low w/c. Head et al. [3] selected a threshold value of 42 to identify the porosity content from other phases in the image for w/c 0.3. Yang et al. [2] developed an algorithm to segment aggregates from the cement paste, then, the porosity and unhydrated cement grains can be measured effectively. Wong et al. [21], for w/c 0.7, where a clear pore peak appeared on the histogram, simply used the threshold value at the minimum frequency between the pore peak and the HP peak as the upper threshold level for pore segmentation.

In our study, manual threshold and visual checking was adopted to set the upper threshold level of porosity. In the Oxford INCA Feature, when a threshold is set on the histogram, areas in the image that corresponds to the threshold will be painted with a color. By adjusting the threshold and visual check on the coloured area, the upper threshold level of the porosity was determined. The threshold value was then used in analySIS® for pores segmentation.

4.4 Interfacial transition zone

Fig. 12 shows the area % of porosity and unhydrated cement versus the distance from the steel fiber's interface measured from the corresponding BSE images of w/c 0.3 and 0.5 in Fig. 11 using the method proposed in this paper.

From Fig. 12(a), it was observed that the porosity showed a higher value close to the edge of the steel fibers, and then reduced and reached a constant value with the distance far away from the edge for both w/c. However, w/c 0.5 showed a higher area % of porosity than w/c 0.3 for the distance of 10μm from the edge of the steel fiber. This indicated that w/c 0.5 was more porous than w/c 0.3. It was also observed that the presence of the neighbouring aggregates within the ITZ on the BSE image of w/c 0.5 disturbed the trend of the curve of the porosity. Depending on the geometry and arrangement of the aggregate, it had a possibility of increasing/decreasing the porosity in the ITZ. For w/c 0.3, without the presence of the aggregate in the ITZ, the curve of the porosity decreased and reached a plateau at the matrix. Comparing the BSE images of w/c 0.3 and w/c 0.5, see Fig. 11, the ITZ and the matrix of w/c 0.3 were packed more compact with hydration products and unhydrated cement grains, and had less porous areas. In line with what was expected in ref. [26] and the fact that w/c 0.3 has higher compressive strength than w/c 0.5.

For unhydrated cement, w/c 0.5 shows a low and constant value of unhydrated cement, while w/c 0.3 shows an increase with the distance away from the edge of the steel fiber, see Fig. 12(b). High area % of unhydrated cement in w/c 0.3 compared to w/c 0.5 indicated not enough water to complete the hydration. A low area % of unhydrated cement found near the surface of the steel fiber for the specimen of w/c 0.3 was mainly caused by a locally high w/c formed near the surface of the steel fiber due to the wall effect. For w/c 0.5, we believe that a locally high w/c formed at the steel fiber's surface compared to the matrix. However, due to the high water content in w/c 0.5, almost all the cement grains were hydrated, and thus a low and constant area % of unhydrated cement was observed both in the ITZ and matrix.

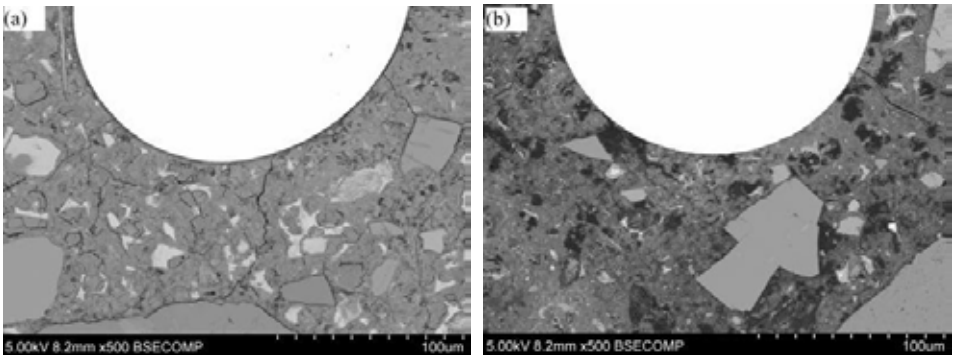

Figure 11 – BSE images of (a) w/c 0.3 and (b) w/c 0.5, and their corresponding area percent of porosity and unhydrated cement as distance from the steel fiber's interface was plotted in Figure 12.

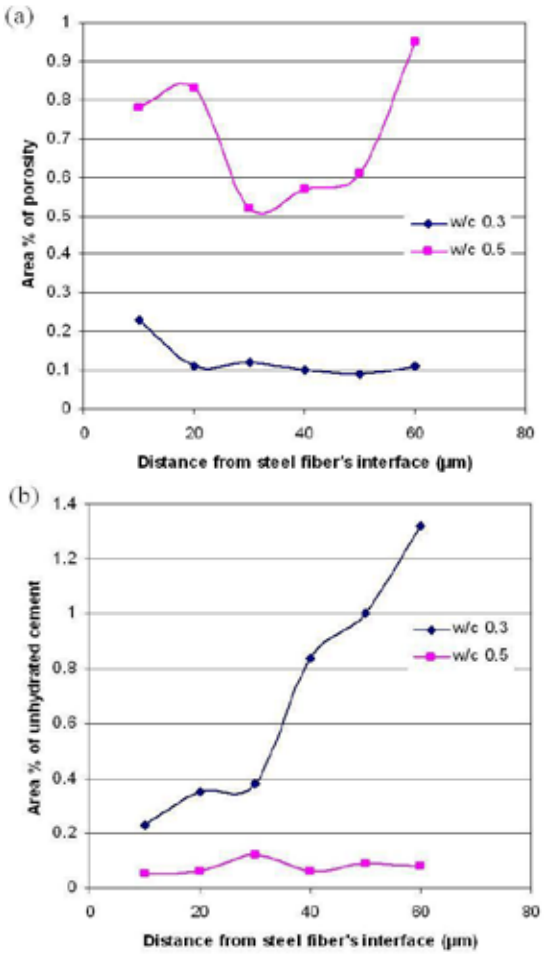

Figure 12 – Area percent of (a) porosity and (b) unhydrated cement vs distance from the steel fiber's interface for w/c 0.3 and 0.5.

5 CONCLUSIONS

For steel fiber-reinforced mortar specimen, MD-grinding discs and polishing cloths were found to improve the specimen surface flatness compared to SiC paper. Although epoxy impregnation helped to reduce microstructure pluck out and steel fiber pull-out, certain countermeasures needed to be taken during sample preparation to prevent artifacts such as edge rounding, scratches and contamination that are commonly encountered in cementitious materials.

It is essential to adjust the brightness and contrast properly in SEM so that important features do not disappear at the both ends of the greyscale during image acquisition. Any efforts to enhance the brightness and contrast of the image during image analysis were in vain.

The porosity and the unhydrated cement at the steel fiber's interface showed the same trend as function of distance as that from the aggregate's interface. The neighbouring aggregates, depending on their geometries and arrangements, had a tendency of disturbing the trend of the porosity in the ITZ. From the observation and analysis on BSE images, cement grains in the specimen with w/c 0.5 underwent more complete hydration both in the ITZ and matrix than that in w/c 0.3.

ACKNOWLEDGMENTS

We thank the funding from the Norwegian Research Councils (NRC) Institution-based Strategic Project (ISP) on focus area 3 -Sustainable Infrastructure (Grant No 177275). This work also forms a part of NTNU's contribution to the Concrete Innovation Centre (COIN) at Sintef/NTNU, starting in 2007 as a centre for research based innovation (CRI) within concrete technology with 9 industrial partners: Aker Solutions, Norcem Heidelberg, Borregaard, Maxit, Skanska, Rescon Mapei, UNICON, Veidekke and the Norwegain Road directory.

REFERENCES

1. Scrivener, K.L., Pratt, P.L., "Characterisation of portland cement hydration by electron optical techniques. In: Electron microscopy of materials", *Mater Res Soc Symp Proc*, 31, 1983 PP. 351–356
2. Yang, R., Buenfeld, N.R., "Binary segmentation of aggregate in SEM image analysis of concrete", *Cement Concrete Res*, 31, 2001 pp. 437–441
3. Head, M.K., Buenfeld, N.R., "Measurement of aggregate interfacial porosity in complex, multi-phase aggregate concrete: Binary mask production using backscattered electron, and energy dispersive X-ray images", *Cement Concrete Res*, 36, 2006 pp. 337–345
4. Gran, H.C., "Fluorescent liquid replacement technique. A means of crack detection and water:binder ratio determination in high strength concrete", *Cement Concrete Res*, 25, 1995 pp. 1063–1074
5. Mindness, S., Diamond, S., "A preliminary SEM study of crack propagation in mortar", *Cement Concrete Res*, 10, 1980 pp. 509–519
6. Chatterji, S., Thaulow, N., Christensen, P., "Formation of shrinkage cracks in thin specimens of cement paste", *Cement Concrete Res*, 10, 1981 pp. 155–157
7. Struble, L., Stutzman, P., "Epoxy impregnation of hardened cement for microstructural characterization", *J Mater Sci Lett*, 8, 1989 pp. 632–634

8. Bisschop, J., Mier, J.G.M., "How to study drying shrinkage microcracking in cement-based materials using optical and scanning electron microscopy?", *Cement Concrete Res*, 32, 2002 pp. 279–287
9. Scrivener, K.L., Crumbie, A.K., Laugesen, P., "The interfacial transition zone (ITZ) between cement paste and aggregate in concrete", *Interface Sci*, 12, 2004 pp. 411–421
10. Elsharief, A., Cohen, M.D., Olek, J., "Influence of aggregate size, water cement ratio and age on the microsturcture of the interfacial transition zone", Cement Concrete Res, 33, 2003 pp. 1837–1849
11. DeJong, M.J., Ulm, F., "The nanogranular behavior of C-S-H at elevated temperatures up to 700ºC", *Cement Concrete Res*, 37, 2007 pp. 1–12
12. Mondal, P., Shah, S.P., Marks, L.D., "Nanoscale characterization of cementitious materials", *ACI Mater J*, 105, 2008 pp. 174–179
13. Sorelli, L., Constantinides, G., Ulm, F., Toutlemonde, F., "The nano-mechanical signature of ultra high performance concrete by statistical nanoindentation techniques", *Cement Concrete Res*, 38, 2008 pp. 1447–1456
14. Wang, X.H., Jacobsen, S., Lee, S.F., He, J.Y., Zhang, Z.L., "Effect of silica fume, steel fiber and ITZ on the strength and fracture behavior of mortar", *Mater Struct*, 43, 2009 pp. 125-139
15. Garrett, H.L., Beaman, D.R., "A method for preparing steel reinforced mortar or concrete for examination by transmitted light microscopy", *Cement Concrete Res*, 15, 1985 pp. 917–920
16. Kjellsen, K.O., Monsøy, A., Isachsen, K., Detwiler, R.J., "Preparation of flat-polished specimens for SEM-backscattered electron imaging and X-ray microanalysis - importance of epoxy impregnation", *Cement Concrete Res*, 33, 2003 pp. 611–616
17. Struers A/S, Struers Metalog Guide - User's manual, Valhøjs Alle 176, DK-2610 Rødovre, Denmark, 2000.
18. Ollivier, J.P., Maso, J.C., Bourdette, B., "Interfacial transition zone in concrete review", *Adv Cem Based Mater*, 2, 1995 pp. 30–38
19. Zheng, J.J., Li, C.Q., Zhou, X.Z., "Thickness of interfacial transition zone and cement content profiles around aggregates", *Mag Concrete Res*, 57, 2005 pp. 397–406
20. Glauert, A.M., Glauert, R.H., "Araldite as an embedding medium for electron microscopy", *J Biophys Biochem Cytol*, 4, 1958 pp. 191–194
21. Wong, H.S., Head, M.K., Buenfeld, N.R., "Pore segmentation of cement-based materials from backscattered electron images", *Cement Concrete Res*, 36, 2006 pp. 1083–1090
22. Goldstein, G., Newbury, D., Joy, D., Lyman, C., Echlin, P., Lifshin, E., "Scanning Electron Microscopy and X-Ray Microanalysis", 3rd edition, Springer, 2003.
23. Mouret, M., Ringot, E., Bascoul, A., "Image analysis: a tool for the characterisation of hydration of cement in concrete - metrological aspects of magnification on measurement", *Cement Concrete Comp*, 23, 2001 pp. 201–206
24. Scrivener, K.L., Patel, H.H., Pratt, P.L., Pratt, L.J., "Analysis of phases in cement paste using backscattered electron images, methanol absorption and thermogravimetric analysis", *Mater Res Soc Symp Proc*, 85, 1987 pp. 67–76
25. Igarashi, S., Kawamura, M., Watanabe, A., "Analysis of cement pastes and mortars by a combination of backscatter-based SEM image analysis and calculations based on the Powers model", *Cement Concrete Comp*, 26, 2004 pp. 977–985
26. Powers, T.C., Brownyard, T.L., "Studies of the physical properties of hardened portland cement paste - part 5", *J Amer Concrete Inst Proc*, 43, 1947 pp. 669– 712

Mix design and the effect of silica fume and steel fiber on rheological and mechanical properties of mortars

Siaw Foon Lee
PhD, Postdoc
Department of Structural Engineering
Norwegian University of Science and Technology (NTNU)
NO-7491 Trondheim
Norway
E-mail: siaw.lee@ntnu.no

Xiao Hui Wang
PhD, Associate Professor
Department of Civil Engineering
Shanghai Jiaotong University
200240 Shanghai
China
E-mail: w_xiaoh@163.com

Stefan Jacobsen
PhD, Professor
Department of Structural Engineering
Norwegian University of Science and Technology (NTNU)
NO-7491 Trondheim
Norway
E-mail: stefan.jacobsen@ntnu.no

ABSTRACT

Mortars with water and binder ratio (w/b) 0.3 and 0.5, with and without 10% silica fume by cement weight and with 0, 0.3 and 1 vol% steel fibers were made to study the effect of silica fume and steel fiber on rheological and mechanical properties. Slump, yield stress and plastic viscosity of fresh mortars were measured. Three-point bending and compressive tests were performed on the mortars after 28-day curing. It was found that silica fume improved the cohesiveness of fresh mortars, increased the compressive strength but showed no obvious effect on the bending strength for both w/b either with or without 0.3 vol% steel fiber. The inclusion of 0.3 vol% steel fiber greatly affected the workability of fresh mortars with w/b 0.3 without silica fume compared to that with silica fume, and gave no effect on mortars with w/b 0.5. 10% silica fume and 0.3 vol% steel fiber increased the air-void content slightly. However, plots of strength as

function of air void content over a small range did not show that air void gave a general reduction of strength.

Key words: mortar, silica fume, steel fiber, rheological, mechanical properties, air-void content.

1. INTRODUCTION

Mortar has gradually become an interesting research as it forms the major component of concrete and can be used as repairing material to fill up the opening crack in the concrete. Its mechanical properties can greatly be improved with the use of fibers [1]. As a repairing material, it is important that the mortar has flowable behaviour. Although fibers reinforce the mortars by improving the ductility, arresting and preventing cracks from propagation, the inclusion of different types or vol% of fibers can greatly affect the workability of fresh mortars [2]. In addition, it is relatively difficult in designing steel fiber-reinforced mortar that has both high fluidity and good cohesiveness.

The European guidelines for self-compacting concrete [3], which was lately established as a basic guideline for mix design and test methods to quantify the properties of self-compacting concrete such as flowability, plastic viscosity, passing ability and segregation resistance, and other mix design methods proposed by different authors [2, 4] can be used as references in designing a mortar with high fluidity and cohesiveness. It is reported that for a concrete to be considered as self-compacting, the slump flow must be between 550 and 850mm [3]. Normally self-compacting concrete has less content of coarse aggregate (maximum size between 10 to 40 mm, depending on the project interest) compared to normal concrete, typically around 31-40% by volume [5]. Okamura et al. [6] proposed a rational mix-design method for self-compacting concrete with coarse aggregate (maximum size 40 mm) content fixed at around 50 percent of the solid volume, and for self-compacting mortar with the fine aggregate content fixed at around 40% of mortar volume. According to the EFNARC guidelines [3], the amount of coarse aggregate (maximum size between 12 and 20 mm) by mass should be around 750-1000 kg/m^3 with 48-55% fine aggregate (sand) of total aggregate weight, and the sizes of aggregate particles smaller than 0.125 mm are considered as powder with the typical range of powder content 380-600 kg/m^3 in the mix design of self-compacting concrete. According to the particle-matrix method for a concrete having a high fluidity, the volume fraction of matrix, which is the volume of all particles less than 0.125 mm as well as liquid, should be more than 330 liter m^{-3} somehow depending on the w/b of concrete [7, 8].

Rheometrical methods are said to provide better workability data in terms of yield stress and plastic viscosity [9], although the rheometers are bulky, expensive and only available in a few research laboratories. The yield stress and plastic viscosity for mortar varied with temperature, time after mixing and the type of rheometer [10,11]. Therefore, for the purpose of comparison it is essential to carry out the rheological tests of all mixtures in one batch under the same condition. Nielson and Wallevik [12] proposed a self-compacting concrete zone with yield stress from 0 to 60 Pa and plastic viscosity from 20 to 120 Pas using the BML-viscometer: for self-compacting concrete having plastic viscosity below some 40 Pas, the yield stress should have significant value; for self-compacting concrete having plastic viscosity between 70 and 120 Pas, the yield value has to be close to or zero.

In general, the w/b, the amount of superplasticizer and the fine powders are the main factors that greatly influence the workability and strength of concrete or mortar. The use of fine powders and mineral fillers such as limestone powder, fly ash, silica fume, metakaolin and ground granulated blast furnace slag by replacing some part of cement, as well as viscosity-modifying admixture (VMA) can increase the resistance to segregation, reduce the cost of production and heat generation during cement hydration [13–17]. Superplasticizer is normally used along with fine powders to ensure that the workability of concrete remains the same as that without the incorporation of fine powders [18]. Although the use of superplasticizer reduces the demand of water, different concentration or different types of superplasticizer can affect the rheological properties [19] and the air-void content [20] of concrete greatly. It was reported that polyacrylate grafted with polymer (PA) superplasticizer used together with silica fume decreased the plastic viscosity, while sodium naphthalene sulphonate-formaldehyde condensate (SNF) superplasticizer used together with silica fume increased the plastic viscosity [19]. In addition, superplaticizer lengthened the setting period of mortar and the flow of mortar increased with the dosage of superplasticizer [21].

The excel-worksheet based proportioning tool, which adopts the particle-matrix method, is viewed as a faster way in designing the concrete mix proportion, and has widely been used in our laboratory for designing normal or self-compacting concretes. In this study, the proportioning tool was adopted to design four different types of high fluidity mortars, which were w/b 0.3 and 0.5 with 0, 10 percent silica fume, that could be used as a repairing material. Since it was the first time that the proportioning tool was used in designing a high fluidity mortar, a series of testings on mortar by adjusting the matrix volume, the vol% of limestone powder, fine aggregates with sizes less than 0.125 mm and superplasticizer were carried out. In the proportioning tool, the included vol% of steel fibers replaced the removed vol% of aggregate. Therefore, it was expected that the workability of fresh mortar with and without steel fiber at the same w/b should remain unchanged. 0.3 and 1 vol% of steel fibers were included into the fresh mortars at two different w/b. The slump and the rheological tests were performed to study the effect of silica fume and steel fiber on the workability of fresh mortars. On top of that, the mix design, the density, the effect of silica fume and steel fiber on mechanical properties, and the effect of air-void content on strength were also studied.

2. Experiments

2.1 Materials and mix procedures

Mortars with w/b 0.3 and 0.5 with and without silica fume 10% by cement weight were made with the mix proportions shown in Table 1, using the excel-worksheet based proportioning tool [7]. The materials used were Anlegg cement (an ordinary Portland cement commercially available in Norway), silica fume, limestone powder, sand 0-4 mm and sand 0-2 mm with their sieve analyses and fineness moduli shown in Table 2, polycarboxylate polymer super-plasticizer with 15% solid content and straight high carbon steel fibers (length 13 mm and diameter 0.16 mm, aspect ratio = 81, tensile strength = 2000 Nmm^2, Bekaert OL13/.16, see Fig. 1). The chemical compositions of the cement, silica fume and limestone powder are listed in Table 3. 0, 0.3 and 1 vol% of steel fiber were incorporated into the mortars. It made up all together four groups: A with w/b 0.3 and 0% silica fume (Mix 1, Mix 2 and Mix 3), B with w/b 0.3 and 10% silica fume (Mix 4 and Mix 5), C with w/b 0.5 and 0% silica fume (Mix 6 and Mix7) and D with w/b 0.5 and 10% silica fume (Mix 8 and Mix 9). All mixes had 41 vol% matrix (all liquids and

powders < 0.125 mm) excluding air voids.

The following procedures were used to mix the mortars with a total mixing time of 11 minutes: 1) Sands, cement, limestone powder and silica fume were added into a 10-litre flat-bottomed mixer with a counter current paddle and blended for 1 minute at low speed. 2) With the mixer running, water and superplasticizer were added simultaneously and slowly into the mixture in duration of around 30 seconds and then followed by steel fibers. The mixer was stopped after 4-minute mixing. 3) The mixture was left to set for 5 minutes and any powder that stuck on the wall of the mixer was spaded down into the mixture. 4) The mixture was then blended for another 1 minute.

The density, air void, slump tests, rheological tests and casting fresh mortars into steel moulds were performed straight after the mixing.

Figure 1 – Bekaert OL13/.16 Straight high carbon steel fibers.

Table 1 – Mix proportions of plain and steel fiber-reinforced mortars with w/b 0.3 and 0.5 using an excel-worksheet based proportioning tool [7].

	Water/binder = 0.3					Water/binder = 0.5			
	A			B		C		D	
Materials	Mix 1	Mix 2	Mix 3	Mix 4	Mix 5	Mix 6	Mix 7	Mix 8	Mix 9
Cement (kg/m^3)	542.5	543.0	543.9	483.4	483.8	411.2	411.5	367.9	368.2
Silica fume (kg/m^3)	-	-	-	48.3	48.4	-	-	36.8	36.8
Silica fume (% by cement weight)	-	-	-	10	10	-	-	10	10
Limestone powder (kg/m^3)	47.2	47.2	47.3	47.4	47.4	47.3	47.3	47.8	47.9
Water (kg/m^3)	162.7	162.9	163.2	159.5	159.7	205.6	205.7	202.3	202.5
Sand 0-4mm (kg/m^3)	1406.8	1399.1	1382.1	1406.8	1399.4	1406.8	1399.4	1406.8	1399.4
Sand 0-2mm (kg/m^3)	248.3	246.9	243.9	248.3	246.9	248.3	246.9	248.3	246.9
Superplasticizer (kg/m^3)	11.4	10.9	11.4	12.1	12.1	4.9	4.9	6.4	6.4
Superplasticizer (% by cement weight)	2.1	2	2.1	2.5	2.5	1.2	1.2	1.73	1.73
Steel fiber (kg/m^3)	-	24.2	78.0		23.4	-	23.4	-	23.4
Steel fiber (vol%)	-	0.3	1	-	0.3	-	0.3	-	0.3
Designed air-void content (vol%)	2	2	2	2	2	2	2	2	2
Matrix (vol%)	41	41	41	41	41	41	41	41	41
Density (kg/m^3)	2409	2425	2460	2396	2411	2320	2335	2311	2326

Table 2 – Sieve analysis and physical properties of the fine aggregates.

Sieve size (mm)	Sand 0-2mm	Sand 0-4mm
8	100	100
4	97.3	98.9
2	91.8	85.9
1	82.7	65.6
0.5	68.1	40.9
0.25	47.4	19.1
0.125	23.6	6.1
Fineness modulus	1.51	2.37
Specific gravity (g/cm^3)	2.65	2.65

2.2 Slump and slump flow measurements

A mini slump cone with 80 mm diameter at base, 40 mm diameter at top and 120 mm high as shown on the left side of bottom photo of Fig. 7 - Fig. 10 was used. The steel tamping rod was 8 mm diameter, 274 mm long and rounded at both ends. The fresh mortar was added into the slump cone in three layers, with each one-third of the cone height. Every layer was tamped for 25 times using the steel tamping rod before a new layer was added. For the last layer, the fresh mortar was added fully to the top of the cone. After 25-time tamping on the last layer, any excess mortar on the top of the cone was removed using the steel tamping rod until flat. The cone was then lifted slowly (around 1 to 2 seconds) in vertical direction. After the mortar stopped slumping, the steel rod was put on the top of the cone placed closed to the mortar and the slump, which was the distance from the bottom edge of the steel rod down to the top of the center of the mortar, was measured. The mean diameter of the slump flow, which was the average of two readings in perpendicular direction, was taken and shown in Table 4. Photos of the nine fresh mortars after slump were shown in Fig. 7 - Fig. 10.

Table 3 – Chemical compositions of the cement, silica fume and limestone powder.

Analysis %	Cement	Silica fume	Limestone powder
CaO	63.50		79.80
SiO_2	20.65	>90	12.87
Al_2O_3	4.70		2.68
Fe_2O_3	3.51		2.04
SO_3	3.16		
MgO	1.83		1.84
K_2O	0.47		0.62
Na_2O	0.28		0.49
P_2O_5	0.11		
Loss of ignition		>3	37.66
Specific gravity (g/cm^3)	3.12	2.20	2.70
Specific surface area (m^2/kg)	372		362

2.3 Rheological parameters and air-void content measurements

Yield stress (τ_0) of fresh mortar refers to the necessary starting force needed to move the mortar,

and plastic viscosity (μ) of the fresh mortar refers to the resistance against an increase in moving speed. Both parameters were measured using a coaxial cylinder ConTec Viscometer 4 controlled by computer software, with a 21-mm gap between the outer and the inner cylinder, see Fig. 2. The outer cylinder was made with a steel lining with the same saw-tooth profile as the rubber lining used by Wallevik [22]. The measurements were based on the Bingham equation as below:

$$\tau = \tau_0 + \mu\dot{\gamma} \tag{1}$$

where τ is shear stress, τ_0 is yield stress, μ is plastic viscosity and $\dot{\gamma}$ is shear rate. The rheological measurements of nine mortars, as shown in Table 4, were carried out in the same coaxial cylinder ConTec Viscometer 4 straight after mixing, in the same laboratory and under the same temperature so that the systematic errors on the nine mortars could be maintained as constant as possible.

The air-void content and the density of fresh mortar were measured using a pressure-type air meter in Fig. 3 with the volume of the container which is 1000 cm^3, and the values are shown in Table 4 as fresh(pressure) under the column of air-void content and density. The following equation, which is in volume percent (vol%), was used to calculate the air-void content of fresh and hardened mortar:

$$\lambda = \left(1 - \frac{\rho}{\rho_{theory}}\right) \times 100 \tag{2}$$

where λ can be either the air-void content of fresh, 24-hour hardened mortar (λ_{24h}) or 28-day hardened mortar (λ_{28d}), ρ can be either the density of hardened mortar after 24-hour (ρ_{24h}) or after 28-day (ρ_{28d}) curing, and ρ_{theory} is the theoretical void free density of the designed mortar.

Figure 2 – The coaxial cylinder ConTec viscometer 4 controlled by computer software.

Figure 3 – Pressure-type air meter used for measuring the air-void content and the density of fresh mortar in our study.

2.4 Density of hardened mortar calculation

The weights of 24-hour and 28-day hardened mortars were measured in air, W_{air}, and in water, W_{water}, in the unit of gram using the Mettler PM6000 balance.

Then, the density of hardened mortar was calculated using the following equation,

$$\rho = \frac{W_{air}}{W_{air} - W_{water}} \times \rho_w \quad (3)$$

where ρ is in kg/m^3 and can be either the density of 24-hour hardened mortar (ρ_{24h}) or 28-day (ρ_{28d}), and ρ_w is the density of water.

2.5 Mechanical tests

50x50x50 mm cubes and 40x40x160 mm prisms were made for compressive tests and three-point bending tests respectively. The moulds with steel fiber fresh mortars were vibrated on a vibrating table for 3 seconds. The specimens were covered with a plastic sheet, demoulded after 24 hours and cured in water at 20 degrees Celsius for 28 days. Table 4 shows the average compressive strength of six cubes compressed at a rate of 0.2 mms^{-1}, and the average flexural strength of three prisms bended at a rate of 0.1 mms^{-1} with the span of 100 mm.

2.6 Scanning electron microscopy

Zeiss Ultra 55 Field Emission Scanning Electron Microscopy (FESEM), with an accelerating voltage of 3 to 5 kV and a working distance of 4 to 6 mm, was adopted to take the SE images of cement powders, limestone powders, aggregate particles with sizes smaller than 0.125 mm, silica fume and steel fiber, as shown in Fig. 4. Cement powders, limestone powders and fine aggregate are granular while silica fume is spherical. Steel fiber has a very smooth surface texture at a magnification of 300x although it shows pores with irregular shapes and line cracks at a magnification of 3000x.

Table 4 – Yield stress, plastic viscosity, slump, slump flow, air-void content, density,compressive and bending strength of mortars with w/b 0.3 and 0.5

	w/b = 0.3					w/b = 0.5			
	A			B		C		D	
	Mix 1	Mix 2	Mix 3	Mix 4	Mix 5	Mix 6	Mix 7	Mix 8	Mix 9
silica fume (% by cement weight)	0			10		0		10	
steel fiber (vol%)	0	0.3	1	0	0.3	0	0.3	0	0.3
yield stress, τ_0 (Pa)	8	11	-	30	42	8	7	10	10
plastic viscosity, μ (Pas)	30.2	43	-	14.5	15.8	6.5	5.7	2.8	5.1
slump (mm)	101	94	60	105	95	100	98	110	103
slump flow (mm)	252.5	192.5	114.5	232.5	202.5	265	260	237.5	245
	air-void content (vol%)								
mix design (excel)	2	2	2	2	2	2	2	2	2
fresh(pressure)	1.9	2.3	3.2	4	2.9	3.4	4	2.5	1.5
$\lambda_{fresh(pressure)}$	6.3	6.0	6.3	7.0	6.3	6.7	7.1	7.5	5.6
λ_{24h}	4	4.7	4.4	5	5.5	3.1	3.4	4.8	3.5
λ_{28d}	3.4	3.7	3.8	4.1	4.7	2.5	2.6	3.9	2.7
	density (kg/m^3)								
mix design (excel)	2409	2425	2460	2396	2411	2320	2335	2311	2326
ρ_{theory}	2458	2475	2510	2445	2460	2367	2383	2358	2374
fresh(pressure)	2302	2326	2351	2273	2304	2208	2215	2181	2242
ρ_{24h}	2359	2358	2399	2323	2324	2293	2302	2248	2291
ρ_{28d}	2375	2382	2416	2345	2345	2309	2320	2265	2308
	strength at 28 days (MPa)								
compressive	75.5	68.9	78	78.6	74.9	39.8	34.9	42.6	46.7
bending	8.9	9.8	11.3	9	9.1	7.1	6.8	7.2	7.2

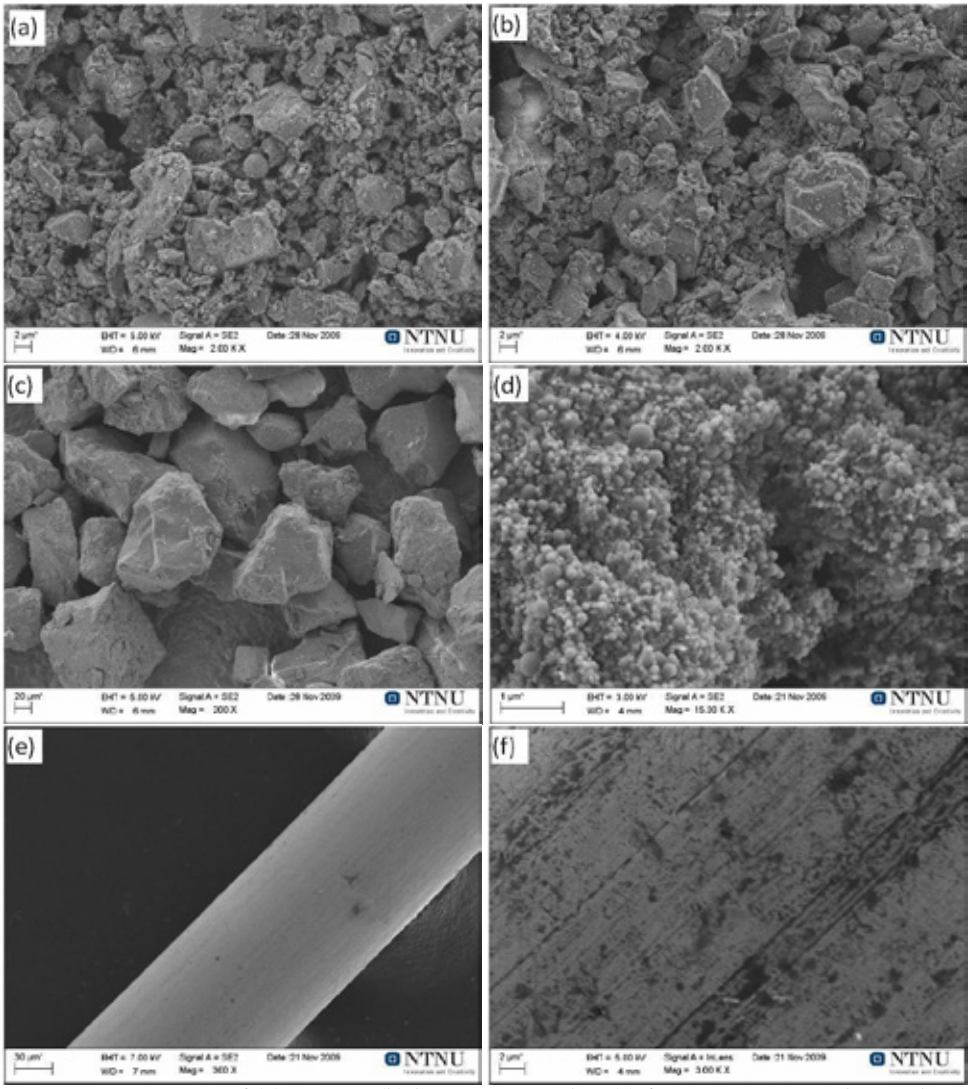

Figure 4 – SE image of (a) cement, (b) limestone powder, (c) fine aggregates with sizes less than 0.125 mm, (d) silica fume, (e) steel fiber and (f) surface texture of steel fiber at a 3000x magnification.

3 Results and Discussion

3.1 Mix Design

In our mix design using the excel-worksheet based proportioning tool [7], the ’matrix’ in Table 1 has the same meaning as powder used in the EFNARC guidelines, except ’matrix’ including water content. Therefore, ’matrix’ is the sum of the amount of cement, silica fume, limestone

powder, water and aggregate particles with sizes smaller than 0.125 mm, see calculation in Appendix. Taking the matrix of 41 vol% into consideration, we managed to design flowable plain mortars with the slump flow and the compressive strength of 230 to 255 mm and 72.5 to 78.6 MPa respectively for w/b 0.3; of 237 to 265 mm and 39.8 to 42.6 MPa respectively for w/b 0.5, see Mix 1, Mix 4, Mix 6 and Mix 8 in Table 4. The slump flows of the flowable plain mortars designed in our study were similar to the slump flow of 239 to 262 mm for self-compacting mortar reported elsewhere [13,23].

The purpose of adding limestone powder in the mortar was to increase the percent of fine powder in order to increase resistance against segregation in fresh mortar. Limestone powder itself did not involve completely in the chemical reaction in the mixture, confirmed both from thermal analysis and BSE image analysis [24]. However, its presence accelerated the initial hydration reaction, influenced the hydrate assemblage [25], and contributed to higher shrinkage and creep deformations [26]. Therefore, the amount of limestone powder used in each mix was kept the same, see Table 1.

It was reported that different types of superplasticizer used together with silica fume had different effect on plastic viscosity, for example, polyacrylate grafted with polymer (PA) used together with silica fume decreased the plastic viscosity, while sodium naphthalene sulphonate-formaldehyde condensate (SNF) used together with silica fume increased the plastic viscosity [19]. Faroug et al. [27] showed that the effect of increasing dosages of superplasticizer on the rheological parameters became minimal for w/b > 0.5, and segregation might occur if the unnecessary amount was added. Szwabowski et al. [20] showed that poly-carboxylate based superplasticizer increased the air-void content at high w/b. Since the same type of superplasticizer as Szwabowski et al. [20] was adopted in our study, less amount of the superplasticizer was used in w/b 0.5 to minimize any increase of air-void content caused by the superplasticizer.

3.2 Density

Fig. 5 shows the densities of 9 mixes at three different stages: fresh, 24-hour and 28-day. The densities of all mixes increased abruptly after 24-hour curing and continued to increase until 28-day curing. We ascribed the increased density from 0 (fresh mortar) to 1 day (demoulding) to the loss of some air-void content after the compaction of fresh mortar in the steel moulds on the vibrating table. This was supported by the calculation of air-void content, λ, for three different stages of mortar, using Eq. 2 which was mainly based on the measured density, see Table 4. The water curing was used in our study. The increased density from 1 to 28 days was due to the absorption of water because of chemical shrinkage when the hydration progressed. The chemical shrinkage is usually ascribed to the volume reduction of the chemically bound water that causes water from the surrounding to be sucked in. In general, low w/b and the use of silica fume are known to increase the chemical shrinkage [28, 29].

Fig. 5 also shows that w/b, silica fume and steel fiber influence the density of the mortar. Mortars with w/b 0.5 had less density than those with w/b 0.3. This was mainly due to the fact that mortars with w/b 0.5 had more water and less cement content. Thus the matrix had more pores and less particle packing than mortars with w/b 0.3, as shown in Fig. 6. Silica fume had lower density than cement powder could explain the fact that plain mortars with silica fume had lower density than those without silica fume. The inclusion of steel fiber increased the density of mortars as expected.

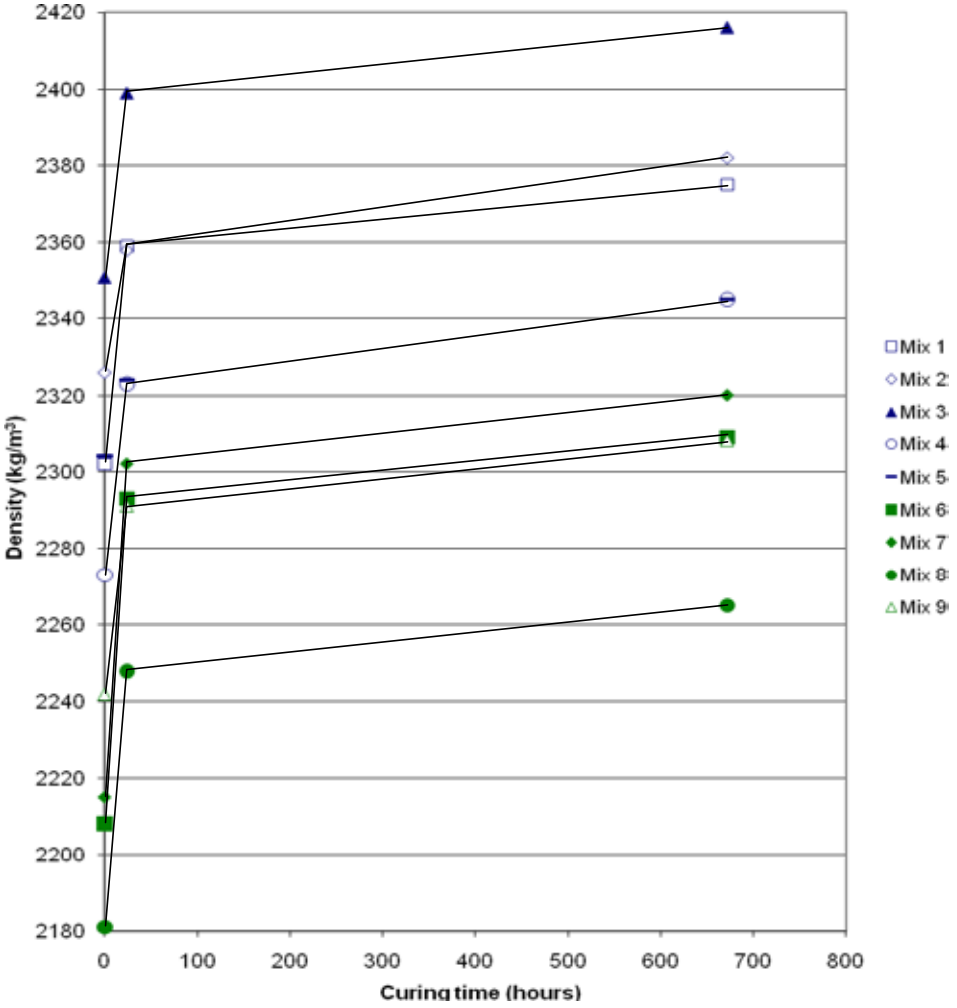

Figure 5 – Density of fresh, 24-hour and 28-day mortar for w/b 0.3 and 0.5.

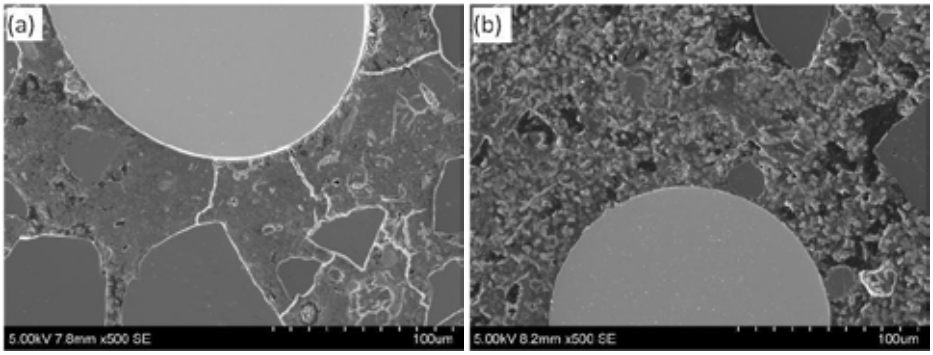

Figure 6 – SE image of the matrix surrounding a steel fiber in (a) w/b 0.3 and (b) w/b 0.5.

3.3 Workability

The workability of the mortar was investigated by studying the slump, yield stress and plastic viscosity. The cohesiveness of the mortar was measured in percent by taking the ratio of the slump difference between mortar with and without silica fume to the slump of mortar without silica fume. Comparing Fig. 7(a) and Fig. 8(a) for w/b 0.3 and comparing Fig. 9(a) and Fig. 10(a) for w/b 0.5, a small bump in the middle of the fresh plain mortars disappeared with the incorporation of 10% silica fume, showing an improvement of the cohesiveness of mortars by 4% for plain mortars with w/b 0.3 and by 10% for plain mortars with w/b 0.5. However, more superplasticizer was required to maintain the slump flow of mortar with silica fume close to that without silica fume, see Table 1 and Table 4. Although superplasticizer may have an effect in decreasing the yield stress, Table 4 shows that 10% silica fume had greater effect in increasing the yield stress than the additional amount of superplasticizer in decreasing the yield stress at w/b 0.3. However, at w/b 0.5, the effect of silica fume on rheological properties became smaller. The increasing amount of water in w/b 0.5 possibly reduced the effect of silica fume on the properties of mortars. Although 10% silica fume increased the yield stress, it decreased the plastic viscosity of mortars, as seen by comparing Mix 1 and Mix 4 for w/b 0.3 and Mix 6 and Mix 8 for w/b 0.5 in Table 4. This is in line with Faroug et al. [27] who reported that the replacement of cement by condensed silica fume up to 20% increased the yield stress, up to 15% replacement decreased the plastic viscosity, and the similar trends of yield stress and plastic viscosity were shown when the dosage of superplasticizer (naphthalene formaldehyde) up to 2% by cement weight were introduced. It was reported that the pozzolanic reaction between silica fume and calcium hydroxide (CH) happened after 1-day or 7-day curing, depending on the amount of cement powder being replaced by silica fume [30]. Fig. 4 shows that silica fume is spherical compared to cement powder. The rheological parameters were taken straight after mixing. It may be suggested that the increase in yield stress, the decrease in plastic viscosity and the increase of the cohesiveness of fresh mortar was related to the spherical shape of silica fume that served as lubricant or roller-bearing before the pozzolanic reaction took place.

From Table 1, the included vol% of steel fibers actually replaced the same vol% of removed aggregates with the amount of the rest of the components remaining unchanged in the mix proportion. Visual comparision of Fig. 7(b) and Fig. 8(b) revealed that the inclusion of 0.3 vol% steel fibers reduced the flowability of mortars w/b 0.3 without silica fume more than that with silica fume. However, the effect of 0.3 vol% steel fibers on mortars with w/b 0.5 with and without silica fume was similar, with a bump in the middle of the fresh mortar showing low cohesiveness, comparing Fig. 9 and Fig. 10. For fresh mortars without silica fume with 0.3 and 1 vol% steel fibers, a halo was partly seen on the edges of the slump revealing segregation and 1 vol% steel fibers tremendeously reduced the workability of fresh mortars, see Fig. 7 (b) and (c). The cylindrical shape of steel fiber caused the entanglement of steel fiber during flowing, and this could explain that after the slump, steel fibers accumulated more in the middle of fresh mortar than spreading out with the flow. With the amount of superplasticizer and silica fume maintained the same in each group, the inclusion of steel fiber increased the yield stress and plastic viscosity of fresh mortar, in agreement with Szwabowski et al. [31]. However, the effect of steel fiber on workability was more significant at w/b 0.3 than at 0.5. Close examination using the FE-SEM revealed that the surface of steel fiber was smooth, see Fig.4. Therefore, the friction between steel fiber and aggregate was minima during flowing. The increase in yield stress and plastic viscosity was mainly caused by the cylindrical shape of steel fiber in causing entanglement during flowing. Fig. 11 shows that no correlation is observed between air void content and rheological properties of fresh mortars.

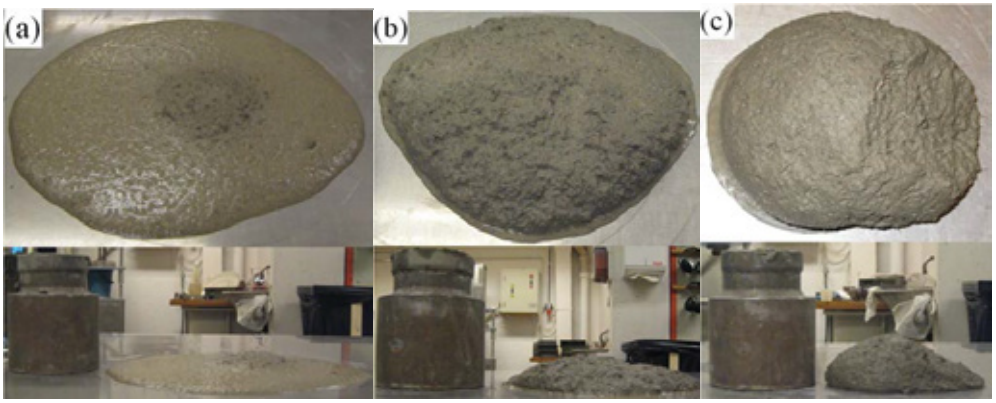

Figure 7 – (Group A) Mortars with w/b 0.3, 0% as-received silica fume, (a) 0, (b) 0.3, and (c) 1 vol% steel fiber after slump from 45° angle for the top and from the side for the bottom photo.

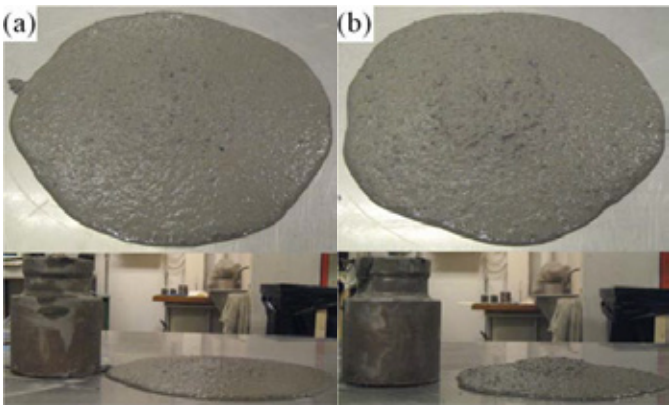

Figure 8 – (Group B) Mortars with w/b 0.3, 10% as-received silica fume, (a) 0, and (b) 0.3 vol% steel fiber after slump from 45° angle for the top and from the side for the bottom photo.

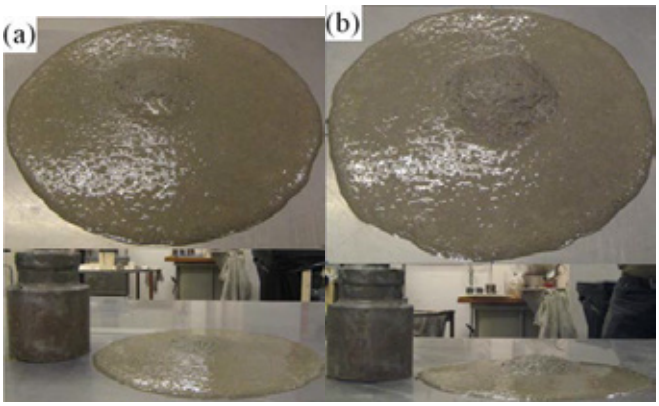

Figure 9 – (Group C) Mortars with w/b 0.5, 0% as-received silica fume, (a) 0, and (b) 0.3 vol% steel fiber after slump from 45° angle for the top and from the side for the bottom photo.

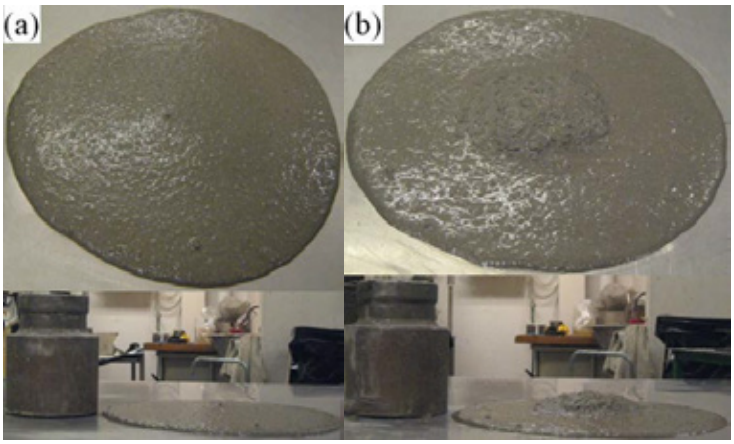

Figure 10 – (Group D) Mortars with w/b 0.5, 10% as-received silica fume, (a) 0, and (b) 0.3 vol% steel fiber after slump from 45° angle for the top and from the side for the bottom photo.

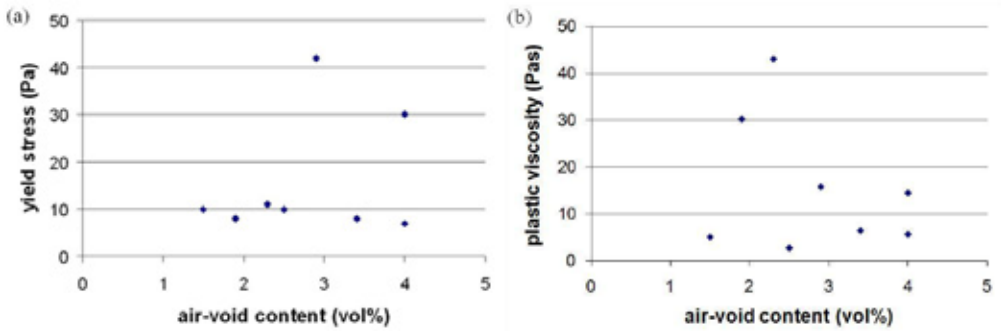

Figure 11 – (a) Yield stress versus air-void content, and (b) Plastic viscosity versus air-void content, of mortars from w/b 0.3 to 0.5.

3.4 Compressive and flexural strength

Silica fume is known to enhance the compressive strength of mortar and concrete [32]. Table 4 shows that for both w/b 0.3 and 0.5, 10% silica fume increased the 28-day compressive strength of plain mortars. However, its effect on increasing the 28-day flexural strength was not significant. Its effect on compressive strength became less strong at w/b 0.5 than at w/b 0.3 due to the increasing amount of water and less binder at w/b 0.5, although Huang et al. [30] reported that the effect of silica fume on increasing the strength was almost insignificant at w/b 0.6.

Table 4 also shows that the inclusion of 0.3 vol% steel fibers into mortars for both w/b did not increase the compressive strength in all mixes studied. Some researchers reported a positive effect on compressive strength for the inclusion of 0.5 vol% or more steel fiber [33,34], but not all of them. The inclusion of steel fibers increased the flexural strength at w/b 0.3, but not at w/b 0.5. In another study using the same mortars, the main effect of fibers on mechanical properties were mainly on ductility and fracture energy, where the incorporation of steel fiber imposed a

great effect on increasing the ductility of mortars after maximum load ($P_{max\text{-}elastic}$) in bending tests, preventing mortars from breaking into two separate parts instantly, and increasing the work ($W_{post\text{-}elastic}$) needed for fracture in Ref. [21]. The inclusion of 1 vol% steel fiber increased both the compressive and the bending strength in our study.

3.5 Effect of air-void content on strength

Table 4 shows that silica fume and steel fiber have an effect in increasing the air-void content in 24-hour and 28-day mortars for both w/b. Balaguru et al. [36] reported that the inclusion of steel fiber reduced the air-void content. This was contrary to many of our observations of increased air-void content due to steel fiber. They argued that the reduction of air-void content was due to the possibility of the randomly distributed fibers providing a path for bubbles to escape. We believed that stirring the fresh mortar in order to disperse the steel fiber evenly during mixing could introduce air into mortar and this was unavoidable.

Although 10% silica fume and 0.3 vol% steel fiber increased slightly the air-void content, no clear trend between the relationship of 28-day compressive and flexural strength with the air-void content was shown in Fig. 12. In fact, mortars with lower compressive and flexural strengths were found at the region of air-void content between 2.5 and 3 vol% (the region where mortars with w/b 0.5 dominated), and mortars with higher compressive and flexural strengths were found at the region of air-void content between 3.5 and 4 vol% (the region where mortars with w/b 0.3 dominated). In fact, the change of the w/b was the key influencing factor on the strengths.

4 Conclusions

1) 10% silica fume improved the cohesiveness of fresh plain mortars by 4% for mortars with w/b 0.3 and by 10% for mortars with w/b 0.5. However, the fresh mortars required more superplasticizer to maintain the slump flow closed to that without silica fume for two different w/b. The effect of silica fume in increasing the yield stress was greater than that of additional amount of superplasticizer in decreasing the yield stress. It increased 28-day compressive strength but gave no significant increase on 28-day flexural strength of mortar for both w/b either with or without steel fiber.

2) The inclusion of 0.3 vol% steel fiber reduced greatly the flowability of fresh mortars with w/b 0.3 without silica fume, but only slightly for those with silica fume. Its effect on the flowability of fresh mortars with w/b 0.5 either with or without silica fume was the same. It did not give a consistent positive effect on compressive strength of mortar for both w/b. It gave a slight increase in 28-day flexural strength for mortars with w/b 0.3, but not with w/b 0.5.

3) 10% silica fume and 0.3 vol% steel fiber increased slightly the air-void content in mortar. However, the slight increase in the air-void content did not influence the strength of the mortar.

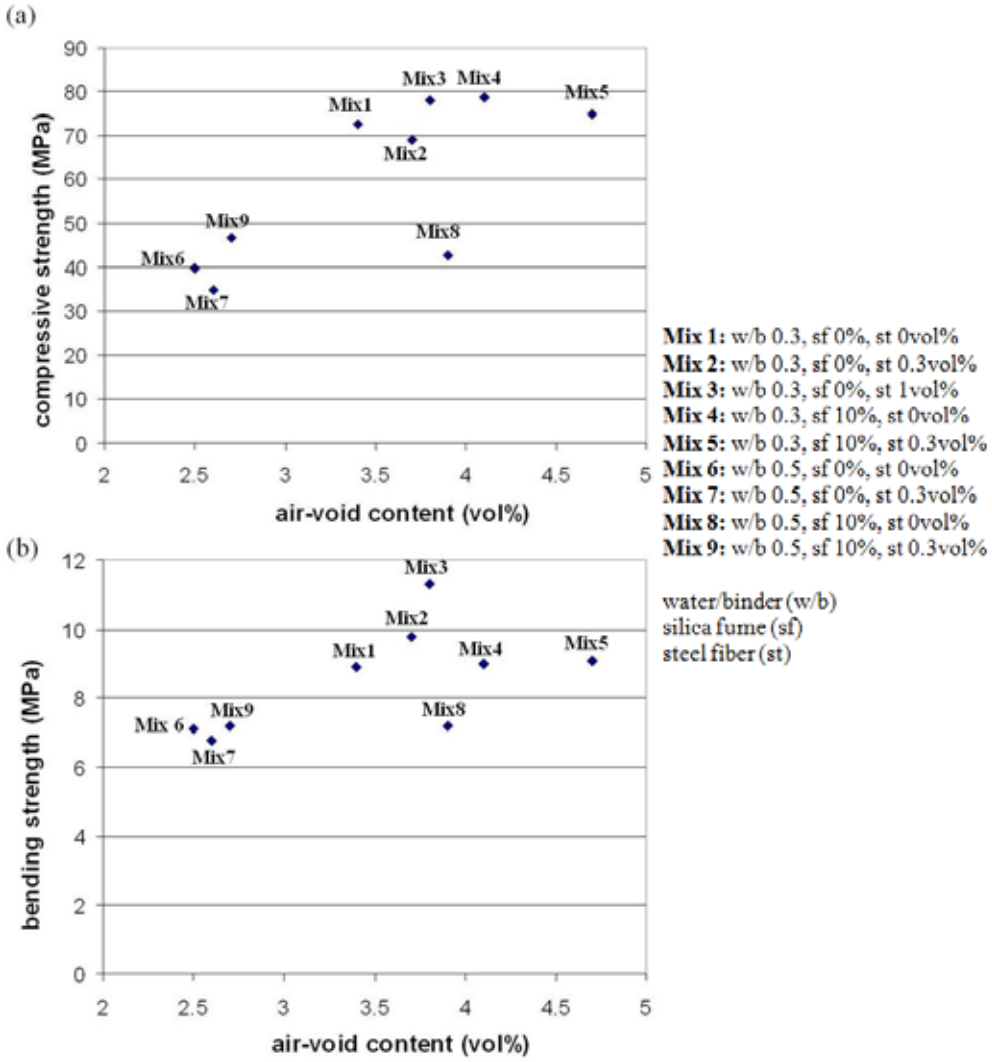

Figure 12 – (a) 28-day compressive strength versus 28-day air-void content, and (b) 28-day bending strength versus 28-day air-void content, of mortars from w/b 0.3 to 0.5.

Acknowledgments

We thank the funding from the Norwegian University of Science and Technology (NTNU) and the Norwegian Research Council (NRC) through the Institution-based Strategic Project (ISP) on focus area 3 -Sustainable Infrastructure (Grant No 177275). This work also forms a part of NTNU's contribution to the Concrete Innovation Centre (COIN) at Sintef/NTNU, starting in 2007 as a centre for research based innovation (CRI) within concrete technology with 9 industrial partners: Aker Solutions, Norcem Heidelberg, Borregaard, Maxit, Skanska, Rescon Mapei, UNICON, Veidekke and the Norwegain Road directory. The authors would like to thank PhD stipendiat Sindre Sandbakk and engineer Ove Loraas for their discussions on mix proportion.

APPENDIX

How to calculate matrix volume in mix proportion Matrix is sum of the amount of cement, silica fume, filler, water and aggregate particles with sizes smaller than 0.125 mm.

Refer to Mix 9

1) Density of cement = 3120 kg/m^3
Cement = 368.2 kg in 1 m^3
Volume of cement = 368.2/3120 = 0.118 m^3

2) Density of silica fume = 2200 kg/m^3
Limestone = 36.8 kg in 1 m^3
Volume of limestone = 36.8/2200 = 0.0167 m^3

3) Density of limestone = 2700 kg/m^3
Limestone = 47.9 kg in 1 m^3
Volume of limestone = 47.9/2700 = 0.0177 m^3

4) Density of water = 1000 kg/m^3
Water = 202.5 kg in 1 m^3
Volume of water = 202.5/1000 = 0.2025 m^3

5) Density of superplasticizer = 1030 kg/m^3
Superplasticizer = 6.4 kg in 1 m^3
15% dry stuff in 6.4 kg superplasticiser = 0.96 kg
Volume of dry stuff in superplasticizer = 0.96/1030 = 0.00093 m^3

6) Density of sand 0-4mm = 2650 kg/m^3
Percent of particles < 0.125 mm = 6.1%
Sand 0-4 mm used = 1399.4 kg in 1 m^3
Particles < 0.125 mm = 6.1/100 × 1399.4 = 85.36 kg/m^3
Volume of particles < 0.125 mm = 85.36/2650 = 0.032 m^3

7) Density of sand 0-2 mm = 2650 kg/m^3
Percent of particles < 0.125 mm = 23.6%
Sand 0-2 mm used = 246.9 kg in 1 m^3
Particles < 0.125 mm = 23.6/100 × 246.9 = 58.27 kg/m^3
Volume of particles < 0.125 mm = 58.27/2650 = 0.022 m^3

Total of matrix = 0.118 + 0.0167 + 0.0177 + 0.2025 + 0.00093 + 0.032 + 0.022 = 0.40983 ≈ 0.41 m^3

REFERENCES

1. Felekoğlu, B., Türkel, S., Altuntaş, Y., "Effects of steel fiber reinforcement on surface wear resistance of self-compacting repair mortars", *Cement and Concrete Composites*, Vol. 29, 2007, pp. 391-396.
2. Ferrara, L., Park, Y-D., Shah, S.P., "A method for mix-design of fiber-reinforced self-compacting concrete", *Cement and Concrete Research*, Vol. 37, 2007, pp. 957-971.
3. BIBM, CEMBUREAU, EFCA, EFNARC, and ERMCO, "The European Guidelines for Self-Compacting Concrete - Specification, Production and Use", *available from www.efnarc.org*, May 2005.
4. Saak, A.W., Jennings, H.M., Shah, S.P., "New Methodology for Designing Self-compacting Concrete", *ACI Materials Journal*, Vol. 98, No. 6, 2001, pp. 429-439.
5. Domone, P.L., "Self-compacting concrete: An analysis of 11 years of case studies", *Cement and Concrete Research*, Vol. 28, 2006, pp. 197-208.
6. Okamura, H., Ozawa, K., "Mix design for self-compacting concrete", *Concrete Library of JSCE* no. 25, 1995, pp. 107-120.
7. Smeplass, S., "Chapter 4 – Fresh concrete - Proportioning", TKT 4215 Concrete Technology 1, Department of Structural Engineering, Norwegian University of Science and Technology (NTNU), Norway, August 2004, 38pp.
8. Smeplass, S., Mørtsell, E., "The applicability of the particle matrix model to self compacting concrete (SCC)", *Nordic Concrete Research* no. 26-6, 2001, 13p.
9. Tattersall, G.H., "The rationale of a two-point workability test", *Magazine of Concrete Research*, Vol. 25, No84, 1973, pp. 169-172.
10. Petit, J-Y., Wirquin, E., Vanhove, Y., Khayat, K., "Yield stress and viscosity equations for mortars and self-consolidating concrete", *Cement and Concrete Research*, Vol. 37, 2007, pp. 655-670.
11. Schwartzentruber, L.A., Roy, R.L., Cordin, J., "Rheological behaviour of fresh cement pastes formulated from a self compacting concrete (SCC)", *Cement and Concrete Research*, Vol. 36, 2006, pp. 1203-1213.
12. Nielsson, I., Wallevik, O.H., "Rheological evaluation of some empirical test methods - preliminary results", Proceedings, 3rd international RILEM Symposium on Self-Compacting Concrete, edited by Wallevik, O. and Nielsson, I., (RILEM Publications SARL), Reykjavik, Iceland, August 2003, pp. 59-68.
13. Güneyisi, E., Gesoğlu, M., "Properties of self-compacting blends of fly ash and metakaolin", *Materials and Structures*, Vol. 41, 2008, pp. 1519-1531.
14. Lachemi, M., Hossain, K.M.A., Lambros, V., Nikinamubanzi, P-C., Bouzoubaâ, N., "Performance of new viscosity modifying admixtures in enhancing the rheological properties of cement paste", *Cement and Concrete Research*, Vol. 34, 2004, pp. 185-193.
15. Khayat, K.H., "Viscosity-enhancing admixtures for cement-based materials - an overview", *Cement and Concrete Composites*, Vol. 20, 1998, pp. 171-188.
16. Lachemi, M., Hossain, K.M.A., Lambros, V., Bouzoubaâ, N., "Development of cost-effective self-consolidating concrete incorporating fly ash, slag cement, or viscosity-modifying admixtures", *ACI Materials Journal*, Vol. 100, No. 5, 2003, pp. 419-425.
17. Tayyeb, A., Memon, S.A., Obaid, H., "Production of low cost self compacting concrete using bagasse ash", *Construction and Building Materials*, Vol. 23, 2009, pp. 703-712.
18. Leemann, A., Winnefeld, F., "The effect of viscosity modifying agents on mortar and concrete", *Cement and Concrete Composites*, Vol. 29, 2007, pp. 341-349.
19. Vikan, H., Justnes, H., "Rheology of cementitious paste with silica fume or limestone", *Cement and Concrete Research*, Vol. 37, 2007, pp. 1512-1517.

20. Szwabowski, J., Piekarczyk, B.Ł., "The increase of air content in SCC mixes under the influence of carboxylate superplasticizer", *Cement Wapno Beton*, Vol. 13, 2008, pp. 205-215.
21. Phatak, T.C., Agarwal, S.K., Masood, I., "The effect of a superplasticizer (from cashew nut shell liquid) on the properties of concrete and mortar", *Materials and Structures*, Vol. 25, 1992, pp. 355-357.
22. Wallevik, J.E., "Rheology of Particle Suspensions", PhD thesis, Department of Structural Engineering, Norwegian University of Science and Technology (NTNU), Norway, 2003.
23. Güneyisi, E., Gesoğlu, M., Ozbay, E., "Effects of marble powder and slag on the properties of self compacting mortars", *Materials and Structures*, Vol. 42, 2009, pp. 813-826.
24. Ye, G., Liu, X., Schutter, G.D., Poppe, A.-M. Taerwe, L., "Influence of limestone powder used as filler in SCC on hydration and microstructure of cement pastes", *Cement and Concrete Composites*, Vol. 29, 2007, pp. 94-102.
25. Lothenbach, B., Saout, G.L., Gallucci, E., Scrivener, K., "Influence of limestone on the hydration of portland cement", *Cement and Concrete Research*, Vol. 38, 2008, pp. 848-860.
26. Heirman, G., Vandewalle, L., Gemert, D.V., Boel, V., Audenaert, K., Schutter, G.D., Desmet, B., Vantomme, J., "Time-dependent deformations of limestone powder type self-compacting concrete", *Engineering Structures*, Vol. 30, 2008, pp. 2945-2956.
27. Farong, F., Szwabowski, J., Wild, S., "Influence of superplasticizers on workability of concrete", *Journal of Materials in Civil Engineering*, Vol. 11, 1999, pp. 151-157.
28. Loukili, A., Khelidj, A., Richard. P., "Hydration kinetics, change of relative humidity, and autogenous shrinkage of ultra-high-strength concrete", *Cement and Concrete Research*, Vol. 29, 1999, pp. 577-584.
29. Sellevold, E.J., Justnes, H., "High-strength concrete binders Part B: Nonevaporable water, self-dessication and porosity of cement pastes with and without silica fume", In: 4th CANMET/ACI International Conference on Fly Ash, Silica Fume, Slag and Natural Pozzolans in Concrete, ACI SP 132-48, Istanbul, Turkey, May 1992, pp. 891-902.
30. Huang, C.Y., Feldman, R.F., "Influence of silica fume on the microstructural development in cement mortars", *Cement and Concrete Research*, Vol. 15, 1985, pp. 285–294.
31. Szwabowski, J., Ponikiewski, T., "Influence of steel fibres geometry on chosen profiles of self-compacting concrete", *Cement Wapno Beton*, Vol. 13, 2008, pp. 3-8.
32. Yazici, H., "The effect of silica fume and high-volume Class C fly ash on mechanical properties, chloride penetration and freeze-thaw resistance of self-compacting concrete", *Construction and Building Materials*, Vol. 22, 2008, pp. 456-462.
33. Köksal, F., Altun, F., Yiğit, I., Şahin, Y., "Combined effect of silica fume and steel fiber on the mechanical properties of high strength concretes", *Construction and Building Materials*, Vol. 22, 2008, pp. 1874-1880.
34. Song P.S., Hwang, S., "Mechanical properties of high-strength steel fiber -reinforced concrete", *Construction and Building Materials*, Vol. 18, 2004, pp. 669-672.
35. Wang, X.H., Jacobsen, S., Lee, S.F., He, J.Y., Zhang, Z.L., "Effect of silica fume, steel fiber and ITZ on the strength and fracture behavior of mortar", *Materials and Structures*, Vol. 43, 2010, pp. 125-139.
36. Balaguru, P., Ramakrishnan, V., "Properties of fiber reinforced concrete: workability, behavior under long-term loading, and air-void characteristics", *ACI Materials Journal*, Vol. 85, No. 3, 1988, pp. 189-196.

Penetration Profiles of Water Repellent Agents in Concrete as a Function of Time – Determined with FTIR-Spectrometer

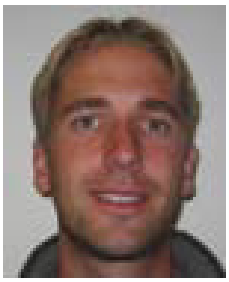

Anders Johansson-Selander
Tekn. Lic, PhD-Student
Swedish Cement & Concrete Research Institute
Drottning Kristinas väg 26, SE-100 44 Stockholm
anders.selander@cbi.se

Mårten Janz
Tekn. Dr
Energoretea
Drottning Kristinas väg 26, SE-100 44 Stockholm
marten.janz@energoretea.se

Johan Silfwerbrand
Tekn. Dr, Professor
Swedish Cement & Concrete Research Institute
Drottning Kristinas väg 26, SE-100 44 Stockholm
Johan.silfwerbrand@cbi.se

Jan Trägårdh
Fil. Lic
Swedish Cement & Concrete Research Institute
Drottning Kristinas väg 26, SE-100 44 Stockholm
jan.tragardh@cbi.se

ABSTRACT

The success of a water repellent treatment on concrete is often judged by the visual penetration depth. This method, however, only indicate if the water repellent agent has penetrated the concrete or not. With the use of a FTIR-spectrometer with KBr-tablets a determination of the concentration of the water repellent agent can be made. This is an important tool in the understanding of how these treatments work. From the results of the experiment presented in this paper it is clear that the duration of contact between a water repellent agent and the concrete is important for the outcome of the treatment. It is clear that the concentration as well as the depth increases with a prolonged time for the treatment.

Key words: silane, water repellent agent, FTIR-spectrometer, penetration profile.

1. INTRODUCTION

Water repellent agents are often used on concrete to prolong the service life of the structure. This is accomplished by protecting the reinforced concrete from chloride ingress and/or by reducing the moisture content inside. The success of a treatment is often judged by the visual penetration depth. This method, however, only indicates if the water repellent agent has penetrated the concrete or not. The FTIR (Fourier Transform InfraRed) -spectrometer gives the possibilty of determining not only the penetration depth but also the concentration of the agent.

Concrete is an inorganic material meaning that there are no carbon-hydrogen bonds. The FTIR-spectra for concrete and organic materials differ in the region for this bond. The alkylgroup of the fully reacted silane can thereby be detected and quantified by the FTIR-spectrometer. This is an important tool in the understanding of how water repellent agents work.

1.1 Water repellent agents

Water repellent agents, today mainly consisting of alkylalkoxysilane, contain an organic group (alkylgroup) when fully reacted. The silane is absorbed through capillary suction into the pores, when applied on the concrete surface. The alkoxy groups react in the alkaline environment of the pore solution and a fine network of polymer siloxane or silicon resin forms [1] (see Figure 1) which turns the concrete from hydrophilic to hydrophobic [2] giving it protection against e.g., chlorides [3]. The alkoxy group is liberated as alcohol during the reaction.

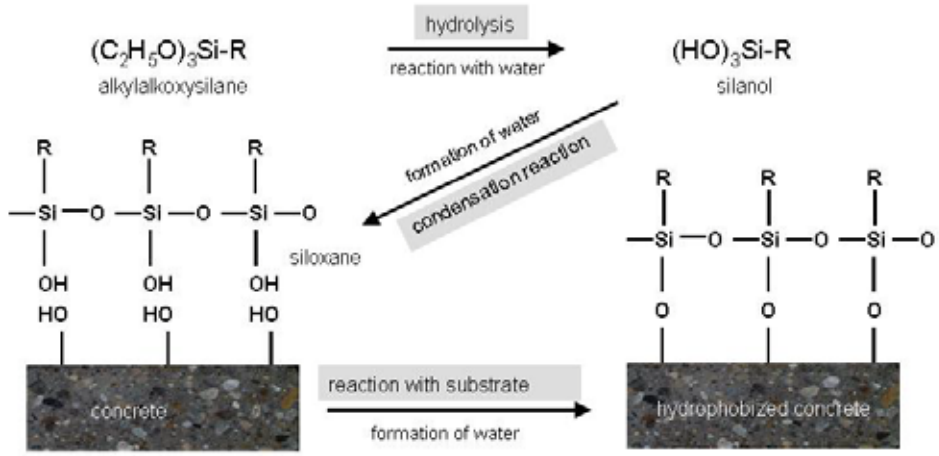

Figure 1: Reaction of an organofunctional trialkoxysilane with the concrete matrix [4]. Ethanol is liberated during the hydrolysis.

Identifying the FTIR spectra of pure polymer siloxane and especially the influence of the organic bond between carbon and hydrogen makes it possible to detect and quantify the amount

of water repellent agent in concrete after a treatment. This method is described in detail by *Gerdes* in [5].

1.2 FTIR-Spectroscopy

FT-IR stands for Fourier Transform InfraRed, where FT refers to the method used to interpret the results. This is the preferred method of infrared spectroscopy. In infrared spectroscopy, IR radiation is passed through a sample. Some of the infrared radiation is absorbed by the sample and some of it is passed through (transmitted). The resulting spectrum represents the molecular absorption and transmission of the sample, creating a molecular fingerprint of the sample [6]. This makes infrared spectroscopy useful for several types of analysis as for example organic materials in concrete.

Molecules are flexible, moving collections of atoms. The atoms in a molecule are constantly oscillating around average positions. Bond lengths and bond angles are continuously changing due to this vibration [6]. A molecule absorbs infrared radiation when the vibration of the atoms in the molecule produces an oscillating electric field with the same frequency as the frequency of incident IR-radiation.

2. METHOD

The samples used in this experiment were originally prepared for an investigation on the effective penetration depth of a water repellent treatment and how different factors influence it [7]. A total of 400 samples were prepared. Ten of these samples were analyzed in this FTIR-measurement. Another ten of identically prepared samples were used to measure the visual penetration depth. This was done according to EN 1504-2:2004 as the distance from the surface to the sharp line between dry and wet concrete after it has been sprayed with water.

2.1 Preparation of samples

Two types of concrete with w/c = 0.8 and 0.45, respectively, were used in this experiment with the composition according to Table 1. The maximum size of the aggregate was 8 mm. The concretes were cast from a CEM I 42.5 BV, LA, SR (Swedish cement for civil engineering structures) according to EN 197-1 in 80 litre boxes and conditioned for three months in 100 % RH and 20°C. Cores with a diameter of 75 mm were then drilled out of the boxes and cut into 30 mm thick plates. The first and last plates from each core were removed from the setup in order to avoid any boundary effects. To ensure a uni-dimensional flow when the samples were treated with the water repellent agent the perimeter of the plate was sealed before they were placed inside the climate boxes, leaving the up- and downside open.

Table 1: The concrete mixtures used in the experiments.

w/c	Cement (kg/m^3)	Aggregate 0-8 mm (kg/m^3)	Water (kg/m^3)	Plasticizer (kg/m^3)
0.45	500	1575	225	2.0 (Glenium)
0.80	350	1609	280	-

The plates were then conditioned for six months in 59 % RH [8]. The humidity was created inside climate boxes with saturated NaBr- solution and small rotators. The bottom of the climate box was filled with $Ca(OH)_2$ - powder to absorb the CO_2 in the air in order to avoid the samples from carbonating. To check the depth of carbonation a few plates were cracked and sprayed with phenolphthalein. No carbonation had taken place, meaning the carbonation depth was less than 0.1 mm.

2.2 Water repellent treatment

A box with triethoxy(isooctyl)silane in liquid form was prepared. A 10 mm thick net was placed in the bottom of the box to ensure that full contact between the fluid and the specimen was achieved. The silane was then poured into the box so that the net was covered to a depth of approximately 5 mm. The concrete plates were then placed on the net so that the bottom was in contact with the fluid. Since the envelope surface of the plate is sealed a uni-dimensional capillary suction is achieved. When the desired time had passed the plates were removed from the box, wiped off with paper and then placed horizontally in open air. The five different times for treatment was 5 minutes, 25 minutes, 2 hours, 10 hours and 48 hours, respectively.

2.3 FTIR-analysis

The FTIR-spectrometer used in the experiment is an instrument which uses potassium-bromide (KBr)-tablets. The preparation of samples is time consuming but the reward is that the instrument, when calibrated, can be used for accurate quantification of a specific molecule or group. Information about the thickness of the tablet and the concentration of powder in the tablet is necessary and assured by accurate preparations of the sample. The contribution to the FTIR-spectra is almost zero from KBr. The following steps are included in the preparation and measurements of one tablet starting from dry solid concrete:

1. Concrete powder is needed for the measurements. A grinding machine (see Figure 2a) is used for this purpose. A solid concrete piece is placed in the machine horizontally and the concrete powder is collected. The machine is cleaned afterwards so that contamination of the next sample is avoided. Depending on the surface area of the sample and the skill of the operator as small as 0.5 mm intervals are possible.

2. The concrete powder is then mixed with KBr-powder at a given concentration and mass with an accuracy of ±1%. 1000 mg KBr is mixed with 40 mg concrete powder. This is important to ensure the concentration and the thickness of the tablet since the quantification depends on this.

3. 250 mg powder mixture is then placed in the 13 mm tablet press (see Figure 2b). KBr melts at high pressure and when the pressure is released a tablet is formed.

4. The tablet can then be placed in a holder (see Figure 2c) which fits in the FTIR-spectrometer (see Figure 2d).

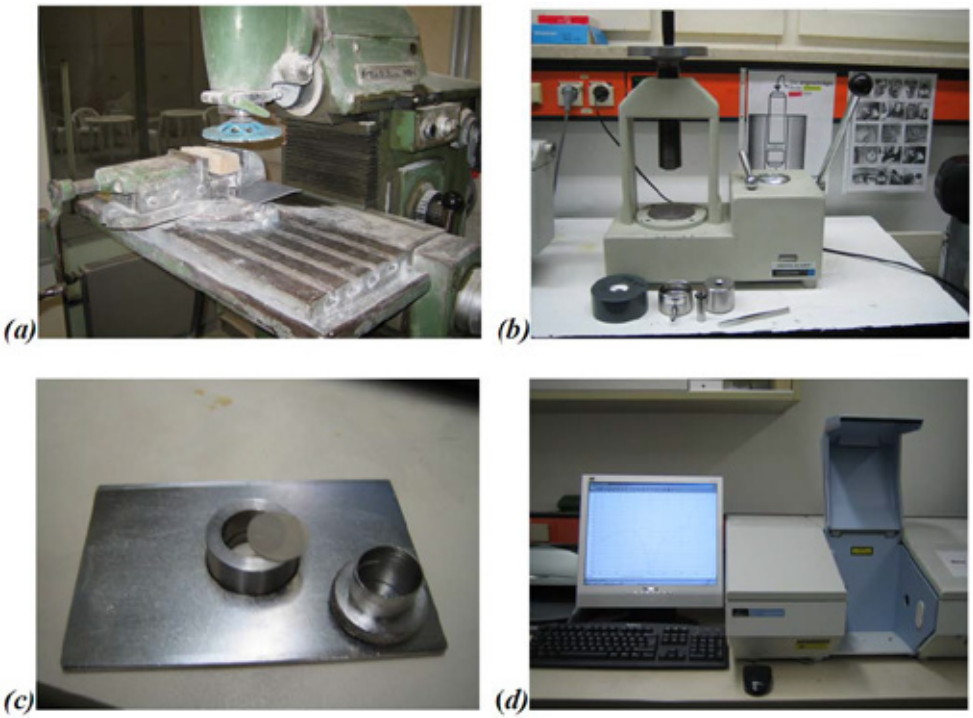

Figure 2: a) The machine used to grind powder from 1 mm layers. b) Equipment used to press KBr-tablets. c) A KBr-tablet and the holder for the tablet. d) FTIR-spectrometer.

The result from the analysis is a spectrum with wave number (wavelength^{-1}) on the x-axis and the absorption (%) on the y-axis resulting from the IR-radiation. In the region of wavenumber 2800-3100 cm^{-1} a difference in the spectrum for concrete and organic material can be noted. The quantification process is based on area calculation. A specific peak (see Figure 3) caused by the water repellent treatment is identified and the area of that peak is related to the amount of the fully reacted water repellent agent present in the concrete. A calibration curve with known concentrations is necessary in this step.

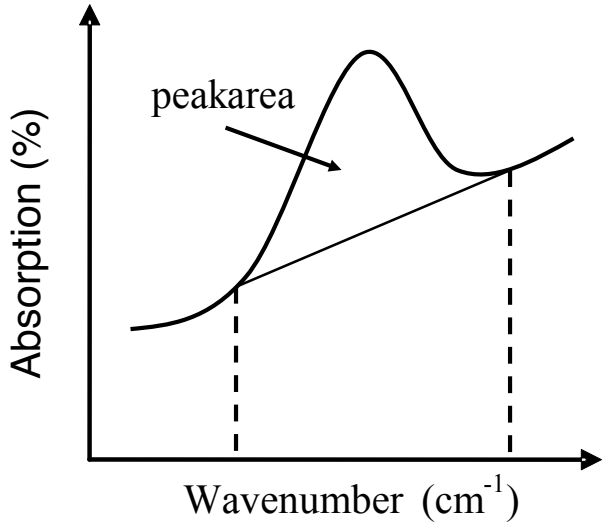

Figure 3: Illustration of the quantification method where the area of a specific peak is related to the amount of fully reacted water repellent agent present in the concrete.

3. RESULTS & DISCUSSION

The penetration profiles and the influence of the duration of contact are presented for two different concrete types with w/c = 0.8 and 0.45. The profiles are shown in Figures 4 and 5. Every curve represents one concrete plate and 1 mm on the x-axis means that the powder analyzed is collected from 0.5-1.5 mm from the surface.

Three well known factors which affect the outcome of a water repellent treatment in terms of penetration depth are time, porosity and degree of saturation [9-11]. The time referred to is the duration of contact between the water repellent agent and the concrete surface. The porosity and degree of saturation refer to the concrete pore system and the amount of moisture inside the concrete at the time of the impregnation, respectively. The effect of time and porosity can be seen clearly in Figures 4 and 5 when the concentration profiles are compared. The higher porosity of the concrete with w/c = 0.8 clearly results in a higher concentration. A longer duration of contact also gives a higher concentration at a given depth with one exception. The penetration profile of the 25 minutes treatment and the two hour treatment in Figure 4 is almost the same. This is probably due to the fact that each penetration profile is based on just one sample.

The highest concentration is reached at the surface for the w/c = 0.45 in Figure 4 while the peak for w/c = 0.8 is shifted a few millimeters from the surface in Figure 5. A certain amount of silanes always evaporates before the polymerization starts which could be one explanation to the peak for the treatments with a longer duration and higher concentrations.

The correlation between the visual penetration depth of the water repellent agent, defined according to EN 1504-2:2004 as the distance from the surface to the sharp line between dry and wet concrete after it has been sprayed with water, and the concentration is clear. The visual

penetration depth of the identically prepared samples corresponds well to the approximate concentration of 1 to 2 mg polysiloxane/g concrete in this experiment. The best correlation is given by 1.5 mg polysiloxane/g concrete. This can be seen in Figure 6. There is, however, a need for more experiments before a fixed concentration can be set for this correlation.

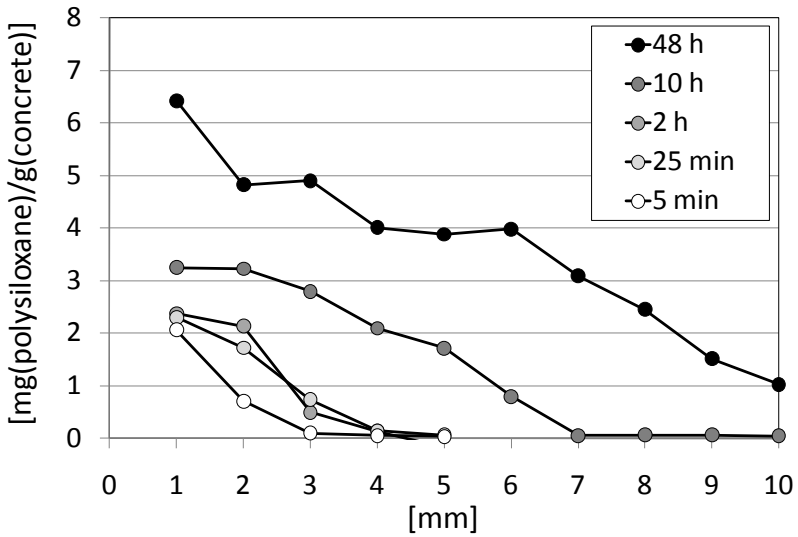

Figure 4: Penetration profiles of triethoxy(isooctyl)silane on concrete with w/c = 0.45 for different durations of treatment. The plates were conditioned in 59 % RH before the treatment. Every point represents one tablet.

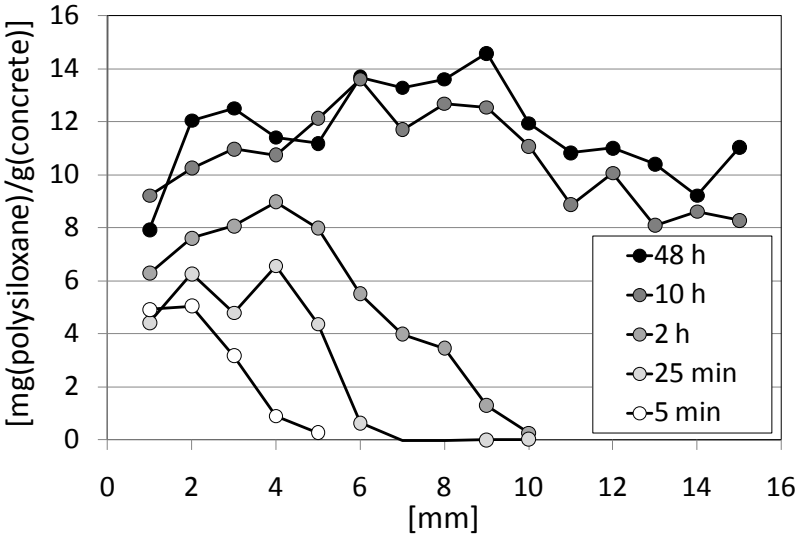

Figure 5: Penetration profiles of triethoxy(isooctyl)silane on concrete with w/c = 0.8 for different durations of treatment. The plates were conditioned in 59 % RH before the treatment. Every point represents one tablet.

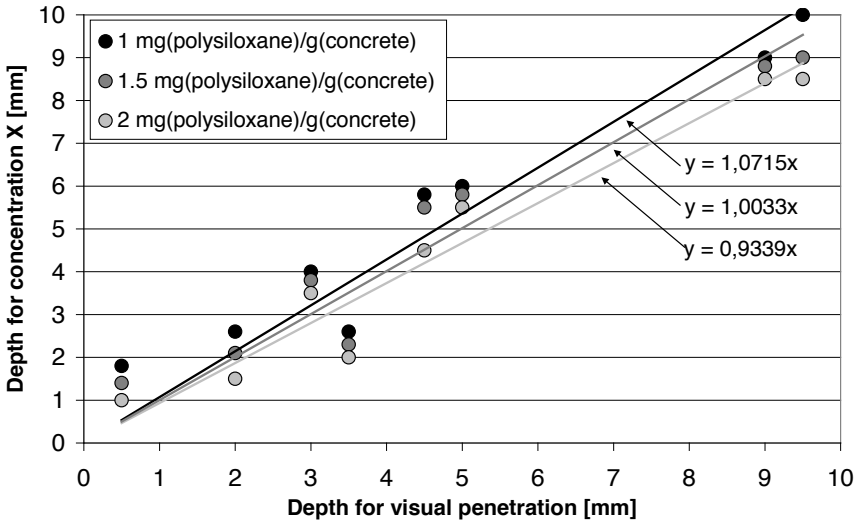

Figure 6: The correlation between the visual penetration depth and a specific concentration measured with FTIR-spectroscopy. The concentration of 1.5 mg polysiloxane/g concrete gives a correlation of 1.0033.

4. CONCLUSIONS

The conclusions are based on an experiment where the penetration profiles of a total of ten water repellent treated samples were determined by the means of FTIR-spectroscopy. The experiment should be considered as a pilot study to evaluate the method and the impact of the duration of the treatment on the penetration profiles.

The duration of contact between the water repellent agent and the concrete is important for the outcome of the treatment. Figures 4 and 5 illustrate how the penetration profiles are affected and it is clear that the concentration as well as the depth increases with a prolonged time for the treatment. The correlation between the visual penetration depth and a given concentration is clear in this experiment. The concentration of 1.5 mg polysiloxane/g concrete gives the best result. This, however, is just a relation between the concentration and the visual depth and the relation might not be the same with the effectiveness of the treatment.

The difference in the concentrations between the different concrete types clearly illustrates how important the factor porosity is for the outcome of the treatment. If conditioned in the same environment and treated in the same way the porosity has a major influence on the depth and concentration of the water repellent agent.

The FTIR-spectrometer with KBr-tablets is the only method today that can be used for quantification of water repellent agents in concrete. This is an important tool in the understanding of how these treatments work. The potential of relating the concentration of water repellent agent to porevolume or cement content in a further development are interesting in

order to learn more. However, the method is laborious and time consuming and this is a disadvantage in comparison with the visual penetration depth.

ACKNOWLEDGMENTS

Financial support from the Swedish Research Council for Environment, Agriculture Sciences and Spatial Planning is gratefully acknowledged. The authors also wish to express gratitude to Prof. Andreas Gerdes, Forschungs-Zentrum Karlsruhe, for theoretical and practical help with the FTIR-Spectrometer.

REFERENCES

1. Gerdes A. H., ”Transport und chemische Reaktion siliciumorganischer Verbindungen in der Betonrandzone.” PhD-Thesis, Eidgenössische Technische Hochschule (ETH), Building Materials Reports No. 15, Zürich, Switzerland, 2001.
2. Kus, H., “Long-Term Performance of Water Repellants on Rendered Autoclaved Aerated Concrete”, PhD-Thesis, Centre for Built Environment, Materials Technology, University of Gävle, ISBN 91-7283-352-1. 2002.
3. Johansson, A., Janz, M., Silfwerbrand, J., & Trägårdh, J., ”Long-term Measurements on Chloride Ingress in a Road Tunnel Environment”. Proceedings, Hydrophobe V, Brussels, Belgium, April 15-16, 2008 pp. 327-328.
4. Giessler, S., Standke B. & Büchler M., “A New Silane System for Corrosion Reduction of Steel Reinforced Concrete”. Proccedings, Hydrophobe IV – 4th International Conference on Water Repellent Treatment of Building Materials, Stockholm, April 12-13, Aedificatio Publishers, 2005, pp 17-26.
5. Gerdes A. H., Betschart S. &Wittmann F. H. “Quality Control by FT-IR-Spectroscopy”, Proceedings, Hydrophobe II- Second International Conference on Water Repellent Treatment of Building Materials, Zürich, September 10-11, Aedificatio Publishers, 1998, pp. 237-244.
6. Coates, J. “Interpretation of Infrared Spectra, A Practical Approach”, Encyclopaedia of of Analytical Chemistry, R. A. Meyers (Ed.) John Wiley & Sons Ltd, Chichester, 2000, pp. 10815-10837.
7. Johansson, A., Janz, M., Silfwerbrand, J., & Trägårdh, J., ”Penetration Depth for Water repellent Agents in Concrete as a Function of Humidity, Porosity and Time”, Int. J. Restoration of Buildings and Monuments, Vol. 13, No. 1, 2007, pp. 3-16.
8. D. R. Lide, Editor, Constant Humidity Solutions, Handbook of Chemistry and Physics, 74th Edition, CRC-Press, Boca Raton, Florida, USA, 1994, 15-25.
9. Meier. S.J. & Wittmann. F.H., “Influence of Concrete Quality, its age and Moisture Content, on the Penetration Dept of Water Repellent Agents”, Proceedings, Hydrophobe III- Third International Conference on Water Repellent Treatment of Building Materials, Aedificatio Publishers, 2001, pp. 123- 131.
10. Krii. S, ”Hydrophobic Impregnation - Penetration Depth in Brick, Limestone and Mortar”, (Vattenavvisande impre-genering - inträngningsdjup i tegelsten, kalksandsten och morbruk). Master Thesis TVBM-5031, Lund University of Technology. 1996, (In Swedish)

11. Bofeldt. M. & Nyman. B.. “Penetration Depth of Hydrophobic Impregnating Agents for Concrete”, Proceedings, Hydrophobe III- Third International Conference on Water Repellent Treatment of Building Materials, Aedificatio Publishers, 2001, pp. 133-141.

Measurement methods for stored VOC in concrete floors

Anders Sjöberg
Ph.D. Assistant Professor
Division of Building Materials, Lund University
P.O Box 118, 221 00 Lund
anders.sjoberg@byggtek.lth.se

Patrice Blondeau
Ph.D. Associate Professor
LEPTAB, University of La Rochelle
La Rochelle, France
pblondea@univ-lr.fr

Peter Johansson
Ph.D. Assistant Professor
Division of Building Materials, Lund University
P.O Box 118, 221 00 Lund
peter.johansson@byggtek.lth.se

ABSTRACT

Two methods used to determine stored VOC (volatile organic compounds) in concrete slabs has been compared. These methods are frequently used in investigating indoor environment problems where emissions from moisture damaged floorings are suspected.

Comparative measurements were made in situ, and the results show good agreement with expected values, especially in measurements of a profile at several levels in the concrete floor, or at several different places in one and the same damaged floor.

The comparative measurements have been used in evaluating the partition coefficient (K) and the diffusion coefficient (D, δ) for n-butanol and 2-ethyl-1-hexanol in concrete.

Key words: VOC, measurement methods, stored degradation products, partition coefficient (K), diffusion coefficient (D, δ)

1. INTRODUCTION

A common outcome in investigations of indoor environment problems in Scandinavia is that structures with damp concrete floors may be a considerable source of VOC to the indoor air.

Two of the methods frequently used among investigators are examined and compared in this paper.

The deterioration of flooring materials is well known as a plausible cause of indoor air problem. Emissions from floor constructions may contribute considerable quantities of volatile organic compounds (VOC) to the indoor air, Gustavsson and Lundgren /1/, Wiglusz et al /2/, Cox et al /3/, Saarela et al /4/, Sjöberg /5,6/, Wilke et al /7/. For example, building materials of polyvinyl chloride (PVC) are known to degrade in damp alkaline conditions and the degradation products have been related to upper respiratory symptoms and signs of inflammation, Wieslander G, et al /8/ and to asthma symptoms, Norbäck et al, /9/, Bornehag et al, /10/.

According to Sjöberg /6, 11/, the moist alkaline environments that a concrete slab may provide enhance the risk that plasticizers in flooring materials and acrylate based copolymers in adhesives will be hydrolysed. In alkaline hydrolysis the alcohols 2-ethyl-1-hexanol (EtHx) and n-butanol (BuOH), and other compounds, may be formed and emitted from the material, Alexandersson /12, 13/, Björk et al /14/, Persson /15/, Sjöberg /11/ and Wilke et al /7/. These specific degradation products have been found to correlate with increased SBS symptoms in damp buildings, Nordström et al /16/, and cause irritation of the human mucous membrane, Podlekareva et al /17/, and they are good tracers of the decomposition of flooring materials due to alkaline hydrolysis.

In addition to the emission from the flooring surface the volatile degradation products may also migrate down into the concrete substrate and be stored there for a long time, Sjöberg /6, 11, 18/. Since concrete is a porous substrate with ca 15 % pore volume there may be space for a considerable amount of those organic compounds to be stored. If the concrete surface condition later on changes, e g the flooring is removed or replaced, the stored degradation products may start to migrate upwards again and be emitted through the surface into the indoor air.

This paper describes and assesses two different methods used to determine the extent of stored decomposition products in concrete slabs, namely the flask headspace method (FHM) and the vial headspace method (VHM). The methods are often used by damage investigators who investigate indoor air problems and moisture damage in floor constructions. From the results of these types of measurements, the damage investigators often draw different conclusions regarding the condition of the floor constructions. At times it is a matter of deciding whether the moisture damage is still active, so that the source of moisture also must be dealt with, or whether it is only an old moisture damage which has now dried out, in which case only the remaining stored pollutants must be considered. In both cases it is of critical importance to determine how extensive the dispersion of the pollutants has been and to what depth they have penetrated into the concrete slab. This information can then be used in determining how extensive and effective the methods applied to decontaminate and restore the floor construction must be.

In view of this objective, it is of great importance to understand all the phenomena that govern the stored VOC transport within the concrete slab. Consequently, stored VOC concentration gradients in the concrete slab of five buildings were measured using both the FHM and the VHM methods. Apart from comparing the data and discussing the practical advantages and shortcomings of the two methods, the data were also used to derive the partition and diffusion coefficients of the VOC and concrete systems. The partition coefficients represent the storage capacities of the concrete for the VOCs. On the other hand, the diffusion coefficients determine the VOC kinetics of diffusion within the concrete slab. These two coefficients are typical inputs of physically-based sink or emission models that can be used to define adequate strategies for remediation. Here, particular emphasis is put on discussing their variations as a function of the

moisture content of the concrete (relative humidity in the air-phase of the pores), another parameter that was measured at each sampling point.

2. METHODS

2.1 VOC concentration in the gas phase

The equilibrium concentration of VOC in the gas phase (c_{air}, g_{voc}/m^3_{air}) was measured with the flask headspace method (FHM). This method was based on determination of the concentration of VOC in the air in the headspace of a flask, in equilibrium with a sample of the contaminated material.

The flask headspace method (FHM) was devised by Sjöberg /11/ and has been frequently used by the scientific community and practitioners in Sweden. Sjöberg /5/ Engström & Sjöberg /19/, Sjöberg & Engström /20/ Engström et al /21/. The FHM method consists of three stages; the first stage is sample preparation of the contaminated material, followed by headspace sampling of VOC on an adsorbent tube and finally analysis of the adsorbent tube by gas chromatography (GC-FID),

In the frame of the present study, the first stage of the FHM method was preparation of samples from the contaminated concrete slab. Samples were taken from several different depths in the substrate in order to determine the range of the penetration profile of contamination in the concrete slab. Moreover, samples were collected from a number different locations in order to determine the range of the problem area. A hammer drill was used to drill and chisel out the samples from different depths in the floor substrate. No cooling water was used in the process since there may be a risk of washing away water soluble organic compounds. It was also important to work quickly and not to warm up the material with the drill since the stored VOC may otherwise be emitted from the heated pieces of the sample.

The concrete samples at every depth were broken up into fragments of about 1 cm^3 size and about 5 - 10 pieces (ca 50 gram total) were quickly placed in a 250 ml glass flask, see Fig. 1. The flask was immediately sealed with a tightly fitting Teflon sealed cap and kept at room temperature (22°C) for three days before headspace sampling. The intention was to enable the VOC in the concrete sample to attain equilibrium with the headspace air in the flask at room temperature. It was therefore important not to raise the temperature of the sample before or during the conditioning period or at the time the headspace air was sampled. In a previous study, a conditioning period of three days had been found enough for equilibrium to be reached in the flask under these conditions. The achievement of an equilibrium state represents a situation where diffusion is completed: VOC concentrations in the air-phase of the pores are uniform throughout the concrete sample and the same as in the headspace of the flask. Therefore, the measured concentration is representative of the local pore air-phase concentrations that characterise the sorption equilibrium within the pores of the concrete samples. Furthermore, it is important to note that 1) the measured concentration embeds the contributions of adsorption / desorption processes at the pore surfaces, but also absorption / desorption processes in the liquid water filling some pores, and 2) not all the VOCs contained in the concrete samples have been diffused to the headspace of the flask at equilibrium: the main part of molecules are remaining at the pores surfaces and in the aqueous phase as a result of the air-phase, solid phase and aqueous phase partitioning.

Figure 1. Flask with two concrete pieces during sampling. Connected via Teflon tube to a TENAX tube and a plastic syringe.

In the second stage an adsorbent tube consisting of TENAX TA was used to sample the VOC in the air of the headspace. In a pre study Solid Phase Micro Extraction (SPME) was used with unsatisfactory results. On the occasion when the headspace air was sampled a carbon filter was attached to one of the gas proof connections in the cap, the air inlet tube (Figure 1). To the other connection a TENAX tube for air sampling was attached. During sampling a 20 ml plastic syringe was used to slowly draw a 20 ml volume of air through the TENAX tube. In order to prevent short circuiting, the air inlet was lowered via a Teflon tube to the bottom of the flask and the outlet was placed at the top. Since only 8% of the air in the flask was replaced during the sampling of the headspace the concentration in the air was not noticeably diluted. Pre studies of repeated samplings from a flask have shown that this dilution effect may hardly be measurable with this method.

The third and final stage in this method was analysis of the TENAX tube by gas chromatography and flame ionisation detector (GC-FID). In a pre study mass spectrometry (MS) had been used to identify the main peaks in the chromatogram.

The absorber tube was desorbed thermally. During the thermal desorption, the adsorbed VOCs were driven off from the adsorber and transported by the carrier gas to the stationary phase of the column. The column was kept refrigerated during the whole desorption phase. After the desorption phase the temperature in the column was raised according to a predetermined scheme; see Sjöberg /11/. No split of the gas stream was performed. When the temperature in the column increases, the VOCs begin to move through the column at different rates according to their characteristics such as e.g. molecule size. When the VOCs pass through the FID, in order, the electrical conduction increases and a higher current is produced as the amount of hydrocarbon radicals is increased. The variation in current was plotted as a function of time in a chromatogram, where each peak in the chromatogram represents an organic compound with a specific retention time. The total concentration or the concentration of the individual VOCs could be calculated with reference to the sampling volume for the analysed TENAX tube and the integrated area below the peaks.

2.2 VOC concentration in the material phase

The second method used in this study was the vial headspace method (VHM). Unlike, the FHM method, this method evaluates directly the total mass of a certain VOC that is contained in a concrete sample (C_{mtrl}, g_{voc}/m^3_{mtrl}).

The VHM method was devised by a commercial company which specialises in laboratory analysis of buildings. This company has in readiness a broad range of methods that any external consultant who needs to investigate a building with indoor air problems or moisture damage may use. The consultants receive instructions and may even borrow some of the needed equipment from the laboratory, and then take all the samples in the building. The samples are then sent to the laboratory through the post. The laboratory performs analyses on the sample and sends the result and some guidelines for the evaluation of the building's condition back to the consultant.

The VHM method consists basically of the same stages as the FHM method since it was a development and adaptation of the latter. All stages have nevertheless been developed and simplified in order to be safely handled by consultants without special training and to fit in better with the laboratory's selection of analysis methods.

In the first stage of the VHM method the drill cuttings from a hammer drill are sampled, which is an important simplification from the larger specimens used in the FHM method. A normal 12 mm hammer drill was used to drill a single hole and the drill cuttings were continuously collected from different depths in glass vials. About 3 g of the concrete cuttings was placed in each vial of 21 ml and quickly sealed by a cap. The only required condition of the concrete sample was that the pieces should be smaller than the opening of the vial (Øint = 12 mm). The vials were packed in a shock absorbent parcel and sent by normal post to the laboratory.

The second stage of the VHM method was extraction of the VOC in the sample and equilibrium with the headspace. When the sample arrived at the laboratory it was weighed for evaluation purposes and 5 ml of an extraction solution was added into each vial. The extraction solution basically consists of 90 % purified and deionised water (milliQ water), 10% ethanol and several internal standards. The vial was sealed with an aluminium cap with a rubber septum and placed in a shaking machine at 85°C for 30 minutes. According to internal studies performed by the method developer at the laboratory this was sufficient to extract the VOC in the concrete cuttings and reach equilibrium with the headspace.

The third stage of the VHM method was to analyse the headspace by gas chromatography and mass spectrometry (GC-MS). The sampling of the headspace was performed while the vial was still at the high temperature. The vials were placed on a turntable, an injection needle from a GC-MS instrument penetrated the septum and injected the overpressure of the headspace directly into the column. The VOCs in the headspace were separated in the GC column and identified by the MS, and the total amounts of different VOCs were quantified with reference to the external standard used and the mass of the concrete sample.

2.3 Moisture measurements

The moisture level in the concrete substrate was measured as relative humidity (RH) in the air in the pores of the material. The procedure used in this study is the common standard in Scandinavia for moisture measurements in most porous building materials. Regulations and critical values are also mostly expressed as a RH value.

Samples of the concrete were removed according to the FHM method and placed in test tubes made of silicate glass. Samples were taken from the concrete at several levels so that a moisture profile may be determined. In most cases the moisture samples were taken at exactly the same places and depths as the samples for FHM and VHM. The test specimens were broken up with a hammer and chisel, and pieces from each level were quickly taken and placed in test tubes which were sealed with rubber plugs. It was essential that the samples should be broken up and placed of in the test tubes quickly so that no moisture would be lost from the samples.

The next day RH probes were inserted into the test tubes. The measuring instrument was read when the system of samples, air in the test tubes and probe had reached equilibrium. The probe will relatively quickly reach equilibrium with the moisture level in the air in the test tube; what took the longest time was for the moisture to leave the concrete samples and reach equilibrium with the air in the test tube. It usually took about 24 hours before equilibrium was reached and the instrument could be read. The values obtained from the instrument were then converted into RH with reference to calibration curves. For this method, RH-probes HMP 36 and hand instrument HMI 31 from Vaisala were used.

3. MEASUREMENT RESULT

The measurements described in this paper were made in a number of buildings in central and southern Sweden during investigations of poor indoor environments. The main objective of the measurements was to demonstrate abnormal moisture levels and the presence of stored VOC in the concrete floor structure, i.e. to show whether there is moisture damage which has produced and stored degradation products in the floor, with the potential consequence of adversely affect indoor air quality at longer times.

3.1 Partition coefficient K

In situ measurements
Measurements A and B were made in situ in 2004 on the concrete slab in an office building in Sweden, built in 1979. During a renovation in 2001, bonded PVC flooring was laid on all floors in the building; this was also done in those areas of the building in which the concrete slab had had no flooring previously. Some time after the renovation, staff complained that they suffered from building related health problems of the SBS type when they were in the building. In a preliminary investigation, VOC from degraded adhesive was identified by the working environment engineer as a likely source of pollution in the indoor air.

Five rooms of the building were investigated. At all locations, RH and VOC contents in the concrete were determined using the methods presented above (both the VHM and FHM methods were used to measure the VOC concentrations).
When holes were made in the floor construction, it was found that at points A1 and A2 parts of the concrete slab were ca 100-130 mm thick and were laid on expanded plastics insulation. At these points the measurements showed that the moisture level in the concrete was ca 77-84% RH throughout, as shown in Tables 1 and 2; this is below the critical limit of 85% RH which is usually specified for bonded PVC flooring. In other parts of the concrete slab there was no such insulation and the slab rested directly on damp gravel without any moisture barrier. At measurement point B1 the concrete slab was ca 400 mm thick, and at the other two points (B2, B3) it was ca 110-120 mm thick. Moisture levels in the concrete where it had been laid directly on the gravel were very high, around 93 - <95% RH.

The results of measurements at all measurement points, A1 – B3, by both the FHM and VHM methods, are set out in Tables 1 and 2. It is evident from these results that there is a high concentration of VOC at all points near the surface, and that concentration diminishes with depth. This behaviour is, in general, the same for both n-butanol and 2-ethyl-1-hexanol, and is reflected in the same way in the results from both measurement methods. At a depth of ca 100 mm, the concentration of VOC in the concrete is much lower than at the surface, but in most cases it had penetrated even to this depth.

Before the renovation in 2001, the floor had been covered by PVC flooring in the area around measurement point A1. Around points A2 and B1 the concrete floor had had no covering at all. The floor around point B2 had previously had an application of clear epoxy varnish, and around point B3 there had been a rubber mat.

Table 1. Content of n-butanol and 2-ethyl-1-hexanol stored in a moisture damaged concrete slab. Moderate moisture level, about 80 % RH in the concrete subfloor.

			1-butanol			2-etyl-1-hexanol		
			VHM	FHM		VHM	FHM	
Label	Depth	RH	$\cdot 10^{-3}$	$\cdot 10^{-6}$	K	$\cdot 10^{-3}$	$\cdot 10^{-6}$	K
	mm	(%)	kg/m^3_{mtrl}	kg/m^3_{air}	$\cdot 10^3$	kg/m^3_{mtrl}	kg/m^3_{air}	$\cdot 10^3$
A1-1	0-15	77.0	12.0	1.4	8.54	66.7	0.79	84.4
A1-2	25-40	78.0	3.0	1.4	2.14	34.5	0.6	57.5
A1-3	50-70	80.0	3.2	1.3	2.48	25.3	1.4	18.1
A1-4	80-100	79.0	3.0	0.9	3.32	16.1	0.46	35.0
A2-1	0-15	78.5	4.4	1.3	3.36	110	1.1	100
A2-2	25-40	80.5	2.8	1.2	2.30	25.3	0.6	42.2
A2-3	50-70	83.0	-	0.8	-	9.9	0.23	43.0
A2-4	80-100	83.5	-	0.6	-	-	0.18	-
mean		79.9			3.96			54.4
std dev		2.3			2.43			28.9

Table 2. Content of n-butanol and 2-ethyl-1-hexanol stored in a moisture damaged concrete slab. High moisture level, about 95 % RH in the concrete subfloor.

			1-butanol			2-etyl-1-hexanol		
			VHM	FHM		VHM	FHM	
Label	Depth	RH	$\cdot 10^{-3}$	$\cdot 10^{-6}$	K	$\cdot 10^{-3}$	$\cdot 10^{-6}$	K
	mm	(%)	kg/m^3_{mtrl}	kg/m^3_{air}	$\cdot 10^3$	kg/m^3_{mtrl}	kg/m^3_{airl}	$\cdot 10^3$
B1-1	0-15	93.5	43.7	31	1.41	214	9.0	23.8
B1-2	25-40	93.5	22.1	19	1.16	101	4.2	24.1
B1-3	50-70	93.0	15.2	12	1.27	57.5	2.4	24.0
B1-4	80-100	94.0	5.30	6.3	0.84	14.7	1.1	13.4
B2-1	0-15	95.0	48.3	47	1.03	172	13	13.3
B2-2	25-40	95.0	36.8	32	1.15	85.1	3.6	23.6
B2-3	50-70	95.0	25.3	36	0.70	34.5	2.9	11.9
B2-4	80-100	>95	20.9	26	0.81	13.8	1.1	12.6
B3-1	0-15	94.0	46.0	48	0.96	71.3	4.8	14.9
B3-2	30-45	>95	32.2	29	1.11	8.30	0.55	15.1
B3-3	50-70	>95	18.9	22	0.86	-	0.40	-
B3-4	80-100	>95	32.2	19	1.69	-	0.18	-
mean		>94.4			1.08			17.6
std dev		>0.8			0.28			5.43

When the building was constructed in 1979, it was usual in Sweden to lay insulation only under certain parts of a building, the primary task of which was to save energy, but it also protected the concrete slab from rising damp from the soil. This was utilised later on in moisture resistant design. The fact that impervious PVC flooring was now laid at all places is decisive for the high moisture level in some parts of the floor. Soil moisture that rises up through the floor cannot now evaporate into the room air but remains below the flooring and creates a very high moisture level which, together with the alkaline environment in the concrete, decomposes the polymer chains in the floor adhesive and, to some extent, the plasticisers in the plastic flooring. Björk et al /14/, Sjöberg /6/.

Theoretical evaluation
Since measurements have been made of both the content of VOC in the concrete (VHM method) and the free concentration of VOC in air in equilibrium with the concrete (FHM method), the partition coefficient K [-] can be evaluated according to the equation

$$K = \frac{C_{mtrl}}{c_{air}} \qquad \left[\frac{g_{voc}/m^3_{mtrl}}{g_{voc}/m^3_{air}}\right] \Rightarrow [-] \qquad (1)$$

where C_{mtrl} [g_{voc}/m^3_{mtrl}] is the total content of a particular VOC per volume of material, and c_{air} [g_{voc}/m^3_{air}] is the concentration of a particular VOC per volume of air. As explained in paragraph 2.1, K embeds the contributions of adsorption at the pore surfaces, and absorption in the water filling some pores. In the field of indoor air quality, it is generally accepted that concentrations are low enough so that each of these sorption processes can be described through the definition of partition coefficients between the air-phase on the one hand, and the solid-phase or liquid phase on the other hand; Finally, K represents here the global binding capacity of the concrete for the measured moisture level (RH determines the amount of condensed water as well as the surface area available for VOC adsorption onto the pore walls).

In this study, this is done by calculating the ratio of pairs of values measured at the same point and at the same depth by the two methods VHM and FHM. These are set out in Tables 1 and 2.

It is shown that a moist concrete (ca 95 % RH) has a mean value of approximately $K = 1.1 \cdot 10^3$ [-] while a drier concrete (85%RH) has $K = 2.8 \cdot 10^3$ [-]. If the concrete evaluated above has a considerably lower moisture level, the higher values of the partition coefficient ($23 \cdot 10^3$) may very well be correct for the drier concrete.

3.2 Effective Diffusion coefficient D

In situ measurements
Measurements at points C-E were made in situ in a concrete slab laid on the ground in three different buildings. In all buildings the users had reported building related health complaints of the SBS type when they were present in the building. VOC from degraded floor adhesive was suspected to be a likely source of the pollutants in indoor air. These measurements were described for the first time in Sjöberg /11/.

Building C was a newly constructed hospital building where the staff, soon after moving in, began to experience symptoms of the SBS type in operating theatres etc where PVC flooring had been bonded to the floor for reasons of hygiene. This type of flooring is considered easy to keep clean in hospital premises since it can be laid with a portion drawn up along the wall and with welded joints which makes it possible for frequent wet cleaning to be carried out. Sampling

in this building was performed when emission damage was about 1 year old. Moisture level in the slab was ca 78% RH in the surface and ca 85% RH lower down in the slab. By making a back calculation of moisture transport, the investigating consultant could show that moisture level in the slab at the time the flooring was laid was considerably higher and exceeded the critical value of 85% RH for applying the adhesive for the PVC flooring.

Building D was a supervised accommodation building with the slab on the ground, with underlying insulation and underfloor heating. About 3.5 years after completion, the staff experienced such SBS and odour problems that the flooring was removed. The adhesive had lost almost all its tensile strength and was almost completely saponified. There was a strong pungent smell which the damage investigator identified as 2-ethyl-1-hexanol. At the time of the investigation, moisture levels were ca 91% RH at the concrete surface and 87% RH lower down. However, the investigation did not show whether or not the concrete had been much wetter earlier.

Building E was a school building constructed in the 1980s. The foundation construction was a slab on the ground with underlying insulation and PVC flooring bonded directly to the concrete floor. After about ten years, the users experienced building related health problems of the SBS type, and a damage investigator was called in. The preliminary assessment was alkaline hydrolysis of the floor adhesive. The investigation found that this was an old moisture damage which had been much wetter but has now "dried up". At the time of investigation the moisture level measured in the floor was ca 90% RH throughout the floor construction.

Pieces of concrete were taken from these concrete slabs at different depths and analysed with the FHM method for moisture level and VOC in the concrete. The results are shown in Figs. 2-4. In these results also it can be seen that there is a high concentration in the measurements nearest the surface, and a decrease in concentration with depth. In Buildings C and D the concentration of VOC at a depth of 100 mm is very near zero, while in building E which is much older penetration had also reached this depth. Distribution profiles of both n-butanol and 2-ethyl-1-hexanol have the same shape at all meassurement points. The spread of results at the same depth, which can be seen in Fig. 2-4, is probably due to the facts that samples had at times been taken from different places (cores) in the same room and sometimes from different places of the same core. If they originate from different parts of the same core, it is possible for the sample to have been taken from the area near the surface where it was exposed to an elevated temperature and may have lost some of its VOC content.

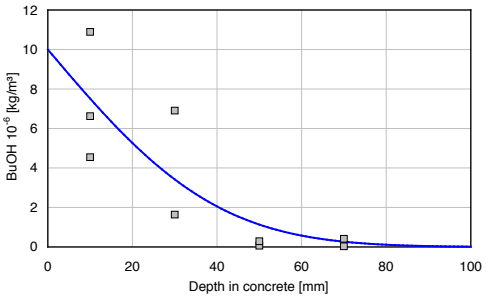

2a. Sample C. Distribution profile of n-butanol, ca 1 year old moisture induced damage.

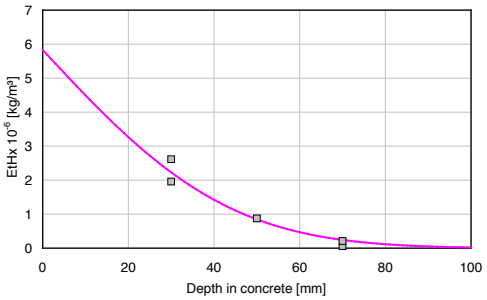

2b. Sample C. Distribution profile of 2-ethyl-1-hexanol, ca 1 year old moisture induced damage.

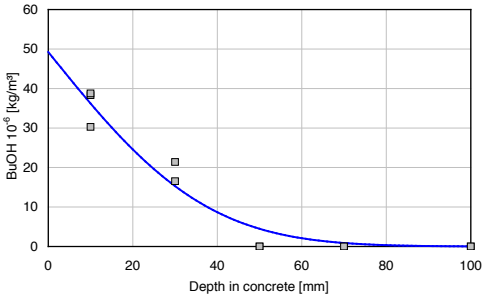

3a. Sample D. Distribution profile of n-butanol, ca 3.5 year old moisture induced damage.

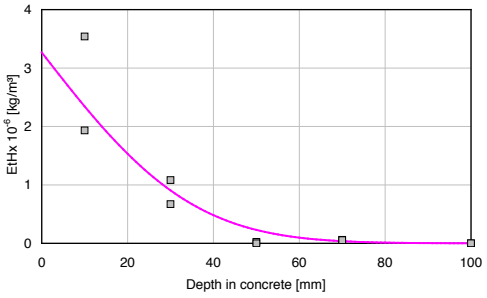

3b. Sample D. Distribution profile of 2-ethyl-1-hexanol, ca 3.5 year old moisture induced damage.

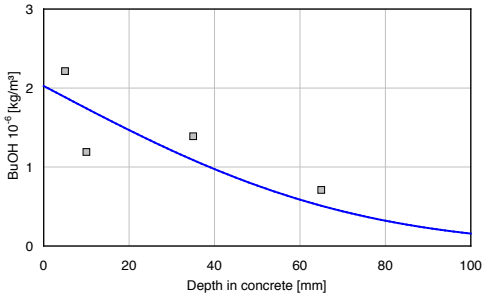

4a. Sample E. Distribution profile of n-butanol, ca 10 year old moisture induced damage.

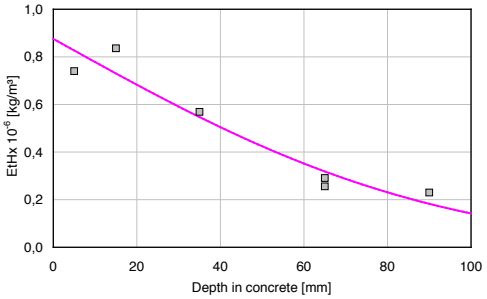

4b. Sample E. Distribution profile of 2-ethyl-1-hexanol, ca 10 year old moisture induced damage.

Figures 2-4. In situ measured distribution profiles of c_{air} in concrete substrate from three different buildings. The dots in the graphs are values measured with the FHM method and the curve is the best fit to the error function with the method of least squares.

Evaluation of D

The results of the measurements with method FHM on samples of the concrete slab from buildings C – D show that VOC from decomposition of the adhesive had penetrated deep into the concrete, about 50 – 100 mm. According to Crank /23/, the effective diffusion coefficient (D) can be evaluated with reference to Fick's second law. For such an evaluation it is necessary to know the penetration profile for a specific compound which has formed during incremental changes in a semi-infinite medium.

Under the assumption that the surface concentration c_S (g_{voc}/m^3_{air}) in the air-phase of the pores at the boundary layer between flooring and concrete surface had changed in stages from the initial value 0 to a constant value which then remained unchanged during the whole period, the fundamental incremental change requirement is satisfied. In view of the fact that the concentration at the bottom of the measured profiles, 100 mm from the surface, is very low, the depth of the slab may be considered infinite in this respect.

Fick's second law can then be solved with Equation 2 according to Crank /23/; this is the complement to the "error function".

$$c(x,t) = c_s \cdot \left[1 - erf\left(\frac{x}{2 \cdot \sqrt{D \cdot t}}\right)\right] \qquad \left[g_{VOC}/m^3_{air}\right] \qquad (2)$$

In Fig. 5, the complement to the error function has been calculated for a number of different combinations of D·t where t is the time during which the surface concentration was high after the incremental change.

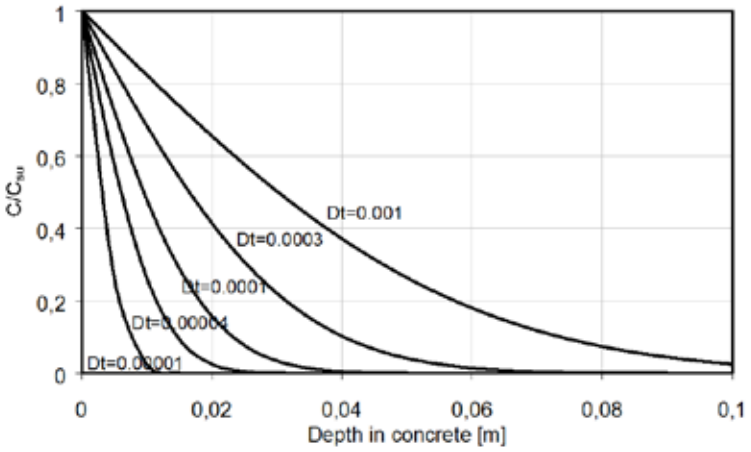

Figure 5. Solution of Fick's second law with the complement to the error function. The figures along the curves are the values of D · t; see Equation 2.

The best fit to the measured values for buildings C – E is plotted as a solid curve in Fig. 2 - 4. Curve fitting was performed by the method of least squares for differences in concentration at the different depths.
Surface concentration (c_s) for n-butanol was higher than for 2-ethyl-1-hexanol in all buildings, 2-49·10^{-6} (kg/m^3) as against 0.9-5.8·10^{-6} (kg/m^3). In spite of this the penetration depth and the shape of the distribution profiles were almost exactly the same, which means that D is of the same order of magnitude for n-butanol and 2-ethyl-1-hexanol in this study, see table 3. The effective diffusion coefficient D is in the range of 4-16·10^{-12} (m^2/s) for n-butanol and 3-19·10^{-12} (m^2/s) for 2-ethyl-1-hexanol.

Table 3. Measured and evaluated properties of n-butanol (BuOH) and 2-ethyl-1-hexanol (EtHx) in buildings C– E.

Building	Age (year)	RH [%]	C_S (·10^{-6} kg/m^3_{mtrl})		D (·10^{-12} m^2/s)	
			BuOH	EtHx	BuOH	EtHx
C	1	78-84	10	5.8	16	19
D	3.5	87-91	49	3.3	4.1	3.6
E	10	ca 90	2.0	0.9	5.2	8.4

The assumption regarding incremental change may not fully be correct, the surface concentration (c_s) which has been calculated may be seen as an effective mean value. The test specimens were in the range of 1 – 10 years old when the samples were taken. The concentration below the flooring may have changed during these years. The concrete may have dried out through the flooring in some cases, so that the reaction and thus the production of VOC had ceased.

The effective diffusion coefficient (D) which has been evaluated may also be a mean value for variable moisture conditions. The rate of penetration of VOC down into the concrete has probably been affected by the redistribution and drying of moisture in the concrete.

4. DISCUSSION

4.1 Measurement methods

As regards reliability, the results of measurements by the two methods appear to be of equal validity. Both methods gave relatively good agreement with expected values when profiles were measured at several levels or at several measurement points on the same damaged floor, although individual values may be different. To some extent, this provides confirmation that, physically, the gas-phase concentration is linearly correlated to the total VOC content of the material through the computed partition coefficient K. If the aim of the measurements is only to find whether there are elevated contents of VOC in the concrete, and to determine the penetration depth and the appearance of the profile, the methods may, on the whole, be regarded as equivalent. If, instead of this, the intention is to determine the partition coefficient (K), then it is necessary to apply the two methods..

Sampling in the field was considerably easier with the VHM method where it is possible to use drill cuttings of powder consistency which are produced when a hole ca 12 mm in diameter is cut with a normal hammer drill. It was easy to collect the cuttings from different depths and to put them into the small vials that are used for this method. On the other hand, the FHM method necessitates the use of a core drill and careful removal of a core without water cooling. This type of dry drilling is something that most operators want to avoid since it exposes the expensive equipment to hard wear.

Transport to the remote laboratory was also easier with the VHM method since these vials were only a fraction as large as the flasks used in the FHM method – 21 ml vials for VHM as against 250 ml flasks for FHM. This makes it much easier to pack the containers in such as way that there is no risk of breakage during transport by post. The FHM flasks also contain whole pieces of concrete which should preferably not rub against one another and crumble to powder, since the binding capacity of the material can then change markedly. With the VHM, the collected sample is preferably already in powder form since the subsequent extraction and analysis take place in a way that permits this.

Sample preparation in the laboratory and analysis of the headspace was much quicker with the VHM method, a few hours compared with several days for the FHM method. It can thus be concluded that the VHM method is the most practical and easy to use, especially for an unfamiliar user who only needs to make measurements in a few places.

4.2 Partition coefficient and storage capacity

The partition coefficient (K) for concrete is different for different gases; generally speaking, 2-ethyl-1-hexanol was found to have a value ca 10 times higher than n-butanol. This means that, for the same quantity of these compounds stored in the material, the concentration of n-butanol in the air in the concrete pores, under equilibrium conditions, is ca 10 times higher. Conversely, if the equilibrium concentration of these compounds in air is the same, there is about 10 times more ethylhexanol stored in the concrete under equilibrium conditions.

According to Sjöberg /11/ the partition coefficient may also be evaluated out of the diffusion coefficient in concrete for VOC in the gas phase, δ [m^2/s] together with the effective diffusion coefficient for VOC in concrete, D [m^2/s], Eq. 3. It is important that the same types of materials should have been evaluated in the different cases, since there are a large number of different concrete types with great variations in different types of material related properties.

$$K = \frac{\delta}{D} \qquad \left[\frac{m^2/s}{m^2/s}\right] \Rightarrow [-] \qquad (3)$$

The diffusion coefficient in normal house building concrete (water cement ratio approx 0.6 – 0.7) for n-butanol, δ is determined as $93 \cdot 10^{-9}$ m^2/s by Sjöberg /11/, Sjöberg & Nilsson /22/. The effective diffusion coefficient (D) for n-butanol in the same concrete is in the range of $4\text{-}16 \cdot 10^{-12}$ m^2/s according to Table 3.

This means that the partition coefficient (K) for n-butanol in concrete should be in the range of $5.8 – 23 \cdot 10^3$ [-]. Based on this assessment, the results presented in tables 1 and 2 seem to be reliable if it is borne in mind that there is probably a variation in the value of K between concretes of different moisture levels, as shown by Tables 1 and 2.

The moisture level in the concrete was also found to have great influence on the size of the storage capacity for these two compounds. At a moisture level of ca 80% RH (A1-A2), the mean value of K for n-butanol was 4.0 ± 2.4, with an outlier that distorts the standard deviation, and 54.4 ± 28.9 for ethylhexanol. At a moisture level of ca 95% RH (B1 – B3), the corresponding values of K for n-butanol were 1.1 ± 0.3 and for ethylhexanol 17.6 ± 5.4. On the other hand, the data presented in Table 1 and Table 2 indicate that the VOC contents of the concrete samples is from 3 to 3.5 times higher when the moisture level increases from ca 80 kg/m^3 to about 110 kg/m^3. In other words, the actual storage capacity of concrete (C_{mtrl}) increases with increasing humidity, although the intrinsic binding capacity of the material (K) is significantly lowered at higher humidity. The explanation most probably lies in the dual effects of moisture. When relative humidity is increased, both the water vapour concentration in the air-phase of the pores and the liquid water content of the material are increased. Consequently, the surface area available for gas adsorption at the pore surfaces is decreased and the competition between water vapour and VOC molecules for adsorption on the active sites of the pores is stronger. The combined effects of these two phenomena are reflected in lower K values. On the other hand, the increased water content favours the VOC absorption in the pores. Higher values of C_{mtrl} at high moisture levels indicate that this is probably the dominating process or, in other words, that the decrease in the amount of VOC adsorbed is largely offset by additional absorption in the aqueous phase.

This moisture related effect on K in concrete has also been demonstrated by Sjöberg /24/). The above values of the absolute moisture content of concrete, at different RH, are to be regarded as typical values that may however vary slightly depending on concrete type and quality.

4.3 Transport coefficient

In Table 3 there is an indication that the effective diffusion coefficient (D) for both n-butanol and 2-ethyl-1-hexanol is higher when the moisture level in concrete is lower. D for n-butanol is ca 3-4 times higher at about 80% RH than at ca 95% RH. For 2-ethyl-1-hexanol, the coefficient is of the order of 2-5 higher at the lower moisture level.

If a comparison is made instead of the difference in diffusion coefficient in concrete for VOC in the gas phase, δ [m^2/s], the difference between different moisture levels is even greater. For n-butanol at ca 90% RH, δ is ca $5 \cdot 10^{-9}$ (m^2/s) if the measured values are substituted into Equation 3. At ca 80% RH, the correspondiong value of δ is ca $64 \cdot 10^{-9}$ (m^2/s), i.e. about 13 times higher. For 2-ethyl-1-hexanol, the corresponding values are ca $110 \cdot 10^{-9}$ (m^2/s) at 95% RH and $1050 \cdot 10^{-9}$ (m^2/s) at 80% RH, i.e. the values are of about 9.5 higher.

This moisture dependent variation is probably related to the proportion of the pore system of concrete that is filled with liquid. Normally, concrete contains about 15% pores. As a rough estimate, two-thirds of these pores may be said to be filled at 95% RH if it is estimated that the concrete then contains 110 kg water per m^3, but to be only half filled at 80% RH when the concrete contains ca 80 kg water per m^3.

5. SUMMARY

All in all, the evaluated material coefficients K, D and δ show that when moisture damage occurs, the concrete is damp and has a low rate of moisture transport, which means that transport down into the concrete takes a long time. This is however compensated for by the high storage capacity of moist concrete which means that it can bind large quantities of VOC per unit volume, probably in some sort of liquid phase in the pores. When the moisture later on dries out, the moisture content of concrete decreases and the rate of transport increases. The probable result of this is that the decomposition products rapidly penetrate deeper into the concrete if there is an airtight flooring on top of the concrete slab. If, however, the flooring has been removed or replaced by a material that is more permeable, more of the stored decomposition products will instead be emitted from the floor surface and will be removed by the general ventilation system in the premises.

Under these conditions, it is of the greatest importance that the general ventilation should have a sufficient rate of flow to collect the emissions from the floor and remove them from the building. In buildings with stored pollutants in the floor, it is therefore highly inadvisable to make use of the extract air from rooms with emission damaged floors and to use this as part of the return air in the building in order to reduce running costs in this way.

In conclusion, it should be pointed out that this paper does not discuss what measures should be taken in buildings with stored pollutants in concrete floors. Great care should be instead be taken in selecting such measures, with reference to the quantity of stored pollutants, the rate of flow of general ventilation and the type of use of the building. The occupants of residential buildings, schools or offices often have greater demands regarding the quality of indoor air than workers in a factory or warehouse.

REFERENCES

1. Gustavsson H, and Lundgren B. 1997. Off-gassing from building materials: a survey of case studies. In The Workplace, Fundamentals of Health, Safety and Welfare. Brune D, Gerhardsson G, Crockford GW, and Dáuria D, eds. International Labor Office, Geneva, Vol. 1, pp 533-555.
2. Wiglusz R, Igielska B, Sitko E, Nikel G, and Jarnuszkiewicz I. 1998. Emission of volatile organic compounds (VOCs) from PVC flooring coverings. Bull. Inst. Marit. Trop. Med. Vol. 49, pp 101-107.

3. Cox, S., Little, J. and Hodgson, A. (2002) Predicting the emission rates of volatile compounds from vinyl floorings, Environ. Sci. Technol., 36, 709–714.
4. Saarela, K., Villberg, K. and Lukkarinen, T. (2000) Emissions from materials and structures. In: Seppänen, O. and Säteri, J. (eds) Proceedings of Healthy Buildings
5. Sjöberg A. 2000. Concrete Floors as Secondary Emission Source. Proceedings of Healthy Buildings 2000. Espoo, Finland. 6-10 August 2000. Vol 4. pp 417-422.
6. Sjöberg A. (2007) An experimental parametric study of VOC from flooring systems exposed to alkaline solutions. Indoor Air; 17, 450-457.
7. Wilke, O., Jann, O. and Bröner, D. (2004) VOC- and SVOC-emissions from adhesives, floor coverings and complete floor structures, Indoor Air, 14, 98–107.
8. Wieslander G, Norbäck D, Nordström K, Wålinder K, and Venge P. 1999. Nasal and ocular symptoms, tear film stability and biomarkers in nasal lavage, in relation to building dampness and building design in hospitals. Int. Arch. Occup. Environ. Health. Vol. 72, pp 451-451.
9. Norbäck D, Wieslander G, Nordström K, and Wålinder R. 2000. Asthma symptoms in relation to measured building dampness in upper concrete floor construction, and 2-ethyl-1-hexanol in indoor air. Int. J. Tuberc. Lung Dis. Vol. 4, pp 1016-1025.
10. Bornehag C. G, Sundell J, Hagerhed-Engman L, Sigsggard T, Janson S, Aberg N, and the DBH Study Group. 2005. "Dampness" at home and its association with airway, nose, and skin symptoms among 10,851 preschool children in Sweden: a cross sectional study. Indoor Air; 15 (Suppl 10): 48–55
11. Sjöberg A. (2001) Secondary Emission from Concrete Floors with Bonded Flooring Materials, Göteborg, Department of Building Materials, Chalmers University of Technology (Report P-01:2).
12. Alexandersson, J. (2003) Emissions from adhesives and floor coverings on aggressive substrate_. In: Tham, K.W., Chandra, S. and Cheong, D. (eds) Proceedings of Healthy Buildings 2003, Vol. 1, Singapore, 7–11 December, 184–188.
13. Alexandersson, J. (2004) Secondary Emissions from Alkali Attack on Adhesives and PVC Floorings, Lund, Division of Building Materials, Lund University (Report TVBM-3115).
14. Björk, F., Eriksson, C.-A., Karlsson, S. and Khabbaz, F. (2003) Degradation of components in flooring systems in humid and alkaline environments, Construction and Building Materials, 17, 213–221
15. Persson, B. (2002) Compatibility between flooring materials and concrete, Materials and Structures, 35, 170–182.
16. Nordström, K., Norbäck, D., Wieslander, G. and Wålinder, R. (1999) The effect of building dampness and type of building on eye, nose and throat symptoms in Swedish hospitals, Journal of Environmental Medicine, 1, 127–135.
17. Podlekareva, D., Pan, Z., Kjærgaard, S. and Mølhave, L. (2002) Irritation of the human eye mucous membrane caused by airborne pollutants, Int. Arch. Occup. Environ. Health., 75, 359–364.
18. Sjöberg A. (2003) Penetration of degradation products from adhesive into concrete. Proceedings of Healthy Buildings 2003, Singapore.
19. Engström C, Sjöberg A 2002. Measurements of stored decomposition products from flooring adhesives in a concrete floor, used for choosing floor surface constructions. Proceedings of the 6th Symposium on Building Physics in the Nordic Countries. Trondheim, Norway . 17-19 June 2002.
20. Sjöberg A, Engström C. 2003. New method to measure stored VOC in concrete. Proceedings of Healthy Buildings 2003, Singapore.

21. Engström C. Hall T. Sjöberg A. 2003. A field study of the distribution of degraded flooring components in a concrete floor. Proceedings of Healthy Buildings 2003, Singapore.
22. Sjöberg A, Nilsson LO (2002) A model for secondary emissions from bonded flooring materials on concrete floors. Proceedings of Building Physics 2002, 6th Nordic Symposium. Trondheim, Norway 17-19 June 2002. pp 721 – 728.
23. Crank J. 1975. The Mathematics of diffusion. Clarendon Press, Oxford
24. Sjöberg A. 2009. Combined Binding Capacity of VOC and H_2O in Building Materials. Proceedings of Healthy Buildings 2009, Syracuse, US. Paper 321.

Influence of different amount of fly ash for early age concrete containing Swedish cement - Part I: Tendency model for heat and strength development for variable fly ash content

Sofia Utsi
PhD in structural engineering, LTU
ProDevelopment AB
Storgatan 9
972 38 LULEÅ, SWEDEN
sofia.utsi@prodevelopment.se

Jan-Erik Jonasson
Professor in Structural engineering
Luleå University of Technology
971 87 LULEÅ, SWEDEN
jan-erik.jonasson@ltu.se

ABSTRACT
This paper presents a numerical tendency model for evaluation of heat and strength development for concrete containing fly ash in different amounts. With the presented model, parameters for heat and strength development calculations in early age can be calculated. It facilitates the possibility to evaluate e.g. form removal times and estimations of need for protection against early freezing for concrete mixes containing fly ash in different amounts.

Keywords: Flyash, heat of hydration, strength growth, early age concrete, hardening control

1 INTRODUCTION

1.1 Objectives and Scope

The main objective with the work presented in this paper is to establish a numerical tendency model for heat development and strength growth in concrete containing fly ash in different amounts and the paper is a part of [1].

Fly ash in concrete is not common in Swedish concrete production, mainly because of the lack of national produced fly ash. However, there is an increased interest among concrete producers to use fly ash in concrete, mainly as a replacement of a part of the cement content. A tendency model is needed to assess the effects of using fly ash in different applications. The strength, as well as generated heat, is dependent on the fly ash content in relation to the cement content, and a model to predict strength and heat have to consider the actual binder composition in a consistent way.

The presented tendency model is based on laboratory tests were the heat development is tested with semi-adiabatic tests and the strength development is measured by compression tests of cubes cured in water at different temperature levels. Tests have been performed on concrete with two different water-to-cement ratios containing fly ash in four different amounts; 6, 11, 25 and 40 % of the cement content. Further, tests have been performed on concrete mixes composed with two different efficiency factors; 0.4 and 0.8.

The tested mixes are composed with one type of fly ash, one type of aggregate, one type and dosage of superplastiziser as well as one type of cement with the aim to evaluate the pure effect from the fly ash content in combination with two levels of equivalent water-to-cement ratios. The tendency model is expected to reflect the combination of variable fly ash and variable water content. The tests have been performed on the Swedish Anläggningscement and similar cement types are available in Norway and Denmark. The used fly ash is from Germany and the used aggregate is a Swedish crushed aggregate.

This part of the paper, Part I, is limited to the development of the numerical tendency model. Part II of this paper [2] contains an application of the suggested tendency model on an assumed civil engineering structure where form stripping times and the risk for early freezing is calculated for different amounts of fly ash. In Part II the tendency model is also applied on another group of concrete.

1.2 Heat development and strength growth

Hydration in concrete is an exothermic chemical reaction. A few hours after the concrete have been mixed, the reaction between water and cement starts to generate heat and the strength growth begins. The strength development is strongly related to the heat development, which is influenced by the chemistry of the binder and by the curing temperature. The temperature effect on the rate of hardening can be expressed by the temperature factor, which also is known as the "maturity function".

For the hardening control of young concrete, the knowledge of the maturity and the temperature development is essential to be able to plan and control the production properly. It involves estimations of form removal times, assessments of necessary times for moisture curing of the concrete surface, and estimation of conditions to avoid too early freezing of the young concrete.

1.3 The effect of fly ash on young properties

Fly ash is a pozzolanic material, which means that it reacts with the calcium hydroxide $Ca(OH)_2$ that is produced when cement reacts with water. When fly ash reacts with $Ca(OH)_2$, calcium silicate hydrate (CSH) is formed, which means that the content of the durable material (CSH) increases in the concrete, [3] and [4].

The in-corporation of fly ash in concrete can be performed in three different ways, [5]:

- Exchange cement with fly ash by weight on a 1:1 basis
- Exchange parts of the cement and parts of the aggregate
- Adding fly ash in addition to the cement as a part of the fine aggregate

According to [6] fly ash contributes to the concrete strength in three different ways; by a water reduction because demanded workability can be received at lower water contents when fly ash is added, by an increased effective paste volume and by the pozzolanic reaction. The first two will influence the early concrete strength while the latter will contribute to increased long-term strength.

Any replacement of Portland cement with fly ash in concrete will influence the compressive strength, and the strength growth may be low in the beginning, but the growth usually continues up to at least 6 months [5]. It is well known that in order to maintain the 28-days compressive strength the amount of fly ash added always exceeds the amount of cement removed [6]. This points out that the relation between fly ash and cement is one of the decisive parameters describing the strength growth.

2 LABORATORY TESTS

2.1 Material properties and Test program

Concretes containing different amounts of fly ash can be characterized by the equivalent water-to-cement ratio, w_0/C_{equ}, calculated according to Eq. 1. In recommendations and codes the efficiency factor in Eq. 1 is given specific values.

$$\frac{w_0}{C_{equ}} = \frac{w_0}{\left(C + k \cdot FA\right)} \tag{1}$$

where w_0= mixing water content [kg/m^3], C_{equ}= equivalent cement content [kg/m^3], C = cement content [kg/m^3], FA = fly ash content [kg/m^3], and k = efficiency factor [-]. Also the allowed maximum content of fly ash is regulated in recommendations and codes with different values depending on the application situation.

The tests have been performed due to the test program presented in Table 1, where two different equivalent water-to-cement ratios with four different fly ash contents have been included. This generates 18 different mixes. For each value of w_0/C_{equ}, either 0.4 or 0.5, the water content and the equivalent cement content have retained constant. The use of an efficiency factor less than one will result in an increase of the total binder (cement plus fly ash) content, and in the present test series the effects of using k = 0.4 and 0.8 are investigated, where k = 0.4 is according to [8]. With the limitations in [8], i.e. k = 0.4, the effect of fly ash regarding heat reduction may not be fully utilized because the total binder content will increase when only part of the fly ash is allowed to be included in the water-to-cement ratio. The demands in [8] are based on the demands on 28-day compressive strength, which means that the combination of demanded 28-day compressive strength together with a significant heat reduction is difficult to achieve.

The water-to-cement ratio, w_0/C, is calculated by rearrangement of Eq. 1 as

$$\frac{w_0}{C} = \frac{w_0}{C_{equ}} \cdot \left(1 + k \cdot \frac{FA}{C}\right) \tag{2}$$

All tests presented here are produced with concrete based on the Swedish cement type Anläggningscement Std P Degerhamn CEM I 42.5 N MH/SR/LA, produced by Cementa AB aimed for civil engineering structures, and the fly ash is black coal fly ash from Rostok, Germany, produced by Warnow-Füller. It fulfils demands according to SS-EN 450 [7] and is allowed for concrete production according to demands stated by SS-EN 206 [8]. The aggregates are Swedish crushed aggregates.

Air entraining agent has been included in all mixes. In the numerical evaluation, the amounts of the constituents have been slightly revised with respect to the measured air content.

Table 1 - Mix compositions for performed heat development and strength growth tests

Mix No.	*FA/C*	W_0/C_{equ}	*k*	*C* kg/m^3	*FA* kg/m^3
1	0	0.40	-	430	-
2	0.06	0.40	0.4	420	25.2
3	0.11	0.40	0.4	412	45.3
4	0.25	0.40	0.4	391	97.8
5	0.40	0.40	0.4	370	148
6	0.06	0.40	0.8	410	24.6
7	0.11	0.40	0.8	395	43.5
8	0.25	0.40	0.8	358	89.5
9	0.40	0.40	0.8	326	130
10	0	0.55	-	370	-
11	0.06	0.55	0.4	361	21.7
12	0.11	0.55	0.4	354	38.9
13	0.25	0.55	0.4	337	84.2
14	0.40	0.55	0.4	319	128
15	0.06	0.55	0.8	353	21.1
16	0.11	0.55	0.8	340	37.4
17	0.25	0.55	0.8	308	77.0
18	0.40	0.55	0.8	280	112

2.2 Heat development

Due to chemical reactions between cement and water, heat is generated during the hardening process of concrete. The heat development can be determined with calorimetric methods and in this paper a semi-adiabatic method has been used. Cylinder samples of concrete have been cured under semi-adiabatic conditions, and the temperature in the samples has been registered. After about two weeks the specimen has been heated, still situated inside the semi-adiabatic equipment, and the cooling phase has been registered. The exchange of heat with the surroundings during the hydration phase, expressed by the so called heat cooling ratio, is then possible to calculate. This is realized to be able to compensate for the loss of heat during the test period, see further [9].

All tested mixes are evaluated regarding generated heat for the total binder content, expressed as a function of temperature equivalent time, t_e, by Eq. 3 from [10].

$$W_B = \frac{W_{tot}}{B} = W_U \cdot \exp\left[-\lambda_1 [\ln(1 + \frac{t_e}{t_1})]^{-\kappa_1} \right] \quad (3)$$

where W_B = generated heat by weight of binder [J/kg], B = binder content, here the sum of cement and fly ash content [kg/m^3], W_{tot} = generated heat at testing [J], W_U [J/kg], t_1 [h], and κ_1 [-] are individual fitting parameters valid for each tested mix. λ_1=1 [-] has been used for all evaluations because it is not an uncoupled parameter. For the denotation t_e, see further Eq. 5.

2.3 Strength Growth

The strength development in concrete is influenced by the temperature. By curing in different temperatures and testing the compressive strength, it is possible to determine the effect of temperature on the strength development and to determine the maturity function.

Concrete cubes of 100x100x100mm are stored in three different water temperatures: 5°, 20° and 35°, respectively. The concrete temperature is registered continuously and the strength development is studied by testing the compressive strength at four occasions between 8 and 168 h after casting. Additional cubes are cured under water in 20°C to determine the 28-day and 91-day compressive strength. All cubes are tested wet.

The strength growth for all tested mixes is evaluated according to Eq. 4, where the lower formula is proposed by [11]. The upper formula for $t_e \le t_A$ is intended for very early age strength estimations to be able to assess trowelling and slipform actions, but here no measurements are performed in this region.

$$f_{cc}(t_e) = \begin{cases} (t_e / t_A)^{n_A} \cdot f_A & \text{for } 0 \le t_e < t_A \\ \exp\left[s \cdot \left(1 - \sqrt{\frac{672 - t_S}{t_e - t_S}} \right) \right] \cdot f_{28} & \text{for } t_e \ge t_A \end{cases} \quad (4)$$

where f_{28} [MPa], s [-], t_S [h], t_A[h] and n_A [-] are fitting parameters. The magnitude of f_A [MPa] is calculated using the lower formula in Eq. 4 for $t_e = t_A$.

2.4 Maturity Function

The properties of the hardening concrete are here based on the maturity concept expressed by the temperature equivalent time, t_e, described by [12] as

$$t_e = \int_t \beta_T \cdot dt \quad (5)$$

where t = time [s, h or d], β_T is the factor for temperature sensitivity, often called the maturity function, which can be expressed [13] and [14] by:

$$\beta_T = \begin{cases} exp\left[\theta \cdot \left(\frac{1}{293} - \frac{1}{T+273}\right)\right] & \text{for T > -10 } ^\circ C \\ 0 & \text{for T} \leq \text{-10 } ^\circ C \end{cases} \quad (6)$$

where (Jonasson, 1984)

$$\theta = \theta_{ref} \cdot \left(\frac{30}{T+10}\right)^{\kappa_3} \quad (7)$$

where θ_{ref} [K] and κ_3 are fitting parameters according to best fit with test data.

3 NUMERICAL TENDENCY MODELS

3.1 Maturity function

For the tested mixes, Nos. 1-18, the maturity function has been evaluated by analyzing the results from the strength development at varying temperature according the procedure described in [9]. No significant variation between the tested mixes regarding the θ-value could be found. It is thus concluded that the variation is randomly spread irrespectively from fly ash content or w_0/C ratio. All tested mixes are represented by the same maturity function plotted in Figure 1 by the use of Eq. 7 with the following numerical values:

$$\text{For all concretes} \begin{cases} \theta_{\text{ref}} = 3870 \ \text{K} \\ \kappa_3 = 0.57 \end{cases}$$

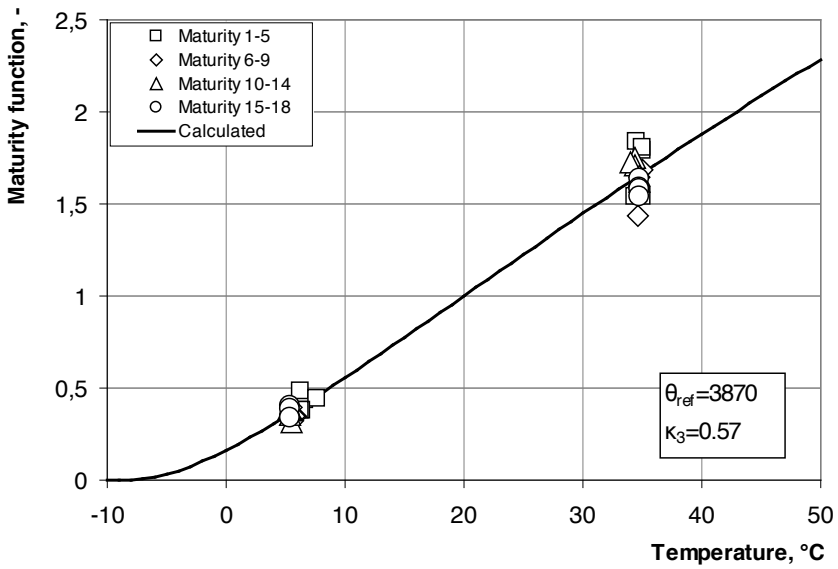

Figure 1 - Maturity function valid for tested mixes 1-18.

3.2 Heat development

Mixes 1-18 are individually evaluated in accordance with Eq. 3, and Figures 2-3 show the evaluation for mix 1 and mix 11. It can be concluded that Eq. 3 satisfactory describes the hydration process. Calculations can recreate measured temperatures within approximately ± 1°C.

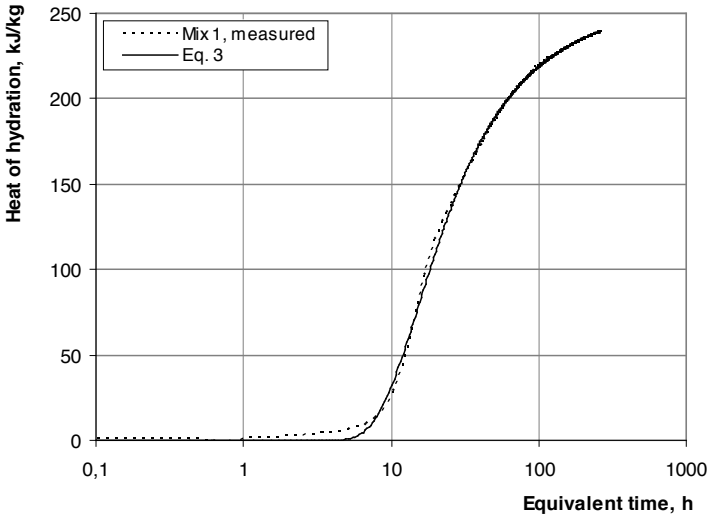

Figure 2 - Individual evaluation of the heat of hydration for mix 1.

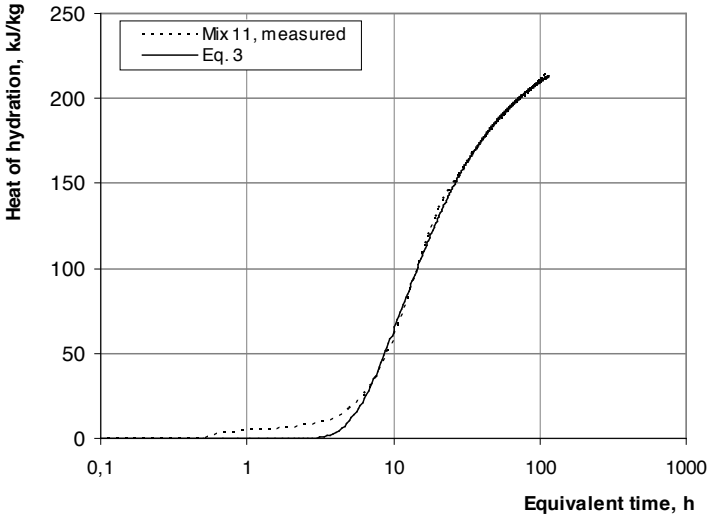

Figure 3 - Individual evaluation of the heat of hydration for mix 11.

Tendencies regarding the heat of hydration due to w_0/C ratio and fly ash content have been evaluated. In the tendency model the effect on the hydration heat is assumed to be separated into

effects of the w_0/C ratio and of the fly ash content, respectively. This assumption makes it easier to choose which formula to be used to model different observed effects in a consistent way.

The subsequent relations, Eqs. 8 – 14, describing the heat of hydration, with parameters for use of Eq. 3, have shown to give a satisfactory agreement with the tested heat developments for the concrete mixes 1- 18.

$$W_U = W_{ref} \cdot \gamma_w \tag{8}$$

$$\kappa_1 = \kappa_0 \cdot \gamma_1 \tag{9}$$

with the following numerical expressions:

$$W_{ref} = 275 - 20 \cdot exp\left[-\left(\frac{w_0 / C}{0.65} \right)^2 \right] \text{ [kJ/kg]} \tag{10}$$

$$\gamma_w = 1 - 0.69 \cdot \frac{FA}{C} \quad (\geq 0.3) \tag{11}$$

$$\kappa_0 = 1.65 + 0.35 \cdot exp\left[-\left(\frac{w_0 / C}{0.55} \right)^7 \right] \tag{12}$$

$$\gamma_1 = 1 + 0.2 \cdot \left(1 - exp\left[-\left(\frac{FA / C}{0.8} \right)^2 \right] \right) \tag{13}$$

$$t_1 = 8 + 2.7 \cdot exp\left[-\left(\frac{w_0 / C}{0.54} \right)^{25} \right] \text{ [h]} \tag{14}$$

In Figures 4-6 the individually evaluated W_U, t_1 and κ_1 are plotted versus the, for use in the tendency model, calculated values for mixes 1-18. The parameters evaluated in the presented model show satisfactory agreement when compared with each individual evaluation.

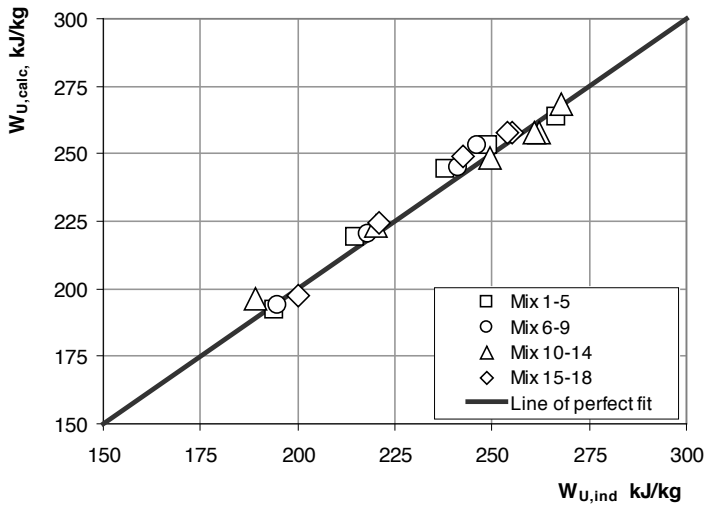

Figure 4 - Calculated $W_{U,calc}$ plotted versus the individually evaluated $W_{U,ind}$ for mixes 1-18.

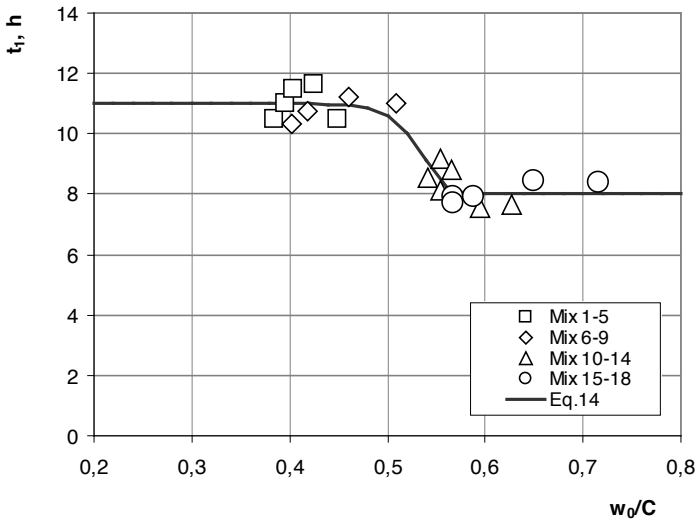

Figure 5 - Calculated t_1 plotted versus the water-to-cement ratio.

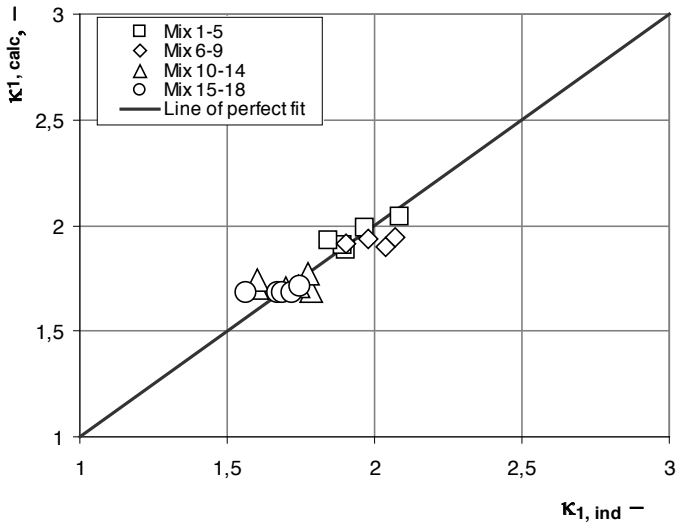

Figure 6 - κ_1 plotted versus the individually evaluated for mixes 1-18.

Figure 7 shows the predicted heat of hydration calculated with the suggested tendency model and it is compared to the measured values for mixes 1-5. It can be concluded that the heat of hydration can be described acceptably with the presented model.

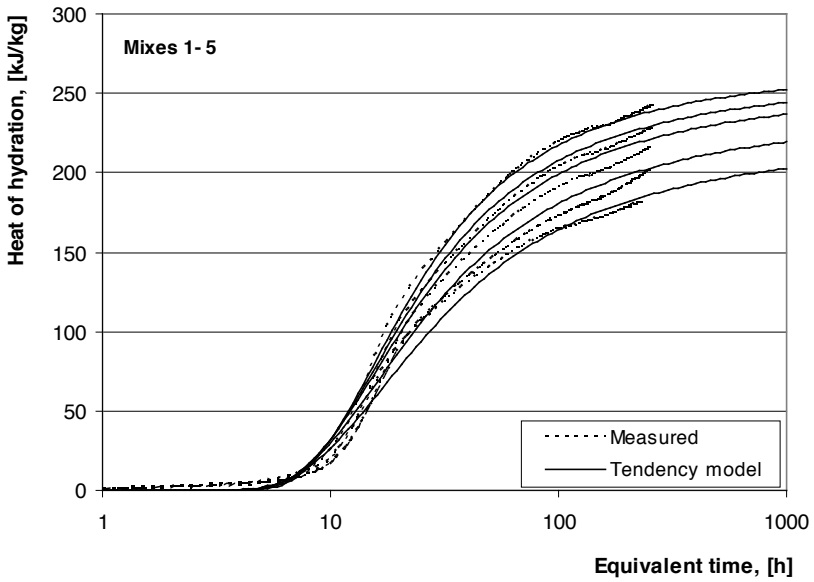

Figure 7 - Measured heat of hydration in comparison to the, with the tendency model calculated, heat of hydration for mixes 1-5.

3.3 Strength growth

The individual evaluation regarding the strength growth for mixes 1-18 has been performed with Eq. 4. The results for mix 1 and mix 18, the mixes showing the highest and lowest 28-day compressive strength, are presented in Figures 8-9. It can be concluded that a satisfactory agreement can be received by using Eq. 4 for all tested mixes up to the 28-day compressive strength. Satisfactory agreement can also be received for the 91-day compressive strength for concrete without fly ash. For concrete with higher w_0/C ratio containing fly ash, the increase in compressive strength between 28 and 91 d will be relatively high. This increase can not be described with the use Eq. 4 alone. The 91-day compressive strength is expressed with a separate formula, see further Eq. 25.

Tendencies regarding the strength development due to w_0/C ratio and fly ash content have been interpreted and a numerical tendency model has been established. Analogous with the numerical tendency model for the heat development, the formulation of the strength growth is assumed to be separable regarding effects of w_0/C ratio and fly ash content. The dotted lines in Figures 8-9 are examples where the proposed tendency model is applied.

The numerical tendency model can be described by:

$$f_{28} = f_{ref} \cdot \gamma_f \tag{15}$$

$$s = s_0 + (s_1 - s_0) \cdot \gamma_s \tag{16}$$

with the fitting parameters:

$$f_{ref} = 2700 \cdot exp\left[-\left(80 \cdot \frac{w_0}{C} \right)^{0.378} \right] \text{ [MPa]} \quad (17)$$

$$\gamma_f = 1 + 0.35 \cdot \frac{FA}{C} \quad (\leq 1.2) \quad (18)$$

$$s_0 = 0.41 - 0.14 \cdot exp\left[-\left(\frac{w_0/C}{0.5} \right)^5 \right] \quad (19)$$

$$s_1 = 0.36 \quad (20)$$

$$\gamma_s = 1 - exp\left[-\left(\frac{FA/C}{0.21} \right)^2 \right] \quad (21)$$

$$t_S = 3 + 2.5 \cdot \left(1 - exp\left[-\left(\frac{FA/C}{0.3} \right)^2 \right] \right) \text{ [h]} \quad (22)$$

$$t_A = 1.5 \cdot t_S \text{ [h]} \quad (23)$$

$$n_A = 3 \quad (24)$$

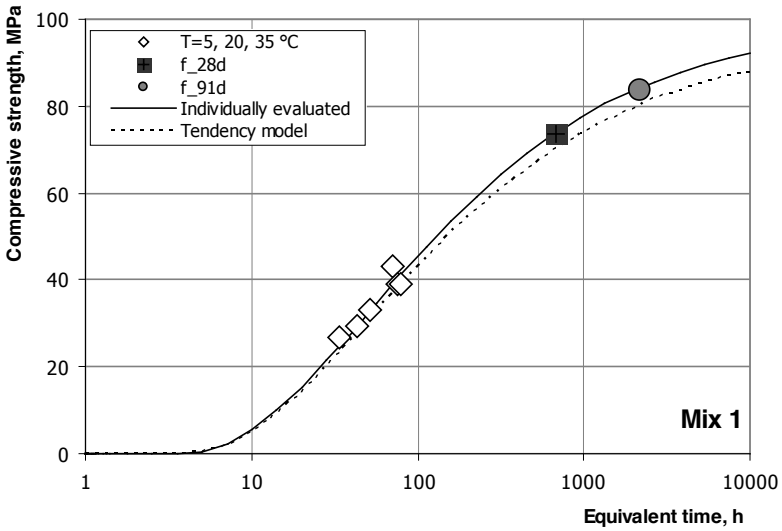

Figure 8 - Individually evaluated compressive strength for mix 1 with measured f_{28} = 73.8 MPa. The dotted line is compressive strength calculated with the tendency model.

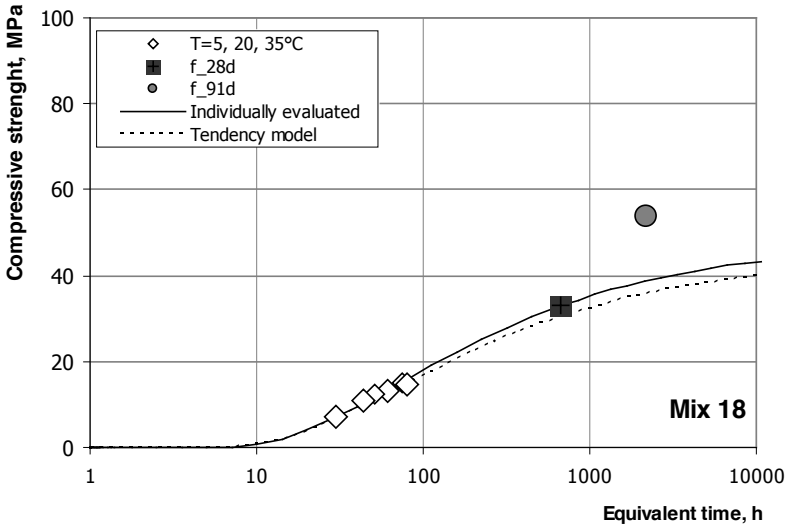

Figure 9 - Individually evaluated compressive strength for mix 18 with measured f_{28} *= 33.0 MPa. The dotted line is compressive strength calculated with the tendency model.*

In Figures 10-12, the measured f_{28} and individually evaluated s and t_S are plotted versus the calculated values using the tendency model for mixes 1-18.

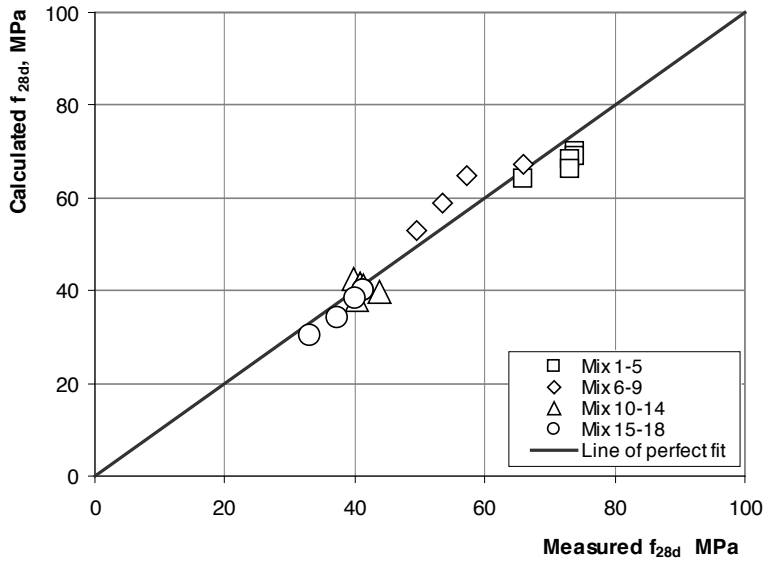

Figure 10 - Calculated f_{28} *plotted versus the measured for mixes 1-18*

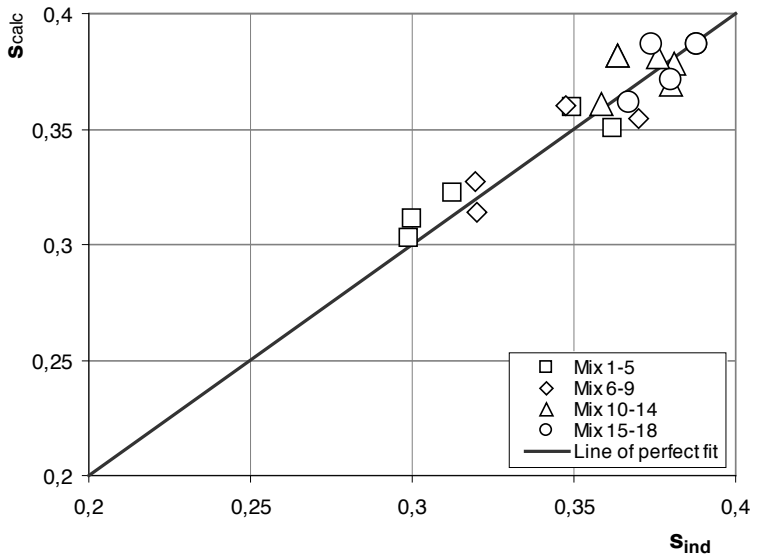

Figure 11 - Calculated s plotted versus the individually evaluated for mixes 1-18.

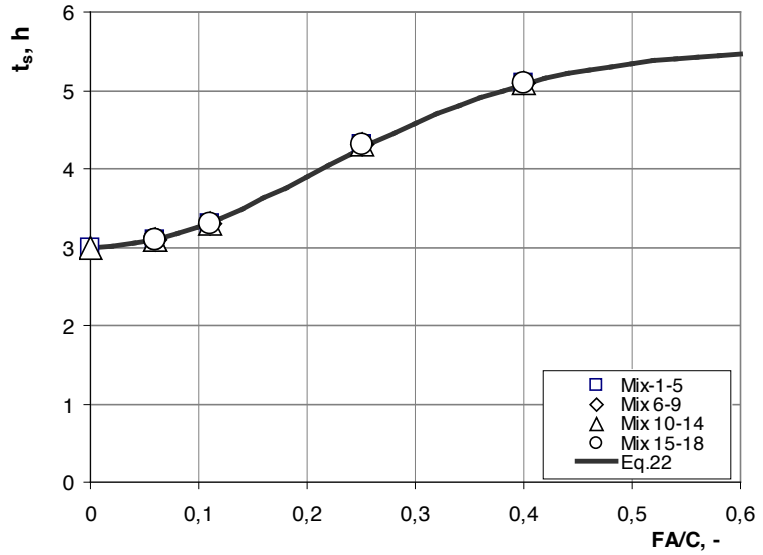

Figure 12 - t_s as a function of the fly ash content.

The increase of 91-days compressive strength, an observed effect of higher fly ash contents, is not reflected by Eq. 4. The needed additional formulas to catch this strength rise are expressed as

$$f_{91} = f_{91,ref} \cdot \gamma_{91} \tag{25}$$

$$\gamma_{91} = 1 + \gamma_{max} \cdot \lambda_{FA} \tag{26}$$

$f_{91,ref}$ is calculated with Eq. 4 for t_e =91d =2184h. γ_{91} is a parameter larger than one, which will increase for increased the fly ash content.

The 91-day compressive strength is described with numerical parameters according to:

$$\gamma_{max} = 0.42 \cdot \left(1 - exp\left[-\left(\frac{w0/C}{0.54} \right)^5 \right] \right) \quad (27)$$

$$\lambda_{FA} = 1 - exp\left[-\frac{FA/C}{0.16} \right] \quad (28)$$

A comparison between individually evaluated and calculated enlargement factors for the 91-day compressive strength is illustrated in Figure 13. It can be noticed that for mix 18 (=highest γ_{91} value in Figure 13), the increase is almost 40 % in comparison with the value only using Eq. 4. The model is chosen to be most accurate for higher fly ash contents, as small amounts of fly ash showed a higher variation in the tested results, see the lower-left part of Figure 13.

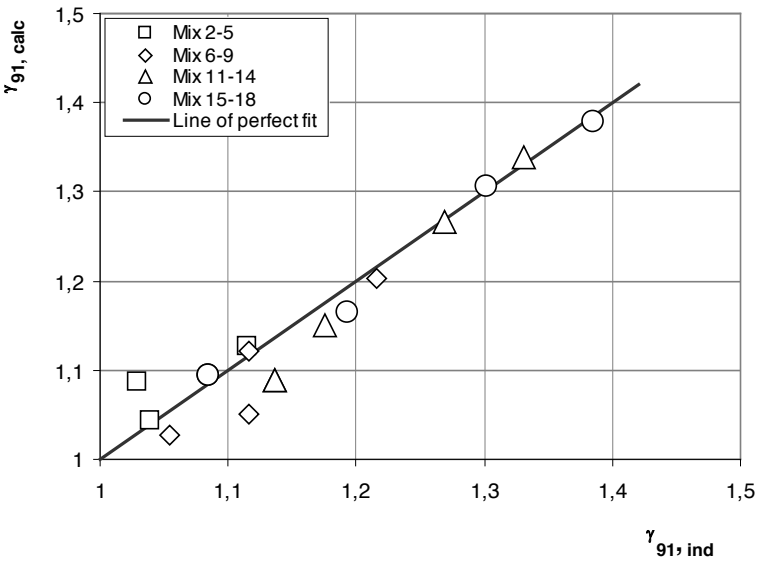

Figure 13 - Calculated γ_{91} values using the tendency model plotted versus individual evaluated values

4. CONCLUSIONS

- The presented numerical tendency model is a useful tool for estimating heat and strength development when fly ash is added in varying amounts. The model is based on the effect from water-to-cement ratio and fly ash content in relation to cement content.

- The suggested model is based on a test series where all parameters except the water-to-cement ratios and fly ash content have been constant.

- The suggested model is not a general numerical model valid for any type of concrete. To establish a more general model tests have to be performed studying all parameters that can effect the heat and strength development. For a given type of cement and a given type of fly ash, such additional parameters may be type and dosage of superplastiziser and aggregate type.

REFERENCES

1. Utsi S (2008): *Performance Based Concrete Mix-Design, Aggregate and Micro Mortar Optimization Applied on Self-Compacting Concrete Containing Fly Ash.* Doctoral Thesis 2008:49, Luleå University of Technology.
2. Utsi S & Jonasson J-E (2010): *Influence of different amount of fly ash for early age concrete containing Swedish cement – Part II: Calculations of form stripping times and the risk for early freezing for different amounts of fly ash*. Submitted for publication in NCR.
3. Papadakis V G, Fardis M N and Vayenas C G (1992): *Hydration and Carbonation of Pozzolanic Cement.* ACI Materials Journal, v.89 No. 2, March 1992, pp. 119-130.
4. Fraay A L A, Bijen J M and Haan Y M (1989): *The Reaction of Fly ash in Concrete. A Critical Examination.* Cement and Concrete Research, vol.19, pp. 235-246.
5. Berry E E and Malhotra V M (1980). *Fly Ash for Use in Concrete – A Critical Review*. ACI Journal, March-April 1989, pp 59-73.
6. Cannon R W (1968): *Proportioning Fly Ash Concrete Mixes for Strength and Economy*. ACI Journal, November 1968, pp 969 – 979.
7. SS-EN 450, (2005): *Fly ash for concrete.* Swedish Standards Institute, March 2005
8. SS-EN 206-1 (2001): Concrete-Part 1: Specification, performance, production and conformity. Swedish Standards Institute, July 2001.
9. Ekerfors K and Jonasson J-E (2000): Maturity Development in Young Concrete - Temperature Sensitivity, Strength and Heat Development. Nordic Concrete Research, Publication No. 25, 2000.
10. Jonasson J-E (1984): *Slipform construction – Calculations for Assessing Protection Against Early Freezing.* Swedish Cement and Concrete Research Institute, Stockholm, CBI Forskning/Research 4.84, 69 pp.
11. Kanstad T, Hammer T A, Bjøntegaard Ø and Sellevold E J (1999): Mechanical Properties of Young Concrete – Evaluation of Test Methods for Tensile Strength and Modulus of Elasticity – Determination of Model Parameters. NOR-IPACS report STF22 A99762. ISBN 82-14-01062-4.
12. Jonasson J-E (1994): *Modelling of Temperature, Moisture and Stresses in Young Concrete*. Luleå University of Technology, Doctoral Thesis 1994:153D, Luleå.
13. Freisleben Hansen P. and Pedersen E. J. (1977): *Måleinstrument til control af betons haerdning* (*in Danish*), Maturity computer for controlled curing and hardening of concrete. Journal of the Nordic Concrete Federation, No. 1:1977, Stockholm, pp 21-25.
14. Byfors J. (1980): *Plain concrete at early ages*. Swedish Cement and Concrete Research Institute, Fo/Research 3:80, Stockholm, 462 pp.

Influence of different amount of fly ash for early age concrete containing Swedish cement - Part II: Calculation of form stripping times and the risk for early freezing for different amounts of fly ash

Sofia Utsi
PhD in structural engineering, LTU
ProDevelopment AB
Storgatan 9
972 38 LULEÅ, SWEDEN
sofia.utsi@prodevelopment.se

Jan-Erik Jonasson
Professor in Structural engineering
Luleå University of Technology
971 87 LULEÅ, SWEDEN
jan-erik.jonasson@ltu.se

Abstract
A recently presented numerical tendency model has been applied on an assumed civil engineering structure. With the model parameters for heat and strength development calculations in early age period can be calculated. This paper shows the possibility to evaluate e.g. form removal times and estimations of need for protection against early freezing for concrete mixes containing fly ash in different amounts, with different water-to-cement ratios and at different outer conditions. The tendency model has shown to be a useful tool for production planning for concrete containing fly ash.

According to the performed calculations, any replacement of cement with fly ash will significantly influence the young concrete properties. The effect on delayed strength growth increases with the increased amount of fly ash and will also increase for lower temperatures. In addition, the effect from fly ash increases at higher water-to-cement ratios

Keywords: Fly ash, heat of hydration, strength growth, early age concrete, hardening control

1 INTRODUCTION

1.1 Objectives and Scope

In Part I of this paper [1], a tendency model for heat and strength development for variable fly ash contents is presented. Data from a tendency model can be used in structural analyses to be able to assess effects of using variable fly ash contents for different structures at different conditions as a part of a production planning. A tendency model facilitates the possibility to evaluate

e.g. form removal times and the risk for early freezing for concrete containing fly ash in various amounts.

The main objectives with the work presented in Part II of the paper are:
– To use the tendency model from Part I for practical applications in an assumed structure for calculations of form removal times and the risk for early freezing.
– Compare the presented model with measured heat development and strength growth for another group of concrete to investigate how many adjustments in the tendency model that is needed to be used on concrete made of other materials.

Fly ash in concrete is not common in Swedish concrete production, mainly because of the lack of national produced fly ash. However, there is an increased interest among concrete producers to use fly ash in concrete, mainly as a replacement of a part of the cement content. A tendency model is needed to assess the effects of using fly ash in different applications. This paper as well as Part I [1] are also parts of [2].

1.2 Heat development and strength growth

Hydration in concrete is an exothermic chemical reaction. A few hours after the concrete have been mixed, the reaction between water and cement starts to generate heat and the strength growth begins. The strength development is strongly related to the heat development, which is influenced by the chemistry of the binder and by the curing temperature. The temperature effect on the rate of hardening can be expressed by the temperature factor, which also is known as the "maturity function".

For the hardening control of young concrete, the knowledge of the maturity and the temperature development is essential to be able to plan and control the production properly. It involves estimations of form removal times, assessments of necessary times for moisture curing of the concrete surface, and estimation of conditions to avoid too early freezing of the young concrete.

1.3 The effect of fly ash on young properties

Fly ash is a pozzolanic material, which means that it reacts with the calcium hydroxide $Ca(OH)_2$ that is produced when cement reacts with water. When fly ash reacts with $Ca(OH)_2$, calcium silicate hydrate (CSH) is formed, which means that the content of the durable material (CSH) increases in the concrete, [3] and [4].

The in-corporation of fly ash in concrete can be performed in three different ways, [5]:

- Exchange cement with fly ash by weight on a 1:1 basis
- Exchange parts of the cement and parts of the aggregate
- Adding fly ash in addition to the cement as a part of the fine aggregate

According to [6] fly ash contributes to the concrete strength in three different ways; by a water reduction because demanded workability can be received at lower water contents when fly ash is added, by an increased effective paste volume and by the pozzolanic reaction. The first two will influence the early concrete strength while the latter will contribute to increased long-term strength.

Any replacement of Portland cement with fly ash in concrete will influence the compressive strength, and the strength growth may be low in the beginning, but the growth usually continues up to at least 6 months [5]. It is well known that in order to maintain the 28-days compressive strength the amount of fly ash added always exceeds the amount of cement removed [6]. This points out that the relation between fly ash and cement is one of the decisive parameters describing the strength growth.

2 LABORATORY TESTS AND NUMERICAL TENDENCY MODELS

2.1 Material

The tendency model presented in Part I [1] is based on laboratory tests performed on concrete mixes with four different fly ash contents and with two different equivalent water-to-cement ratios, which generates 18 different mixes. The use of an efficiency factor less than one will result in an increase of the total binder (cement plus fly ash) content, and in the tests the effects of using $k = 0.4$ and 0.8 were investigated. All tests were produced with concrete based on the Swedish cement type Anläggningscement Std P Degerhamn CEM I 42.5 N MH/SR/LA, produced by Cementa AB aimed for civil engineering structures, and the fly ash is black coal fly ash from Rostok, Germany, produced by Warnow-Füller that fulfils the demands according to [7]. The used aggregates were crushed Swedish aggregate.

2.2 Laboratory tests and numerical tendency model

The calculations in this paper are performed with a numerical tendency model established in Part I of this paper [1]. The performed laboratory tests and the established numerical tendency model are fully described in Part I of this paper and are only briefly described here.

The heat development has been determined with calorimetric methods and for the tests presented in Part I a semi-adiabatic method have been used. Cylinder samples of concrete have been cured under semi-adiabatic conditions, and the temperature in the samples has been registered. After about two weeks the specimen has been heated, still situated inside the semi-adiabatic equipment, and the cooling phase has been registered. The exchange of heat with the surroundings during the hydration phase, expressed by the so called heat cooling ratio, is then possible to calculate. This is realized to be able to compensate for the loss of heat during the test period, see further [8].

The strength development in concrete is influenced by the temperature. By curing in different temperatures and testing the compressive strength, it is possible to determine the effect of temperature on the strength development and to determine the maturity function. Concrete cubes of 100x100x100mm were stored in three different water temperatures: 5°, 20° and 35°, respectively. The concrete temperature was registered continuously and the strength development was studied by testing the compressive strength at four occasions between 8 and 168 h after casting. Additional cubes are cured under water in 20°C to determine the 28-day and 91-day compressive strength.

From the laboratory test results, tendencies regarding the heat of hydration and strength development due to w_0/C ratio and fly ash content have been evaluated. A tendency model for calcu-

lations of the heat and strength development for various fly ash contents and water to cement ratios has been established. The numerical tendency model for the heat development and for the strength growth is assumed to be separable regarding effects of w_0/C ratio and fly ash content. This assumption makes it easier to choose which formula to be used to model different observed effects in a consistent way.

3 THEORETICAL STUDY OF THE EFFECT FROM DIFFERENT FLY ASH CONTENTS

3.1 Choice of structure and mix composition

With the tendency model presented in Part I [1] of this paper, calculations are performed on an assumed civil engineering structure, Figure 1. It comprises a bottom slab, walls and a top slab. Calculations are performed in section A of the top slab and in section B of the wall. The top slab is chosen to be 0.8m thick and the walls are selected to be 0.7m thick.

The calculation examples are based on two types of concrete with w_0/C_{equ} = 0.4 and 0.5, respectively. For w_0/C_{equ} = 0.4 the reference mix with 0 % fly ash contains 420 kg/m^3 Portland cement with a required 28-days compressive strength of 45 MPa. For w_0/C_{equ} = 0.5 the reference mix with 0 % fly ash contains 400 kg/m^3 with a required 28-days compressive strength of 35 MPa.

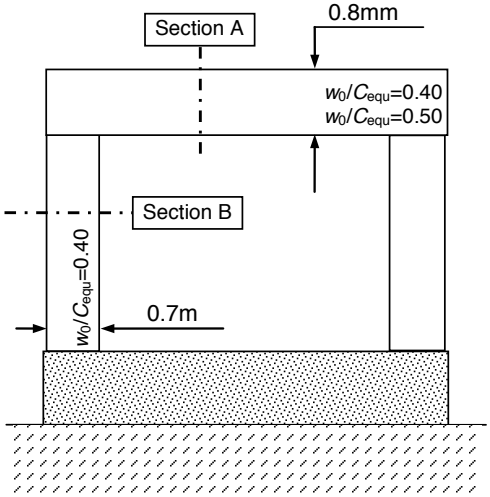

Figure 1 - Assumed civil engineering structure for the heat and strength development calculations at different temperatures and varying fly ash contents.

Cement is replaced by fly ash in three amounts, 11 %, 25 %, and 40 % by weight of the cement content. The sum of cement and fly ash, $C + FA$, has been kept constant at the same amount as in the reference mix, i.e. 420 kg/m^3 and 400 kg/m^3, respectively, with an efficiency factor of 0.4. Material parameters for the usage of the computer program [9] are determined in accordance with the tendency model presented in [1]. The mix composition and the calculated heat and strength parameters are presented in Table 1.

Table 1 - Mix composition and calculated material parameters used in computer program Con-Test (2008).

	0% Fly ash		11% Fly ash		25% Fly ash		40% Fly ash	
w_0/C_{equ}	0.40	0.50	0.40	0.50	0.40	0.50	0.40	0.50
C [kg/m^3]	420	400	378	360	336	320	300	286
w_0 [kg/m^3]	168	200	157	189	149	175	140	165
FA [kg/m^3]	0	0	42	40	84	80	120	114
k [-]	-	-	0.4	0.4	0.4	0.4	0.4	0.4
W_U [J/kg]	261305	263932	241896	244430	217096	219474	190401	192569
λ_1 [-]	1	1	1	1	1	1	1	1
t_1 [h]	10.70	10.33	10.70	9.76	10.68	8.55	10.64	8.01
κ_1 [-]	1.964	1.86	1.96	1.832	1.97	1.812	1.993	1.809
f_{28} [MPa]	66.3	47.9	64.8	46.5	63.0	44.9	61.1	43.2
s [-]	0.309	0.358	0.327	0.367	0.352	0.365	0.359	0.361
t_S [h]	3	3	3.3145	3.3145	4.2516	4.2416	5.0775	5.0775
t_A [h]	4.5	4.5	4.972	4.9717	6.3774	6.3774	7.6162	7.6162
η_A [-]	3	3	3	3	3	3	3	3
θ_{ref} [K]	3870	3870	3870	3870	3870	3870	3870	3870
κ_3 [-]	0.57	0.57	0.57	0.57	0.57	0.57	0.57	0.57

The calculated values of f_{28} in Table 1 show that the required strength values, $f_{28} \geq 45$ MPa for $w_0/C_{equ} = 0.4$ and $f_{28} \geq 35$ MPa for $w_0/C_{equ} = 0.4$, are reached for all mixes.

3.2 Results for section A of the top slab

Assumed performance conditions and demanded target values

In section A of the top slab calculations are performed for the conditions illustrated in Figure 2; formwork made of 25 mm wood at the bottom with wind velocity of 1 m/s below the formwork; A free surface on the top exposed to air with wind velocity of 5 m/s. Calculations are performed at four different outdoor temperatures; 0, 5, 10 and 15°C, and for two different w_0/C_{equ} ratios, 0.40 and 0.50.

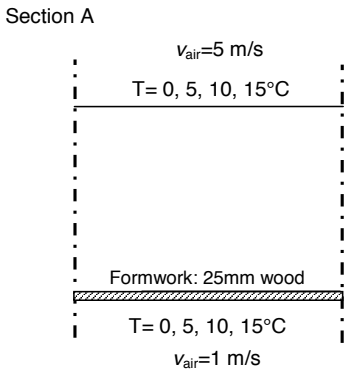

Figure 2 - Conditions used in the calculations for section A.

The results are evaluated considering the following assumed demanded values:

- Time when reaching 5 MPa in compressive strength at the top surface, which is employed as the limit for early age frost protection for the actual situation.
- Form removal time regarding the demand of a sufficient average compressive strength of 70 % of the required strength at 28 d.
- Demands on surface moisture curing for T≥10 °C until the top surface reaches 50 % of the required strength at 28 d.

The demands on the performance of a concrete structure may be stated in accordance with some code or stated directly by the owner of the building object. However, calculations of the type performed here can answer questions if, when and how any stated demand of the type described here can be fulfilled, and the chosen demands shall only be regarded as an arbitrary set of possible demands. It is usually essential to get information if additional measures are needed or not for a given situation.

Estimation of the risk for early freezing

The risk for early freezing occurs if the concrete freezes before reaching the stated demand of 5 MPa compressive strength. To get information to estimate the need for protection against early freezing, it is important to calculate the time needed for the concrete to reach this limit. In springtime or in the autumn, the temperature can reach 10°C during the day, but it can fall below zero during the night. The time needed to reach 5 MPa at different fly ash contents for temperatures between 0 and 10°C is plotted in Figures 3-4. From the figures it is seen that the time to reach 5 MPa is delayed with higher fly ash contents and lower air temperatures. Note that it takes about two days to get frost protection using 40 % of fly ash content at 0°C temperature for w_0/C_{equ}=0.40. The time for w_0/C_{equ}=0.50 is further delayed with approximately ten hours. For these cases, probably some measures should be taken to speed up the hydration rate, but this is not studied here.

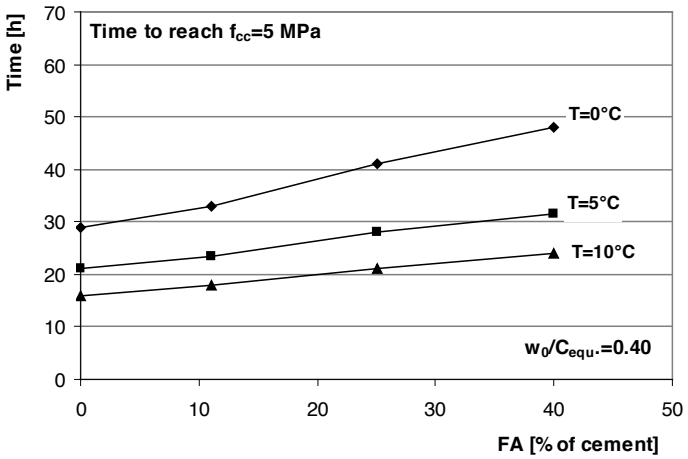

Figure 3 - Time needed to reach 5 MPa, the demanded limit for protection against early freezing, for different fly ash contents and different outdoor temperatures for w_0/C_{equ}*=0.40.*

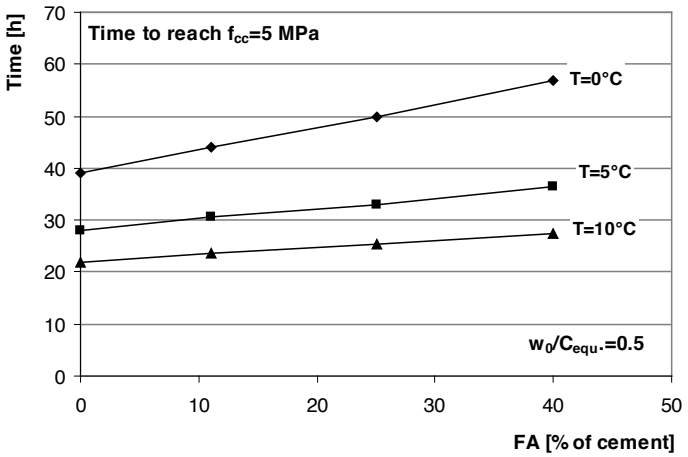

Figure 4 - Time needed to reach 5 MPa, the demanded limit for protection against early freezing, for different fly ash contents and different outdoor temperatures for w_0/C_{equ}*=0.50*

Calculation of form removal times

The predetermined demand to allow formwork removal for the top slab is 70 % of the required 28-days compressive strength, which for this case with f_{28} = 45 MPa means 31.5 MPa, and for f_{28} = 35 MPa the form stripping strength is 24.5 MPa. The calculated times to reach these demanded levels are presented in Figures 5-6.

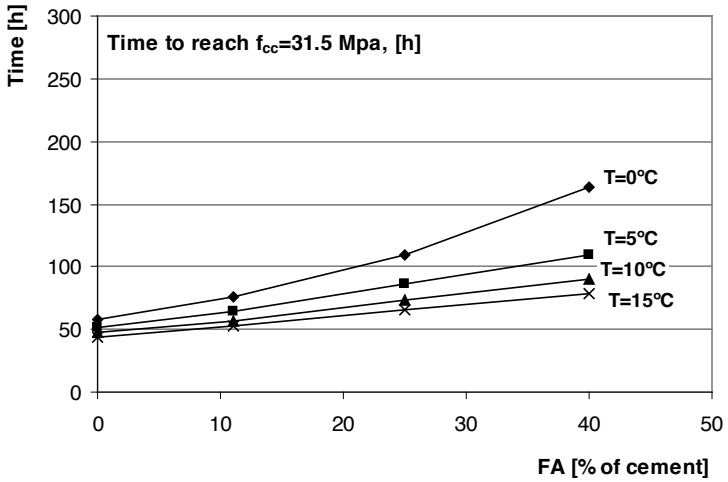

Figure 5 - Time needed to reach 70 % of required f_{28} *for different fly ash contents when the outdoor temperature is 0, 5, 10 and 15°C for* f_{28} *= 45 MPa.*

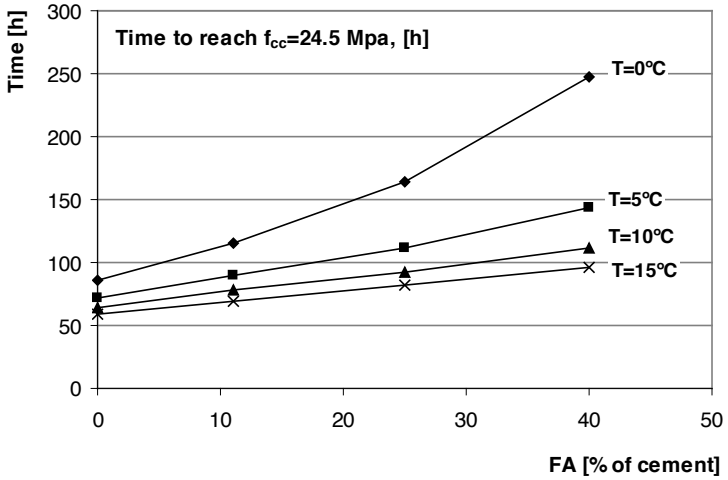

Figure 6 - Time needed to reach 70 % of required f_{28} for different fly ash contents when the outdoor temperature is 0, 5, 10 and 15°C for $\boldsymbol{f_{28}}$ = 35 MPa.

It can be concluded that the effect of the outdoor temperature on the strength development will significantly increase when the fly ash content increases. In case of 0 % fly ash, the time needed to reach 31.5 MPa and 24.5 MPa will only slightly increase when the outdoor temperature is 0°C in comparison to 15°C. When cement is replaced by 40 % fly ash, the time needed to reach demanded form removal time will increase with a factor two if the temperature is 0°C compared to 15°C for w_0/C_{equ} = 0.40. For w_0/C_{equ} = 0.50, the corresponding time delay is increased about 2.5 times. These delays mean that the use of high fly ash contents in low temperatures should always be completed with analyses to form the basis for decisions how to act.

3.3 Results for section B of the walls

Assumed performance conditions and demanded target values
Calculations for section B in the walls are performed for the conditions illustrated in Figure 7. Formwork made of 25 mm wood at both sides exposed to an air wind velocity of 5 m/s. As in the example with the top slab, calculations are performed at four different outdoor temperatures; 0, 5, 10 and 15°C.

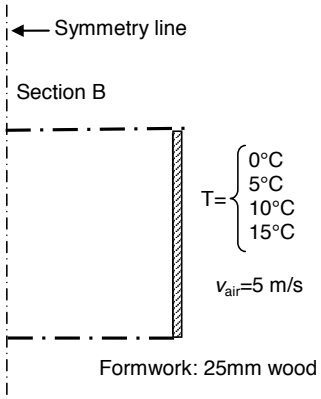

Figure 7 - Conditions used in performed calculations for section B. Half of the wall is shown in the figure.

The demand on surface moisture curing is assumed to be the time until 50 % of the required strength is reached at the surfaces. The retained formwork is an accepted alternative to moisture curing, which means that the form removal shall not be performed earlier than the demanded time for moisture curing. However, form stripping might cause high tensile stresses and surface cracking. The recommendation to limit the risk of surface cracking for walls, see [10], is that the formwork shall not be removed during the first four days. Form removal times for walls will in the calculation example be either four days or when the concrete has reached 50 % of required 28-compressive strength.

Calculation of form removal times
The resulting calculated times to reach half the required 28-days compressive strength is presented in Figure 8.

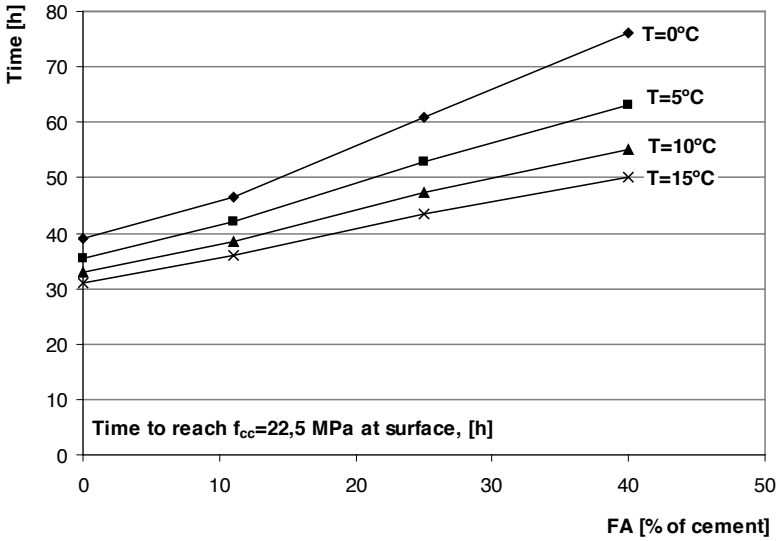

Figure 8 - Time needed to reach 0.5 f_{28} at the surface of the wall, which is the demanded limit for moisture curing.

For the analysed wall structure, all calculations performed reach a surface strength higher than 50 % of the required compressive strength within 4 days. So, in relation to the chosen demanded moisture curing condition, the formwork removal demand connected to the risk of surface cracking is here decisive. For other structures and other moisture curing demands the situation might be different.

In Paper D appended in [2], submitted to the magazine Materials & Structures, the risk for early thermal cracking for concrete containing fly ash is estimated for an assumed civil engineering structure similar to the structure in this paper. In Paper D in [2] it is concluded that the mixes containing fly ash had a higher heat development caused by increased binder content, as fly ash was added as replacement of part of the aggregate. However, from the numerical stress analysis for the assumed civil engineering construction it can be shown that the risk for early age through cracks is significantly decreased for the mixes containing fly ash. In case of adding fly ash to concrete by a partial replacement of the cement, the crack risk will probably be further decreased. It is also concluded from the results presented in that paper that the risk for surface cracks in the analyzed wall (0.7m) is very small for all of the evaluated mixes, fly ash content from 0 to 25 %. The lower risk for early thermal cracking might be an effect from the increased early creep for mixes containing fly ash.

However, the estimated risk for surface cracks in an analyzed slab (1m) on ground was not improved by an incorporation of fly ash [2]. The mix containing 25% fly ash had the highest risk for surface cracks in the slab, which probably is an effect from the increased heat development in combination with the thickness of the slab. The increased heat development has probably compensated the positive effect from the increased early-age creep for concrete containing fly ash.

Average temperature in the wall section

In Figures 9-10 the average temperature in the wall section is plotted for different fly ash contents at 0 °C and 15 °C. It can be concluded that the concrete temperature will decrease significantly for any replacement of cement by fly ash.

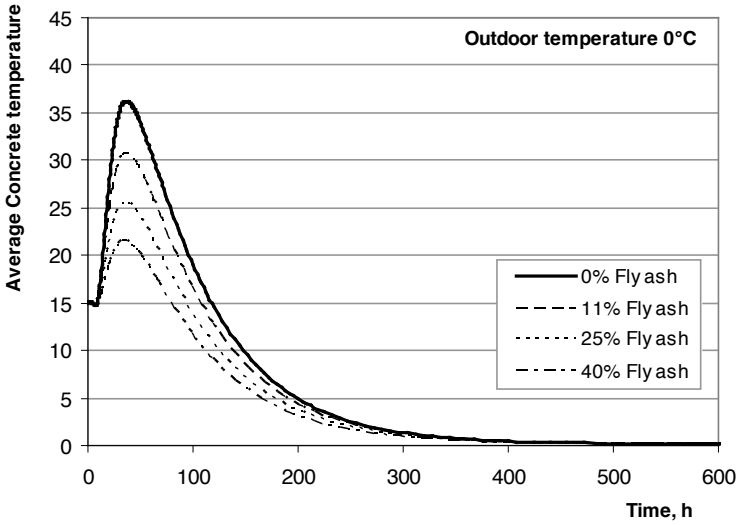

Figure 9 – The average temperature in the wall for different fly ash contents at 0 °C.

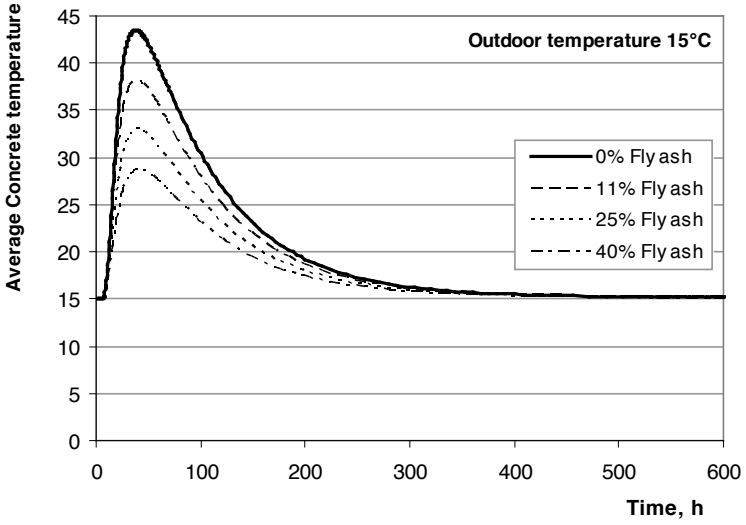

Figure 10 - The average temperature in the wall for different fly ash contents at 15 °C.

4 TENDENCY MODEL APPLIED ON ANOTHER CONCRETE GROUP

4.1 Introduction

The presented tendency model is based on measured data performed on one type of concrete with various fly ash contents. The basic assumption when building the formulas is that the effects of w_0/C ratio and of the fly ash content can be mathematically separated. However, there is an interest in investigation of how the presented model may suit another type of concrete group, but still using the same type of cement and same type of fly ash.

In this section, measured heat development and strength growth for another group of concrete is compared with the presented model.

Three concrete mixes containing 0 %, 11 % and 25% fly ash has been tested. They are composed according to the values presented in Table 2 and they are composed with another type of aggregate and with other dosages of superplastiziser in comparison to the 18 mixes that the tendency model is based on.

Table 2 - Mix-composition for the new group of tested mixes.

Mix No.	FA/C	w_0/C_{equ}	k	C kg/m^3
1	0	0.437	-	400
2	0.11	0.421	0.4	400
3	0.25	0.417	0.4	400

4.2 Heat of hydration

In Figure 11, the measured heat of hydration is plotted together with the results calculated with the presented tendency model, see dotted lines. A difference between measured data and calculated is obtained.

For all of the three tested mixes there are two main tendencies concerning heat of hydration between the measured data and the tendency model in [1]; 1) the total heat of hydration per kg binder is increased, and 2) the reduction in heat, followed by an increased content of fly ash, is less pronounced. By adjusting the fitting parameters in the two formulas that expresses the effect from w_0/C ratio and the fly ash content, Eqs. 1 and 2, the tendency model is adjusted to describe the behaviour for the new concrete group.

$$W_{ref} = 283 - 20 \cdot exp\left[-\left(\frac{w_0 / C}{0.65} \right)^2 \right] \quad (1)$$

and

$$\gamma_w = 1 - 0.23 \cdot \frac{FA}{C} \quad (\geq 0.7) \quad (2)$$

The material related behaviour behind this phenomenon is not known, but it can very easily, and for a few adjustments, be mathematically expressed for further heat calculations.

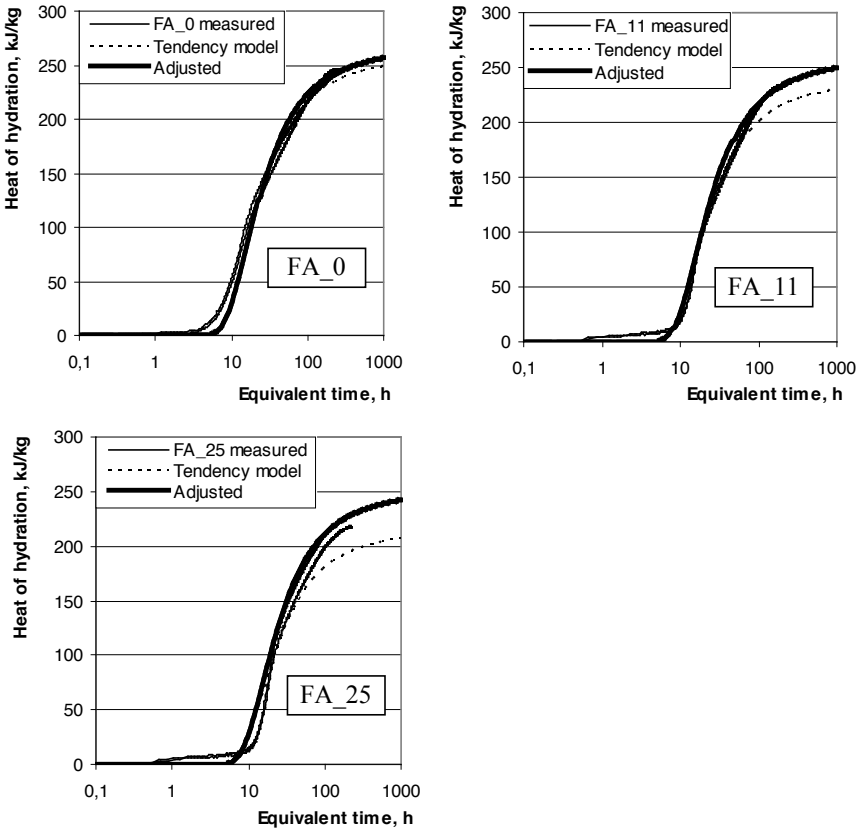

Figure 11 - Measured heat of hydration plotted together with calculated by the presented tendency model and the adjusted tendency model. By a few adjustments, the model can be applied on other types of concrete.

4.3 Strength growth

In Figures 12-14, the measured compressive strength growth is plotted in comparison with calculations using the presented tendency model (dashed lines) and after adjustments (solid lines) for three fly ash contents. The new tested concrete group is showing a lower 28-day compressive strength than calculated and the strength growth is faster in the beginning. These two phenomena can be adjusted by Eqs. 3 - 6 expressed by

$$f_{ref} = 2700 \cdot exp\left[-\left(80 \cdot \frac{w_0}{C} \right)^{0.392} \right] \quad \text{[MPa]} \tag{3}$$

$$\gamma_f = 1 + 0.94 \cdot \frac{FA}{C} \qquad (\leq 1.4) \tag{4}$$

$$s_0 = 0.29 - 0.10 \cdot \exp\left[-\left(\frac{w_0 / C}{0.5} \right)^5 \right] \tag{5}$$

$$s_1 = 0.30 \quad (6)$$

By introducing these adjustments the adjusted tendency model can be used for this new type of concrete group, and all necessary data to be able to perform further analyses of heat and strength developments using different amounts of fly ash.

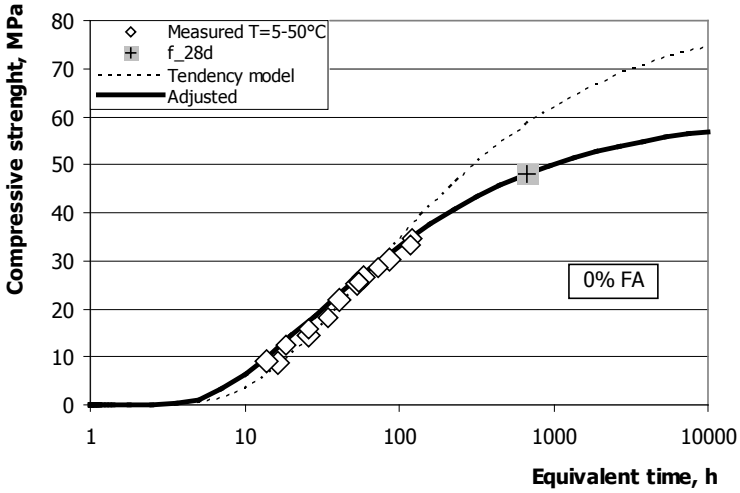

Figure 12 - Measured compressive strength for temperature 5, 20, 35 and 50°C compared to the calculated with the tendency model and calculated by the adjusted model for 0 % fly ash content.

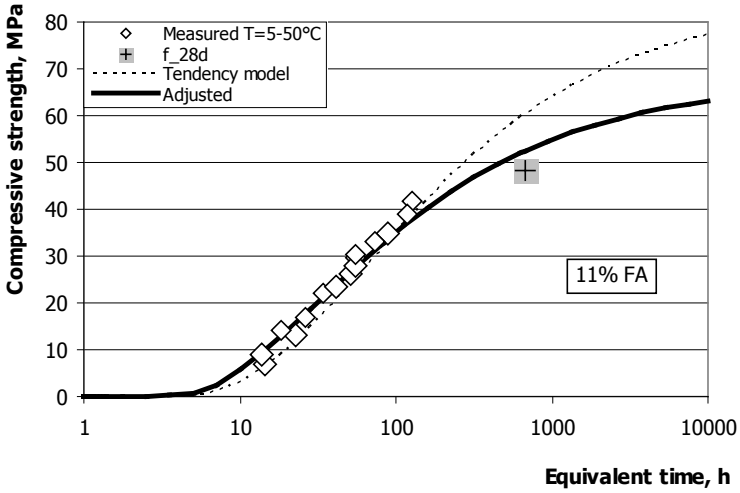

Figure 13 - Measured compressive strength for temperature 5, 20, 35 and 50°C compared to the calculated with the tendency model and calculated by the adjusted model for 11 % fly ash content.

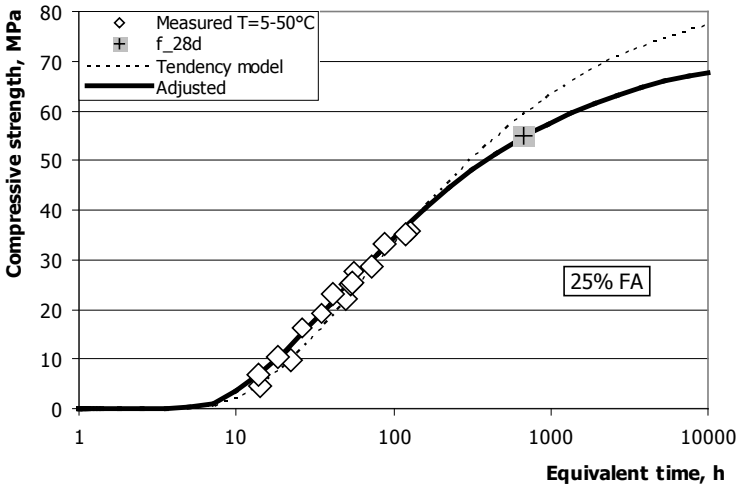

Figure 14 - Measured compressive strength for temperature 5, 20, 35 and 50°C compared to the calculated with the tendency model and calculated by the adjusted model for 25 % fly ash content.

4.4 Concluding remarks

The three additional tested concrete mixes are composed from other types of aggregate materials, and it could be concluded that the presented model did not describe the behavior sufficiently. However, by a few adjustments the model is applicable on the new group of concrete mixes. This indicates that the basic structure of the presented tendency model seems to be useful for other types of concretes containing different amounts of fly ash.

Since the tendency model is based on formulas expressing the effect of the water-to-cement ratio and of the amount of fly ash as partial factors, it facilitates the possibility to trace where adjustments probably shall be performed. The new tested concrete group and its correlation to the presented tendency model showed a systematic deviation, which easily directed the necessary adjustments to a limited number of parameters. Hereby, a few tests were used to fully describe the behavior for a new group of concrete for further use in strength and heat calculations. However, to be able to extend this statement into a general situation analyzing different amounts of fly ash, a lot more testing and checking have to be performed.

5. CONCLUSIONS

- According to the performed calculations, any replacement of cement with fly ash will significantly influence the young concrete properties. The effect on delayed strength growth increases with the increased amount of fly ash and will also increase for lower temperatures. In addition, the effect from fly ash increases at higher water-to-cement ratios.

- The reduced strength growth, especially in lower outdoor temperatures, may delay form removal times or increase the risk for early thermal freezing. The application of the numerical tendency model appears to be a useful tool for production planning for concrete containing fly ash.

- The concrete temperature is significantly lower for any replacement of cement with fly ash.

- The suggested tendency model is based on a test series where all parameters except the water-to-cement ratios and fly ash content has been constant. It has been concluded that the suggested model can not directly be applied on concrete composed from other types of material. However, with a few additional tests and adjustments in the tendency model, it has been shown to be applicable on another concrete type with sufficient agreement.

- The suggested model is not a general numerical model valid for any type of concrete. To establish a more general model tests have to be performed studying all parameters that can effect the heat and strength development. For a given type of cement and a given type of fly ash, such additional parameters may be type and dosage of superplastiziser and aggregate type.

REFERENCES

1. Utsi S & Jonasson J-E (2010): *Influence of different amount of fly ash for early age concrete containing Swedish cement – Part I: Tendency model for heat and strength development for variable fly ash content.* Submitted for publication in NCR.
2. Utsi S (2008): *Performance Based Concrete Mix-Design, Aggregate and Micro Mortar Optimization Applied on Self-Compacting Concrete Containing Fly Ash.* Doctoral Thesis 2008:49, Luleå University of Technology.
3. Papadakis V G, Fardis M N and Vayenas C G (1992): *Hydration and Carbonation of Pozzolanic Cement.* ACI Materials Journal, v.89 No. 2, March 1992, pp. 119-130.
4. Fraay A L A, Bijen J M and Haan Y M (1989): *The Reaction of Fly ash in Concrete. A Critical Examination.* Cement and Concrete Research, vol.19, pp. 235-246.
5. Berry E E and Malhotra V M (1980). *Fly Ash for Use in Concrete – A Critical Review*. ACI Journal, March-April 1989, pp 59-73.
6. Cannon R W (1968): *Proportioning Fly Ash Concrete Mixes for Strength and Economy*. ACI Journal, November 1968, pp 969 – 979.
7. SS-EN 450, (2005): *Fly ash for concrete.* Swedish Standards Institute, March 2005
8. Ekerfors K and Jonasson J-E (2000): Maturity Development in Young Concrete - Temperature Sensitivity, Strength and Heat Development. Nordic Concrete Research, Publication No. 25, 2000.
9. ConTeSt Pro – Users Manual (2008): *A Program for Temperature and Strength Calculations in Concrete*. JEJMS Concrete AB, Luleå, 202 pp.
10. Emborg M, Bernander S, Ekerfors K, Groth P, Hedlund H (1997): *Temperatursprickor i betongkonstruktioner - Beräkningsmetoder för hydratationsspänningar och diagram för några typfall (inSwedish), Thermal Cracking in Concrete Structures – Calculation Methods for Hydration Stresses and Diagrams for Some Typical Cases*. Division of Structural Engineering, Luleå University of Technology, Technical Report 1997:02, 100 pp.